Thermoelasticity of Hexagonal Close-Packed Iron from the Phonon Density of States

Thesis by

Caitlin A. Murphy

In Partial Fulfillment of the Requirements

for the Degree of

Doctor of Philosophy

CALIFORNIA INSTITUTE OF TECHNOLOGY

Pasadena, California

2012

(Defended May 18, 2012)

© 2012

Caitlin A. Murphy

All Rights Reserved

Acknowledgements

First and foremost, I would like to thank my advisor, Jennifer Jackson. Our research discussions provided me with a solid foundation in mineral physics, from both Earth Science and Materials Science perspectives. In addition, I benefitted greatly from your novel and interesting approaches to the unanswered questions about the deep Earth. Equally important are the more personal aspects of your mentorship; your annual lab parties, outings to the Rathskeller, and friendship contributed greatly to my experience as a graduate student. Finally, mineral physics at Caltech would not be the same without such wonderful puns (intended or not) as the need to have “all of our DACs in a row” before heading to the synchrotron.

I am especially thankful for the incredible research opportunities afforded to me over the past five years, and the people who made them possible. In addition to Jennifer, I would like to thank the other members of the self-proclaimed “beam team”: Wolfgang Sturhahn, Bin Chen, and Dongzhou Zhang. The quality of the experimental data on which this thesis is based—in addition to the corresponding analyses—would not have been possible without Wolfgang’s expertise and guidance. In addition, I benefitted greatly from research discussions with Bin and Dongzhou, related to both experimental techniques and their applications to Earth Science. Your passion, drive, and work ethic are truly

inspirational, and it was an honor to perform our experiments together. Finally, I thank the past and present members of the Inelastic and Nuclear Resonant Scattering group at the Advanced Photon Source, Argonne National Laboratory, for your excellent beamline and constant support of our experiments: Jiyong Zhao, Michael Hu, Tom Toellner, Esen Alp, Hassan Yavas, Ayman Said**,** and Ahmet Alatas. A special thank you goes to Tom Toellner for your helpful discussions about both my experiments and career goals.

I thank the faculty at Caltech for providing me with a strong foundation in the underlying principles and applications of Mineral Physics. I thank Paul Asimow for sharing your seemingly endless knowledge of geochemistry, and in particular for your insights on chemical thermodynamics, differentiation of the Earth, and isotope fractionation. I also thank Brent Fultz for allowing me to see our experiments and results through the eyes of a Materials Scientist, both in your course on phase transformations and at your group meetings. Finally, thank you both for serving on my thesis committee; this thesis has benefitted greatly from your diverse expertise and invaluable feedback.

I would also like to thank Rob Clayton, first for serving on my thesis committee. In addition, thank you for three great years as a Teaching Assistant on the Ge111 field trips to the Salton Sea. The field experience, in-depth exposure to applied geophysics techniques, and teaching experience I gained from those trips are invaluable. Your efficiency in the field, passion for teaching, and dedication to the students are all exemplary qualities. Finally, thank you for your support and guidance, especially during my first years at Caltech; with only a few words, you had an incredible impact on my experience here.

I thank Tom Heaton for imparting on me your vast knowledge of seismology from both engineering and Earth Science perspectives. Your courses provided me with a strong

foundation in the principles of seismology and the more relevant features of seismometers and seismic data analysis. I also thank you for your passion for teaching and the students, which is evident in everything you do. I am grateful for your friendship during my final years at Caltech, and for your stories about the Seismolab, geophysics, and life in general.

I am very grateful that I got to explore a proposition project with Professor George Rossman, investigating the coloration mechanism of beryllium-doped corundum with the electron paramagnetic resonance technique. Your enthusiasm for the project was truly contagious, and your mentoring during my first year was invaluable. I continue to be awed by the wealth of information I learned from you after just one short year, and I look forward to writing up that project with you soon.

I thank my officemates—Ting Chen, Laura Alisic, Jeff Thompson, Semechah Liu, and Yiran Ma—for providing such a positive and comfortable work environment. In addition, I am thankful for the wonderful support staff in the Seismolab: Viola Carter, Evelina Cui, Sarah Gordon, Rosemary Miller, Donna Mireles, and Julia Zuckerman. I appreciate the efficiency and care with which you handle Siesmolab affairs, and my day-to-day experience would not have been the same without your smiling faces. Thank you for fostering a fun and friendly environment via the Seismo Socials and Annual Retreat.

I had the privilege of attending two incredible enrichment trips during my time at Caltech. First, I thank John Eiler and Jean-Philippe Avouac for organizing the Enrichment Trip to the Alps, and our local hosts—Lukas Baumgartner, David Flöss, Robert Bodner—for sharing their extensive knowledge about Alpine geology and the wonderful culture embedded in the Swiss and Italian Alps. In addition, I thank Jason Saleeby and John Eiler for organizing and running the 2012 Pahoehoe Trip. Jason’s incredible knowledge of both

the Hawaiian geology and culture made for a truly memorable trip.

My experience at Caltech has also been enriched by extracurricular activities and the wonderful friends I have made. I would like to thank the Love Waves for four amazing softball seasons, each with just enough wins to keep morale high. I thank Jack Prater, Kathy Torres and the rest of the Caltech volleyball community for providing me with a fun way to blow off steam. And I am grateful to my friends across the Institute for all of the great memories: Lisa Mauger, Steve Skinner, Jessica Pfeilsticker, Keenan Crane, Patrick Sanan, Mike Deceglie, Emily Warren, and Karín Menéndez-Delmestre.

I thank my family for your unending support during my time in graduate school. Your frequent presence helped make Southern California feel like home, and I am so grateful that you were there through all of the major milestones.

Finally, I thank my husband, Don Jenket. I cannot believe it has already been five years since we left Quantico for the West Coast, and the incredible journey we have had since. My weekend trips to Oceanside helped me to accelerate and succeed in my graduate program, as they motivated me to push hard during the week so I could enjoy our few days together over the weekend. Our trips to New Zealand, Italy, and the Canadian Rockies were wonderful rewards for all of our hard work. And your experience in the Marines helped me to keep the proper perspective about graduate school and life in general. I greatly appreciate all you have done to support me during graduate school, and I am excited to start our next adventure together in Washington, D.C.

Abstract

Iron is the main constituent in Earth's core, along with ~5 to 10 wt% Ni and some light elements (e.g., H, C, O, Si, S). This thesis explores the vibrational thermodynamic and thermoelastic properties of pure hexagonal close-packed iron (ε-Fe), in an effort to improve our understanding of the properties of a significant fraction of this remote region of the deep Earth and in turn, better constrain its composition.

In order to access the vibrational properties of pure ε-Fe, we directly probed its total phonon density of states (DOS) by performing nuclear resonant inelastic x-ray scattering (NRIXS) and *in situ* x-ray diffraction (XRD) experiments at Sector 3-ID-B of the Advanced Photon Source (APS) at Argonne National Laboratory. NRIXS and *in situ* XRD were collected over the course of ~14 days at eleven compression points between 30 and 171 GPa, and at 300 K. Our *in situ* XRD measurements probed the sample volume at each compression point, and our long NRIXS data-collection times and high-energy resolution resulted in the highest statistical quality dataset of this type for ε-Fe to outer core pressures. Hydrostatic conditions were achieved in the sample chamber for our experiments at smaller compressions ($P \leq 69$ GPa) via the loading of a neon pressure transmitting medium at the GeoSoilEnviroCARS (GSECARS) sector of the APS. For measurements made at $P > 69$ GPa, the sample was fully embedded in boron epoxy, which served as the pressure

transmitting medium.

From each measured phonon DOS and thermodynamic definitions, we determined a wide range of vibrational thermodynamic and thermoelastic parameters, including the Lamb-Mössbauer factor; vibrational components of the specific heat capacity, free energy, entropy, internal energy, and kinetic energy; and the Debye sound velocity. Together with our *in situ* measured volumes, the shape of the total phonon DOS and these parameters gave rise to a number of important properties for ε-Fe at Earth's core conditions.

For example, we determined the Debye sound velocity (v_D) at each of our compression points from the low-energy region of the phonon DOS and our *in situ* measured volumes. In turn, v_D is related to the compressional and shear sound velocities via our determined densities and the adiabatic bulk modulus. Our high-statistical quality dataset places a new tight constraint on the density dependence of ε-Fe's sound velocities to outer core pressures. Via comparison with existing data for iron alloys, we investigate how nickel and candidate light elements for the core affect the thermoelastic properties of iron. In addition, we explore the effects of temperature on ε-Fe's sound velocities by applying pressure- and temperature-dependent elastic moduli from theoretical calculations to a finite-strain model. Such models allow for direct comparisons with one-dimensional seismic models of Earth's solid inner core (e.g., the Preliminary Reference Earth Model).

Next, the volume dependence of the vibrational free energy is directly related to the vibrational thermal pressure, which we combine with previously reported theoretical values for the electronic and anharmonic thermal pressures to find the total thermal pressure of ε-Fe. In addition, we found a steady increase in the Lamb-Mössbauer factor with compression, which suggests restricted thermal atomic motions at outer core pressures.

This behavior is related to the high-pressure melting behavior of ε-Fe via Gilvarry's reformulation of Lindemann's melting criterion, which we used to obtain the shape of ε-Fe's melting curve up to 171 GPa. By anchoring our melting curve shape with experimentally determined melting points and considering thermal pressure and anharmonic effects, we investigated ε-Fe's melting temperature at the pressure of the inner–core boundary (ICB, P = 330 GPa), where Earth's solid inner core and liquid outer core are in contact. Then, combining this temperature constraint with our thermal pressure, we determined the density of ε-Fe under ICB conditions, which offers information about the composition of Earth's core via the seismically inferred density at the ICB.

In addition, the shape of the phonon DOS remained similar at all compression points, while the maximum (cutoff) energy increased regularly with decreasing volume. As a result, we were able to describe the volume dependence of ε-Fe's total phonon DOS with a generalized scaling law and, in turn, constrain the ambient temperature vibrational Grüneisen parameter. We also used the volume dependence of our previously mentioned ν_D to determine the commonly discussed Debye Grüneisen parameter, which we found to be ~10% smaller than our vibrational Grüneisen parameter at any given volume. Finally, applying our determined vibrational Grüneisen parameter to a Mie-Grüneisen type relationship and an approximate form of the empirical Lindemann melting criterion, we predict the vibrational thermal pressure and estimate the high-pressure melting behavior of ε-Fe at Earth's core pressures, which can be directly compared with our previous results.

Finally, we use our measured vibrational kinetic energy and entropy to approximate ε-Fe's vibrational thermodynamic properties to outer core pressures. In particular, the vibrational kinetic energy is related to the pressure- and temperature-dependent reduced

isotopic partition function ratios of ε-Fe and in turn, provide information about the partitioning behavior of solid iron in equilibrium processes. In addition, the volume dependence of vibrational entropy is directly related to the product of ε-Fe's vibrational component of the thermal expansion coefficient and the isothermal bulk modulus, which we find to be independent of pressure (volume) at 300 K. In turn, this product gives rise to the volume-dependent thermal expansion coefficient of ε-Fe at 300 K via established EOS parameters, and the vibrational Grüneisen parameter and temperature dependence of the vibrational thermal pressure via thermodynamic definition.

Table of Contents

List of Figures

List of Tables

NOTATION AND NOMENCLATURE

As a reference, we provide descriptions and definitions for the following list of acronyms and variables that appear frequently in the chapters of this thesis. The following three tables are organized by related topics.

Table xvii.1. Acronyms for average Earth models and major boundaries in the deep Earth.

Acronym	**Definition and Description**
CMB	Core–mantle boundary: A seismically determined boundary between Earth's iron-rich outer core and the overlying silicate-rich mantle, which lies at a depth of ~2891 km. It is indicated in seismic models by a sudden increase in density, decrease in compressional sound velocity, and disappearance of shear waves.
ICB	Inner–core boundary: A seismically determined boundary between Earth's solid inner core and liquid outer core, which lies at a depth of ~5150 km. It is indicated in seismic models by a slight increase in density and compressional sound velocity, and the reappearance of shear waves.
PREM	Preliminary reference Earth model: A commonly cited average Earth model that is based on thousands of seismic observations collected at over 30 seismic stations around the continents. PREM provides average density and seismic wave velocity profiles with depth, based on the assumption that the Earth is radially symmetric (*Dziewonski and Anderson,* 1981).

Table xvii.2. Terms related to experimental techniques discussed in this thesis.

Term	Definition and Description
ALS	Advanced Light Source: A 2nd-generation synchrotron x-ray source at Lawrence Berkeley National Laboratory, Berkeley, CA, USA.
APS	Advanced Photon Source: A 3rd-generation synchrotron x-ray source at Argonne National Laboratory, Argonne, IL, USA.
IXS	Inelastic x-ray scattering: An experimental technique that probes the dispersion of longitudinal acoustic phonon energies and in turn, the elastic tensor and sound velocities of single crystal samples.
NRIXS	Nuclear resonant inelastic x-ray scattering: An experimental technique that probes the partial projected phonon density of states of select isotopes.
DOS	Density of states: In general, a density of states gives the distribution of states, or the number of states that exist for a given energy interval; in this study, we use the term in the context of the "phonon density of states," which provides the energy (frequency) distribution of all vibrational states (phonon modes) of a material.
XRD	X-ray diffraction: An experimental technique that probes a material's interplanar atomic spacing and in turn, the unit cell parameters and unit cell volume of a crystalline material.
EOS	Equation of state: An equation describing the relationship between state variables for a material under a given set of physical conditions. In this study, the most common equations of state relate a material's pressure with its volume, and occasionally temperature.
bcc	Body-centered cubic: A non-close-packed crystal structure with cubic symmetry.
fcc	Face-centered cubic: A close-packed crystal structure with cubic symmetry.
hcp	Hexagonal close-packed: A close-packed crystal structure with hexagonal symmetry.
ε-Fe	Hexagonal close-packed iron: The high-pressure phase of iron that will be the focus of this thesis.

Table xvii.3. Variables that appear frequently in this thesis.

Variable	Common Units	Description
V	cm^3/mol; $Å^3$/mol	Volume: Unless otherwise stated, volume refers to a material's molar volume per atom at a given amount of compression; reported volumes from this study are determined from *in situ* x-ray diffraction and the definition of a hexagonal close-packed unit cell; a subscript *0* indicates some reference conditions; a subscript *i* indicates a single compression point.
ρ	g/cm^3	Density: A material's mass per unit volume at a given amount of compression; reported densities from this study are determined from our measured volumes and m = 56.95 g/mol for 95% isotopically enriched ^{57}Fe; a subscript *0* indicates some reference conditions. Another use of density refers to densities in the Earth, which are inferred from seismic observations of its normal modes and modeled as a function of depth in average Earth models like PREM (see acronym section above).
P	GPa; Mbar	Pressure: the amount of force applied per unit area; reported pressures from this study are determined from our measured volumes and an established equation of state for ε-Fe; in other studies, pressure is often determined using the compressional behavior of secondary pressure markers, such as ruby, gold, and other metals. Subscripts can indicate static pressure (P_v) as determined from an ambient temperature equation of state; thermal pressure (P_{th}) or its vibrational (P_{vib}) or electronic (P_{el}) components, which indicate the amount of internal pressure produced by thermal excitations of phonons or electrons,; superscripts can indicate either harmonic (h) or anharmonic (ah) contributions to a given component of thermal pressure.
K	GPa	Bulk modulus: a material's resistance to uniform compression, given by the 2nd-order volume derivative of the material's free energy; sometimes referred to as "incompressibility;" subscripts can indicate adiabatic (K_S) or isothermal (K_T) bulk moduli; its pressure derivative is indicated by a prime (K').
μ	GPa	Shear modulus: a material's resistance to shear stress, given by the ratio of shear stress to shear strain; sometimes referred to as "rigidity"; its pressure derivative is indicated by a prime (μ').

Variable	Common Units	Description
$D(E,V)$	1/eV	Phonon density of states (see acronym section above).
C	k_B/atom; meV/atom	Specific heat capacity: the amount of heat (energy) required to increase the temperature of a material by a given amount; subscripts indicate the vibrational (C_{vib}) or electronic (C_{el}) components of the specific heat capacity.
F	k_B/atom; meV/atom	Helmholtz free energy: a material's free (usable) energy at a fixed volume and temperature; subscripts indicate the vibrational (F_{vib}) or electronic (F_{el}) components of the free energy.
S_{vib}	k_B/atom; meV/atom	Vibrational entropy: the temperature derivative of a material's vibrational Helmholtz free energy at constant volume; proportional to the number of ways the internal coordinates of a system can be arranged to produce thermodynamically equivalent states, considering dynamical (phonon) effects.
U_{vib}	k_B/atom; meV/atom	Vibrational internal energy: the vibrational component of a material's total internal energy, which includes contributions from both kinetic and potential energies.
E_K	k_B/atom; meV/atom	Vibrational kinetic energy: the portion of material's internal energy that is produced by atomic motions (phonons).
$<u^2>$	Å^2	Mean-square atomic displacement: the amplitude of an atom's displacement around its equilibrium position, which is sensitive to chemistry, crystal structure, pressure, and temperature.
f_{LM}	--	Lamb-Mössbauer factor: a material's probability for recoilless absorption, which contains information about lattice dynamics and is closely related to $<u^2>$.
T_{LM}	K	Lamb-Mössbauer temperature: a parameter introduced to represent the high-temperature behavior of $<u^2>$.
v	km/s	Sound velocities: the velocity with which sound waves travel through a material; subscripts indicate either the Debye (v_D), compressional (v_p), or shear (v_s) sound velocities; v_D is an average sound velocity obtained directly from the phonon density of stations; v_p and v_s are related to v_D via the density and adiabatic bulk modulus, and are conceptually equivalent to seismic velocities measured in the Earth.

Variable	Common Units	Description
γ	--	Grüneisen parameter: the coefficient that relates a material's internal energy and thermal pressure; subscripts indicate vibrational (γ_{vib}) or Debye (γ_D) Grüneisen parameters; the former is related to the phonon density of states, and the latter is based on Debye's approximate description of the same spectrum.
$\ln\beta$	--	Reduced isotopic partition function ratio: the ratio of isotope ratios for a given material and for dissociated atoms at equilibrium; β-factors are related to the equilibrium fractionation factor and in turn, determine the distribution of isotopes in equilibrium processes.
α	$10^{-5}K^{-1}$	Thermal expansion coefficient: the change in volume that results from increasing temperature at constant pressure; subscripts indicate the vibrational contribution to the thermal expansion coefficient (α_{vib}).
δ_T	--	Anderson-Grüneisen parameter: the volume dependence of the thermal expansion coefficient; from thermodynamic definition, the Anderson-Grüneisen parameter is proportional to the temperature derivative of the bulk modulus.

Chapter 1

Introduction

1.1 The Earth's Core

The Earth's core accounts for approximately one-sixth of the Earth's volume and one-third of its mass. We cannot directly sample such great depths in the Earth, so we rely largely on seismology to probe this remote region. Seismic observations of Earth's normal modes provide constraints on the density of the deep Earth, and body-wave travel times are related to the velocity at which compressional and shear sound waves travel through it. Such observations have revealed that to first order, the Earth comprises four basic layers: crust, mantle, outer core, and inner core (Figure 1.1). More specifically, the seismically inferred sharp increase in density across the core–mantle boundary suggests that the Earth's core is compositionally distinct from the overlying mantle. In addition, it has been determined that while Earth's inner and outer cores are likely to be compositionally similar based on their comparable densities, they have very different elastic properties. Shear waves do not propagate through the outer core, but they reappear in the inner core, thus implying that a liquid outer core surrounds the solid inner core. Further evidence for a liquid outer core lies in geodynamo theory, which argues that the Earth's magnetic field is

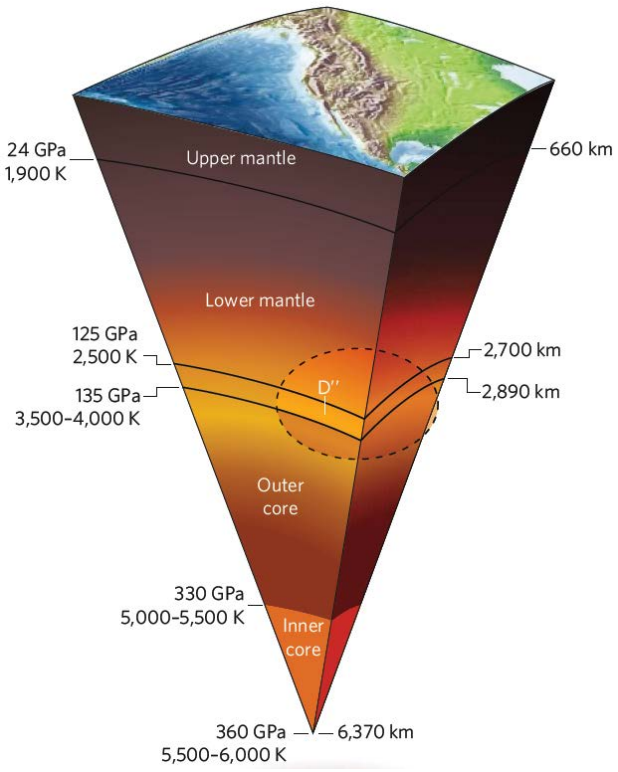

Figure 1.1. Cut-out model of the Earth. The four basic layers of Earth's interior are the crust; the silicate-rich mantle, which is often divided further into an upper mantle (P < 24 GPa) and lower mantle (24 GPa < P < 135 GPa); the liquid metallic outer core (135 GPa < P < 330 GPa); and the solid metallic inner core (330 GPa < P < 364 GPa). We note that the pressure at the center of the Earth is mislabeled. Figure taken from *Duffy* (2008).

generated by the rotation and vigorous convection of an electrically conductive fluid (i.e., the iron-rich liquid outer core) deep in the Earth.

The combination and inversion of astronomic-geodetic data (e.g., radius, mass, and moment of inertia) with observed free oscillations, long-period surface waves, and body-wave travel times results in average Earth models. These models assume a radially symmetric Earth (i.e., they are one-dimensional), and therefore they do not contain any information about lateral variations of the Earth's elastic properties. Instead, average Earth models provide information about the average elastic properties of deep Earth materials, in addition to estimates for the depths (pressures) of major boundaries that correspond to discontinuities in the inferred elastic and structural properties.

Two of the most commonly cited average Earth models are AK135 (*Kennett et al.*, 1995) and the Preliminary Reference Earth Model (PREM) (*Dziewonski and Anderson*,

1981). There are slight differences between AK135 and PREM near the boundaries between distinct layers in the deep Earth, but overall they agree on the general features (Figure 1.2). For example, they place the core–mantle boundary (CMB) at a depth of 2891 km—which corresponds to a pressure of ~136 GPa—where there is a sudden increase in density by 78%, a decrease in compressional wave velocity by 41%, and the complete disappearance of shear waves. In addition, they find the boundary between the solid inner core and the liquid outer core (inner–core boundary; ICB) to be at a depth of 5150 km (329 GPa), based on the reappearance of shear seismic waves and smaller discontinuities

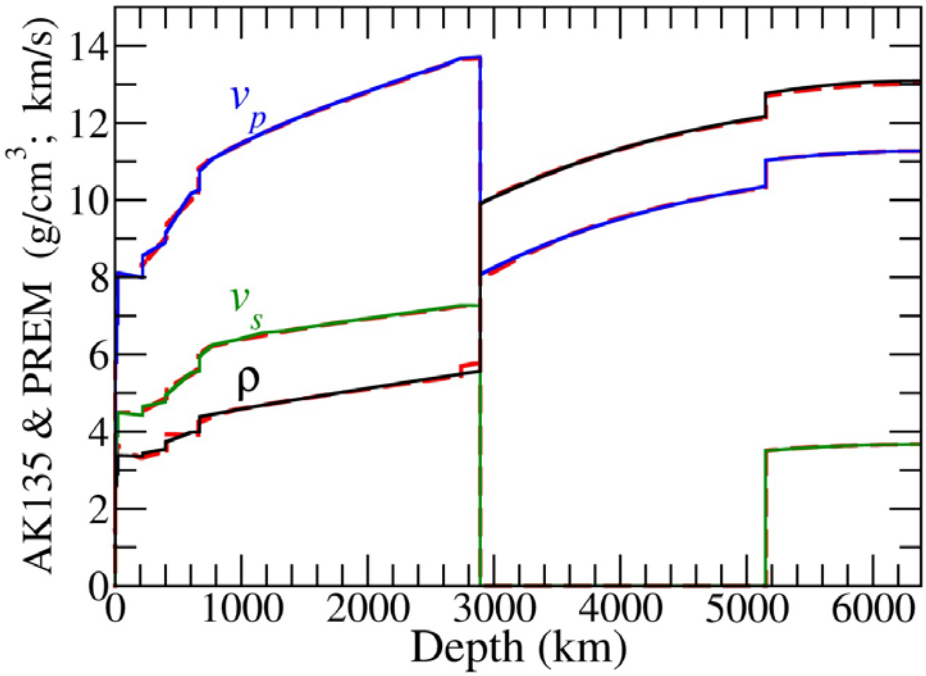

Figure 1.2. Average Earth models. The density (ρ, black) and compressional (v_p, blue) and shear (v_s, green) sound velocities predicted by the Preliminary Reference Earth Model (PREM) are plotted as a function of depth (*Dziewonski and Anderson*, 1981). Predictions for the same quantities from AK135 (*Kennett et al.*, 1995) are plotted as red dashed lines beneath the PREM curves, for comparison. We note that the most prominent differences between the two plotted seismic models occur near major boundaries in the Earth, such as the transition zone and the core–mantle boundary, the latter of which corresponds to the sharp discontinuity at a depth of 2891 km. In addition, we point out that v_s = 0 between 2891 and 5150 km depth, because shear waves cannot propagate through the liquid outer core; the latter depth corresponds to the inner–core boundary.

in the density (~5%) and compressional wave velocities (~6.5%) (e.g., *Dziewonski and Anderson*, 1981). Finally, within a given layer, models like PREM and AK135 provide radial density and velocity profiles (Figure 1.2), which are related to the composition of these remote regions via comparison with theoretical and experimental investigations of the structural and thermoelastic properties of candidate materials.

From arguments based on seismic observations, laboratory experiments, and cosmochemical observations, iron is considered to be the main constituent in Earth's core (e.g., *Birch*, 1964; *McDonough*, 2003). We will return to a discussion of the more minor constituents in the core in Section 1.3, but for now we focus on our current understanding of the high-pressure properties of pure iron. Pure iron crystallizes in the body-centered cubic (bcc; α-Fe) crystal structure at ambient pressure and temperature (*PT*) conditions. At ambient pressure, iron transitions to the face-centered cubic structure (γ-Fe) at ~1185 K (e.g., *Birch*, 1940), and then back to a bcc structure (δ-Fe) at ~1667 K before melting around 1811 K (e.g., *Strong et al.*, 1973) (Figure 1.3). At low temperatures, iron undergoes a single phase transition to the more densely packed hexagonal close-packed structure (hcp; ε-Fe) around 10 to 18 GPa (e.g., *Bancroft et al.*, 1956; *Stixrude et al.*, 1994; *Dewaele et al.*, 2006; *Sha and Cohen*, 2006). Finally, the crystal structure at simultaneous high-pressure and temperature conditions is somewhat controversial (e.g., *Saxena and Dubrovinsky*, 2000), but existing data suggest that ε-Fe is the stable phase at core condition (e.g., *Vočadlo et al.*, 2000; *Alfè et al.*, 2001; *Ma et al.*, 2004; *Nguyen and Holmes*, 2004; *Tateno et al.*, 2010). Therefore, firmly establishing the high-pressure material properties of ε-Fe—the end-member composition of the core—with high-pressure experiments is essential for improving our understanding of a significant fraction of this remote region.

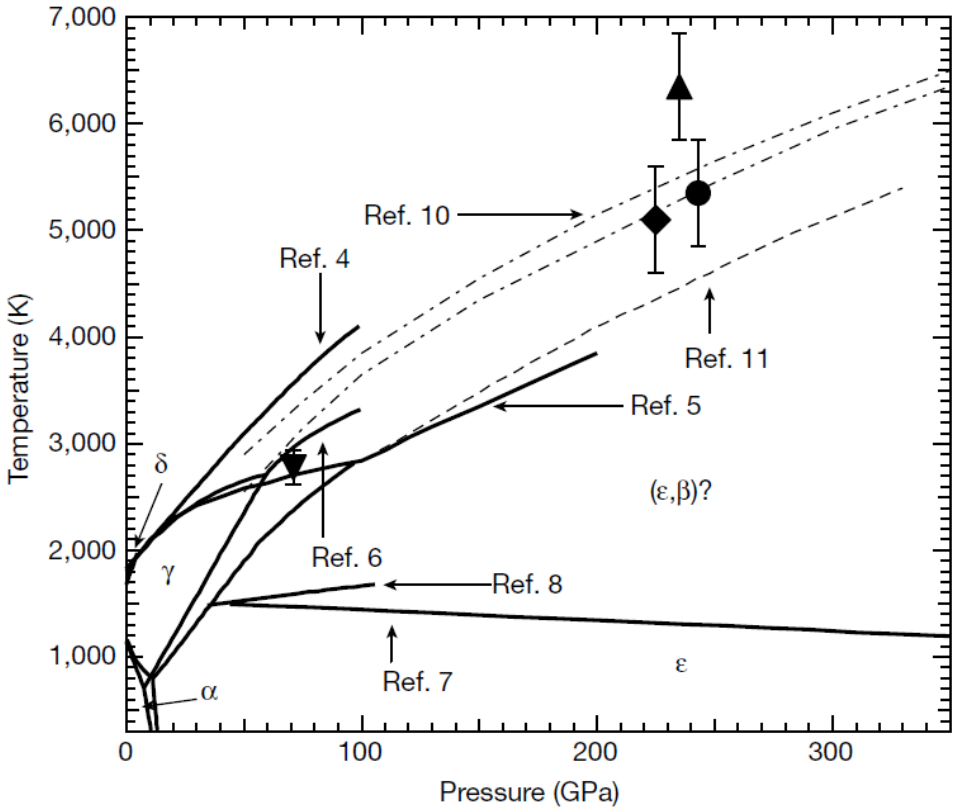

Figure 1.3. Pressure–temperature phase diagram of iron. At ambient conditions, iron takes on the bcc structure (α); at low-*P* and high-*T* conditions, iron transforms first into an fcc structure (γ) and then back to a bcc structure (δ); at low-*T* and high-*P* conditions, iron transforms into an hcp structure (ε); the crystal structure of iron at high-*PT* conditions remains controversial, although there is significant evidence that ε-Fe remains stable throughout the *PT* conditions of Earth's core (e.g., *Tateno et al.*, 2010). Figure taken from *Nguyen and Holmes* (2004) and associated references within.

1.2 Investigating Iron at Earth's Core Conditions

A wide variety of techniques have been used to investigate the structural, vibrational, and thermoelastic properties of ε-Fe. Shock-compression experiments have historically been the preferred method for experimentally probing the properties of candidate core materials, in part, because they simultaneously induce the pressure and temperature conditions expected in Earth's core (~136 to 364 GPa, $T > 2500$ K). In such experiments, pressures are generated by dynamically impacting an iron sample with a

"flyer" that has been accelerated toward it using, e.g., a two-stage light gas gun. Across the resulting shock front, iron undergoes a nearly discontinuous, adiabatic change of state, from which one can investigate the pressure-volume-internal energy equation of state (e.g., *McQueen et al.*, 1970), adiabatic bulk modulus (e.g., *Jeanloz*, 1979), compressional sound velocity (e.g., *Jeanloz*, 1979; *Brown and McQueen*, 1986; *Nguyen and Holmes*, 2004), and melting behavior (e.g., *Brown and McQueen*, 1986; *Williams et al.*, 1987; *Yoo et al.*, 1993; *Ahrens et al.*, 2002; *Nguyen and Holmes*, 2004) of ε-Fe at simultaneous high-pressure and temperature (*PT*) conditions. For shocks that are large enough to induce melting of iron, one can also probe the high-*PT* bulk sound velocity and Grüneisen parameter of the liquid phase (e.g., *Jeanloz*, 1979; *Brown and McQueen*, 1986; *Nguyen and Holmes*, 2004).

The induced pressures, sample densities, and internal energies from shock-compression experiments are very well-known via the measured shock velocity, particle (sample) velocity, and initial pressure and density of the system, but it is difficult to accurately determine the temperature of a given shock. For transparent materials, the shock temperature can be measured fairly accurately (ΔT ~ 50 K at 4000 K) using time-resolved optical pyrometry (e.g., *Luo et al.*, 2004). Determining the shock temperature for an opaque sample is much more challenging, so for experiments on ε-Fe, it is often approximated from thermodynamic calculations that use estimated values for ε-Fe's Grüneisen parameter and heat capacity. Reported temperature uncertainties from this method are typically on the order of ~500 K (e.g., *Brown and McQueen*, 1986; *Nguyen and Holmes*, 2004).

A complementary approach to investigating thermoelastic and thermodynamic properties at core pressures is to use static compression in the diamond-anvil cell (DAC; see Section 2.1 for details on the DAC). Static-compression experiments can achieve

similar pressures as those produced with shock compression, but they are performed at constant volume rather than constant entropy. In addition, the nature of static compression allows for independent manipulation of pressure and temperature and, in turn, a more controlled sampling of *PT* conditions. However, determining the pressure experienced by the sample in a DAC is difficult, and reported pressures are often based on calibrated pressure scales for secondary pressure markers that disagree significantly at core pressures (e.g., *Steinle-Neumann et al.*, 2001; *Dorogokupets and Oganov*, 2006). The recorded pressure from a secondary pressure marker is also sensitive to the sample chamber environment (i.e., degree of hydrostaticity), so additional uncertainties are introduced to reported pressures based on the DAC preparations for a given experiment. For example, the pressure experienced by the sample may be significantly different than that experienced by the secondary pressure marker, which is most often not the sample itself.

A wide variety of DAC techniques have been used to investigate the high-pressure structural and thermoelastic properties of iron. Synchrotron x-ray diffraction (XRD) has been used to investigate the crystal structure and compressibility of ε-Fe, the combination of which gives rise to its isothermal equation of state (e.g., *Mao et al.*, 1990; *Dewaele et al.*, 2006). In addition, the use of a laser-heated DAC allows for the investigation of ε-Fe's thermal equation of state and melting behavior via high-*PT* XRD experiments (*Dubrovinsky et al.*, 1998; *Shen et al.*, 1998; *Uchida et al.*, 2001; *Ma et al.*, 2004; *Tateno et al.*, 2010). High-pressure Raman spectroscopy has been used to measure ε-Fe's E_{2g} Raman mode, which is correlated with a transverse acoustic phonon and, in turn, provides information about its shear sound velocity (*Merkel et al.*, 2000). Inelastic x-ray scattering (IXS) has been used to probe iron's compressional wave velocity via the inelastic scattering

of x-rays by long-wavelength acoustic phonons (e.g., *Antonangeli et al.*, 2004). In general, IXS can be used to investigate the elastic constants and shear sound velocities of single crystals, but single crystals are not preserved across iron's α→ε phase transition, and thus are not available for ε-Fe. For IXS measurements on polycrystals, the shear mode is extremely difficult to detect, typically because the background is too high or elastic scattering dominates at low energies. Finally, nuclear resonant inelastic x-ray scattering (NRIXS) is an especially powerful technique that probes the total phonon density of states of select resonant isotopes and, in turn, their sound velocities and vibrational thermodynamic properties. Somewhat fortuitously for the Earth Science community, ^{57}Fe is one such isotope, and therefore has been the focus of many high-pressure NRIXS studies (e.g., *Lübbers et al.*, 2000; *Mao et al.*, 2001; *Giefers et al.*, 2002; *Lin et al.*, 2005; *Mao et al.*, 2008; *Murphy et al.*, 2011b). NRIXS experiments of ε-Fe will be the focus of this study, and will be described in more detail in Chapter 2.

Finally, many theoretical studies have been dedicated to investigating the structural, thermoelastic, and thermodynamic properties of iron at core conditions. In particular, *ab initio* techniques have been applied by a number of research groups to investigate the Helmholtz free energy (*F*) and, in turn, the equation of state, thermodynamic, and thermoelastic properties of ε-Fe (e.g., *Wasserman et al.*, 1996; *Stixrude et al.*, 1997; *Alfè et al.*, 2001; *Vočadlo et al.*, 2009; *Sha and Cohen*, 2010a). From the volume dependence of *F*, these studies explored the specific heat capacity, bulk modulus, thermal expansion coefficient, and Grüneisen parameter of ε-Fe up to pressures of 400 GPa and temperatures of 8000 K, often producing significantly different results at core conditions. Access to such extreme conditions highlights a major advantage of theoretical calculations: the *PT* range

they have access to is much larger than that of most experiments. However, the utility of theoretical studies at such conditions is limited by their lack of confirmation from experimental results; in general, it is via benchmarking against experiments that the accuracy of theoretical calculations is discussed.

Another important strength of theoretical calculations is their ability to probe properties that are difficult or impossible to measure experimentally at *in situ* high-*PT* conditions. For example, theoretical calculations provide the most complete information about the pressure and temperature dependences of ε-Fe's elastic moduli (e.g., *Vočadlo et al.*, 2009; *Sha and Cohen*, 2010a). In addition, they are currently the sole source of information about electronic contributions to the thermodynamic and thermoelastic properties of ε-Fe at high-*PT* conditions, since experimental techniques that probe the electronic density of states require a free sample surface.

Despite the wealth of data provided by theoretical, shock-compression, and static-compression experiments—and in part because of it—many of the properties of iron at the *PT* conditions of Earth's core remain highly uncertain. For example, there is an ongoing debate about the crystal structure of iron at Earth's core conditions; many studies support the stability of ε-Fe, but a variety of solid–solid phase transitions have been suggested as a result of both static- and shock-compression experiments (e.g., *Brown and McQueen*, 1986; *Anderson and Isaak*, 2000; *Andrault et al.*, 2000; *Dubrovinsky et al.*, 2000b; *Saxena and Dubrovinsky*, 2000). In addition, even if we assume ε-Fe remains stable throughout Earth's core, there is significant disagreement between theoretical (e.g., *Vočadlo et al.*, 1997; *Sola et al.*, 2009; *Sha and Cohen*, 2010a) and experimental (e.g., *Brown and McQueen*, 1982; *Mao et al.*, 1990; *Dubrovinsky et al.*, 1998; *Uchida et al.*, 2001; *Dewaele et al.*, 2006)

determinations of its equations of state (EOS). The ambient pressure volume (V_0), isothermal bulk modulus (K_{T0}), and pressure derivative of the isothermal bulk modulus (K_{T0}') from various static-compression experiments seem to be converging around V_0 ~ 6.75 cm^3/mol, K_{T0} ~ 160 to 165 GPa, and K_{T0}' ~ 5.33 to 5.38 (e.g., *Dewaele et al.*, 2006). However, many theoretical calculations of ε-Fe's EOS report dramatically different EOS parameters: V_0 ~ 6.08 cm^3/mol, K_{T0} ~ 290 GPa, and K_{T0}' ~ 4 to 4.44 (e.g., *Sha and Cohen*, 2010a). Such discrepancies result in significantly different predicted pressures for a given volume at small compressions ($V/V_0 \geq 0.85$) (*Dewaele et al.*, 2006; *Sha and Cohen*, 2006), and are due, in part, to the fact that theoretical calculations predict ε-Fe remains magnetic until ~50 GPa. Another likely factor is the trade-off between K_{T0} and K_{T0}' when fitting an EOS to pressure–volume relationships measured with static-compression experiments.

Finally, we note that the predicted melting temperatures for ε-Fe at the pressure of Earth's inner–core boundary (330 GPa) span a range of almost 3000 K: from 4850 ± 200 K (*Boehler*, 1993) to 7600 ± 500 K (*Williams et al.*, 1987). Many studies have found the melting temperature of ε-Fe falls in a slightly narrower range of ~5000 to 6000 K (e.g., *Brown and McQueen*, 1986; *Shen et al.*, 1998; *Laio et al.*, 2000; *Ma et al.*, 2004; *Nguyen and Holmes*, 2004; *Murphy et al.*, 2011a; *Jackson et al.*, 2012). However, recent reports have predicted melting temperatures consistent with both the upper (*Sola and Alfè*, 2009) and lower (*Komabayashi and Fei*, 2010) bounds of the original range, suggesting that we are not yet converging on a single melting point for ε-Fe at Earth's core conditions.

1.3 Alloying and Temperature Effects of Iron

Determining the properties of Earth's core becomes even more complicated when one considers the fact that the end-member composition is not an accurate representation of

the overall composition. In addition to iron, the core is thought to contain ~5 to 10 wt% Ni and some light elements (e.g., H, C, O, Si, S), based in part on elemental ratios measured in iron meteorites (*McDonough*, 2003). The presence of light elements is further supported by the fact that the inferred density of the core is smaller than that of pure iron (e.g., *Birch*, 1964; *Jeanloz*, 1979; *Mao et al.*, 1990; *Stixrude et al.*, 1997; *Laio et al.*, 2000; *Dewaele et al.*, 2006). In addition, the sound velocities and pressure and temperature derivatives inferred for the core do not match those measured for pure iron (e.g., *Dziewonski and Anderson*, 1981; *Brown and McQueen*, 1986; *Mao et al.*, 2001; *Antonangeli et al.*, 2004).

The identity and amount of alloying elements present in the core is a highly underdetermined problem, so the focus of experimental and theoretical efforts has been divided over a long list of candidate compositions. Perhaps the most obvious composition to explore after pure iron is Fe-Ni, whose structural and elastic properties have been investigated with a variety of techniques, e.g., XRD (*Mao et al.*, 1990), IXS (*Kantor et al.*, 2007), and NRIXS (*Lin et al.*, 2003c). However, the three studies listed above measured the properties of iron alloyed with 20, 23, and 7.5 wt%, respectively; therefore, while discussion can involve results from all three experiments, additional uncertainties are introduced because of the different overall compositions, starting materials, and synthesis procedures. The situation is similar for investigations of iron alloyed with candidate light elements, such as Fe-H (e.g., *Hirao et al.*, 2004a; *Mao et al.*, 2004; *Narygina et al.*, 2011; *Shibazaki et al.*, 2012), Fe-C (e.g., *Scott et al.*, 2001; *Fiquet et al.*, 2009; *Sakai et al.*, 2011), Fe-O (e.g., *Struzhkin et al.*, 2001; *Badro et al.*, 2007; *Seagle et al.*, 2008; *Fischer et al.*, 2011; *Ohta et al.*, 2012), Fe-Si (e.g., *Lin et al.*, 2003c; *Hirao et al.*, 2004b; *Badro et al.*, 2007; *Asanuma et al.*, 2010), and Fe-S (e.g., *Williams and Jeanloz*, 1990; *Lin et al.*, 2004;

Badro et al., 2007; *Campbell et al.*, 2007; *Morard et al.*, 2008). Finally, it is only fairly recently that experimental studies have considered iron alloyed with multiple elements (i.e., Ni and a light element, or more than one light element) (e.g., *Antonangeli et al.*, 2010; *Asanuma et al.*, 2011; *Huang et al.*, 2011; *Sakai et al.*, 2011; *Terasaki et al.*, 2011), which is likely to be closer to an accurate description of the core's composition. More discussion on the effects of alloying nickel and light elements with iron is presented in Chapter 6.

Another important factor that must be addressed in future experiments is the effects of temperature on the aforementioned properties of ε-Fe. Theoretical studies have been investigating the properties of iron and iron alloys at the *PT* conditions of Earth's core for over a decade, but discrepancies exist and confirmation with experimental results is essential. Shock-compression experiments are capable of achieving such experimental conditions, but suffer from the previously discussed challenge of accurately determining the shock temperature for opaque materials. DAC experiments at simultaneous high-*PT* conditions remain challenging to execute and interpret, but select experiments have been performed at the conditions of Earth's solid inner core (e.g., *Tateno et al.*, 2010; *Terasaki et al.*, 2011). As the precision of DAC preparations continues to increase, we can anticipate more high-*PT* experiments that investigate a wider variety of candidate core compositions.

1.4 Scope of Thesis

It is now clear that exploring the structural, thermoelastic, and thermodynamic properties of core materials at Earth's core conditions is a complex problem. To simplify it, the focus of this thesis will be on firmly establishing the high-pressure properties of pure iron up to an outer core pressure of 171 GPa. The ultimate goal is that our measurements and results of our analyses will provide a quality baseline for future investigations of the

effects of alloying and temperature.

In order to probe the thermoelastic and vibrational thermodynamic properties of ε-Fe, we measured the volume dependence of its total phonon density of states with nuclear resonant inelastic x-ray scattering (NRIXS) and *in situ* x-ray diffraction (XRD) experiments. Details of our experimental methods can be found in Chapter 2. Based on our NRIXS and *in situ* XRD data, we present the derivation and discussion of the following parameters for ε-Fe:

- Thermal pressure (P_{th}) is the increase in internal pressure that results from the thermal excitation of electrons and phonons. In the context of Earth's core, knowledge of ε-Fe's P_{th} is necessary for determining the density of iron at the pressure and temperature conditions of Earth's core. In turn, P_{th} is related to the amount of light elements that must be present in the core to match seismically inferred values for the density of this remote layer (Chapter 3).
- As previously discussed, the high-pressure melting behavior of iron is an important quantity for constraining the temperature of the inner–core boundary, where Earth's solid inner core and liquid outer core are in contact. Our experiments are performed at ambient temperature so we do not directly probe melting, but we investigate ε-Fe's melting curve shape via parameters obtained from our measured phonon DOS (Chapter 3).
- The vibrational Grüneisen parameter (γ_{vib}) relates vibrational components of the thermal pressure and thermal energy per unit volume, and is often used to extrapolate available melting points to higher pressures. We investigate both γ_{vib} and the approximate Debye Grüneisen parameter via the volume dependence of

the total phonon DOS and its low-energy region, respectively. Comparison of these two quantities allows us to evaluate the accuracy of the Debye model for ε-Fe (Chapter 4).

- The reduced isotopic partition function ratios (β-factors) of ε-Fe provide information about the distribution of heavy isotopes during equilibrium processes involving crystalline iron. We investigate ε-Fe's β-factors as a function of pressure and temperature, with an emphasis on understanding the available resolution at the conditions of Earth's lower mantle (Chapter 5).
- The thermal expansion coefficient (α) is important for discussions of Earth's core via its close relationship with both P_{th} and γ_{vib}. Determination of α thus provides a self-consistent check on these parameters, and allows us to convert between isothermal and adiabatic bulk moduli, which is necessary for determining accurate sound velocities from the phonon DOS (Chapter 5).
- Accurate knowledge of the sound velocities of ε-Fe is essential because they provide one of the most direct means for comparison with seismic observations of Earth's core. We determine the Debye sound velocity from the low-energy region of the phonon DOS and, in turn, obtain values for its compressional and shear sound velocities via our measured density, γ_{vib}, and α_{vib}. We compare our sound velocities directly with those reported for iron alloys at 300 K, and approximate their high-temperature behavior in order to make comparisons with seismic velocities in Earth's solid inner core (Chapter 6).

Chapter 2

Experiments

The data presented in this thesis were collected at synchrotron radiation facilities in the United States. The majority of our experiments were conducted at the Advanced Photon Source (APS) at Argonne National Laboratory, Argonne, Illinois; select measurements were made at the Advanced Light Source (ALS) at Lawrence Berkeley National Laboratory, Berkeley, California. Experimental preparations were performed in the Diamond Anvil Cell Laboratory at the California Institute of Technology, Pasadena, California, prior to each experimental run.

2.1 Static Compression

For all compression studies, the pressure experienced by a sample is equal to the force imposed upon it divided by the area over which the force is applied: $P = F/A$. Therefore, the extreme pressures of planetary interiors can be achieved by either (1) applying a very large force, or (2) applying a lesser force over a very small area. Both methods are capable of generating hundreds of gigapascals (GPa) of pressure, including pressures beyond those expected for the center of the Earth (364 GPa).

As previously discussed (Section 1.2), shock-compression experiments fall into

category (1). The pressure in a given experiment is generated by dynamically impacting the sample, and scales with the acceleration (force) of the impactor. We reiterate that such impacts result in a simultaneous increase in pressure and temperature, and an adiabatic change of state of the sample. On the other hand, static-compression experiments (e.g., Paris-Edinburgh press, multi-anvil press, and diamond-anvil cell) are based on method (2). The relevant area in a diamond-anvil cell (DAC) experiment is the culet of a gem-quality diamond, which typically has a diameter on the order of 50 to 500 μm. In DAC experiments, a small force applied to the table (back) of the diamond is transferred to the culet and, in turn, the pressure-transmitting medium that is in contact with the culet and fully encloses the sample. Therefore, the force required for inducing 100 GPa of pressure on a 100 μm culet is on the order of ~800 N. As previously discussed in Section 1.2, DAC experiments are performed at constant volume (as opposed to constant entropy), and allow one to easily define the pressure resolution (step size) in an experimental series. In addition, manipulation of temperature is independent of the means for inducing pressure, thus allowing for a more controlled sampling of *PT* space.

2.1.1 Panoramic Diamond-Anvil Cell (DAC) Assembly

Many different DACs have been designed to meet the requirements of various experimental geometries and setups. The experimental technique that will be the focus of this thesis—nuclear resonant inelastic x-ray scattering (NRIXS)—requires a panoramic DAC (Figure 2.1). The main feature of a panoramic DAC is that is has large “windows” cut out of the cylinder, so that detectors can be brought in very close to (~2 cm from) the compressed sample without compromising the ability to apply a uniform force to the sample chamber and, in turn, generate pressure. The components involved in a complete

Figure 2.1. Panoramic Diamond-Anvil Cell (DAC). This panoramic DAC was designed and machined at Caltech. The cylinder side of the panoramic DAC is on top in this picture, and the 90º opening for *in situ* XRD is visible. The most prominent feature is the large "window" that is cut out of the cylinder to allow detectors to be brought in very close to (~2 cm from) the sample for high-pressure NRIXS experiments. The two opposing diamond anvils are mounted onto seats using the procedure described in the text; pink numbers reflect the three "orientations" of the DAC that are available; and the small disk between the diamonds is the Be gasket.

panoramic DAC assembly are 1 piston, 1 cylinder, 2 diamonds, 2 seats, mounting epoxy, aligning screws, 2 set screws, mounting putty, 1 beryllium gasket, 1 boron epoxy insert, and 4 tightening screws.

To prepare a panoramic DAC for NRIXS experiments, one begins by mounting the diamonds to the seats, or backing plates. Gem quality diamonds that are ~2 mm thick are used because of their superior hardness and bulk modulus, transparency at optical and typical x-ray energies (wavelengths), and thermal properties, all of which are essential for performing experiments at *in situ* high-pressure and temperature conditions. Seats are commonly made from tungsten carbide (WC) or cubic boron-nitride (cBN) ceramic materials, which also have large bulk moduli and hardness values. A significant difference between them is that at typical x-ray energies, WC is highly absorbing while cBN is largely transparent. For high-pressure NRIXS experiments, the majority of the signal is collected in the radial direction (i.e., photons that are detected after passing through the gasket material rather than the seat), so it is possible for the downstream seat to be x-ray

absorbing. However, a cBN seat is preferable over WC on the downstream side of the DAC if one plans to collect *in situ* x-ray diffraction (XRD), in order to maximize the range of accessible diffraction angles. For a similar purpose, our panoramic DACs are also specially designed with a 90º opening on the downstream side (Figure 2.1; Section 2.2).

To mount a diamond, the diamond and seat are thoroughly cleaned, and a mounting jig is used to align and secure the diamond roughly in the center of the seat. A mixture of Stycast 2651 resin and a catalyst in a ratio of 100:7 by weight—prepared immediately before diamond mounting—is made to serve as the "glue" between the diamond and the seat. The epoxy should cover the girdle of the diamond and fill in between the girdle and the seat, but in order to maximize stability of the anvil, the epoxy cannot seep between the table and the seat (Figure 2.2). When the epoxy is in place, the seat is placed on a heating plate to allow the epoxy to harden overnight on a low-heat setting.

Once the diamonds have been secured to their seats, they are positioned in the piston and cylinder sides of the panoramic DAC (e.g., Figure 2.1) using the aligning screws, which hold the seats flush against the base of the DAC. The cylinder (i.e.,

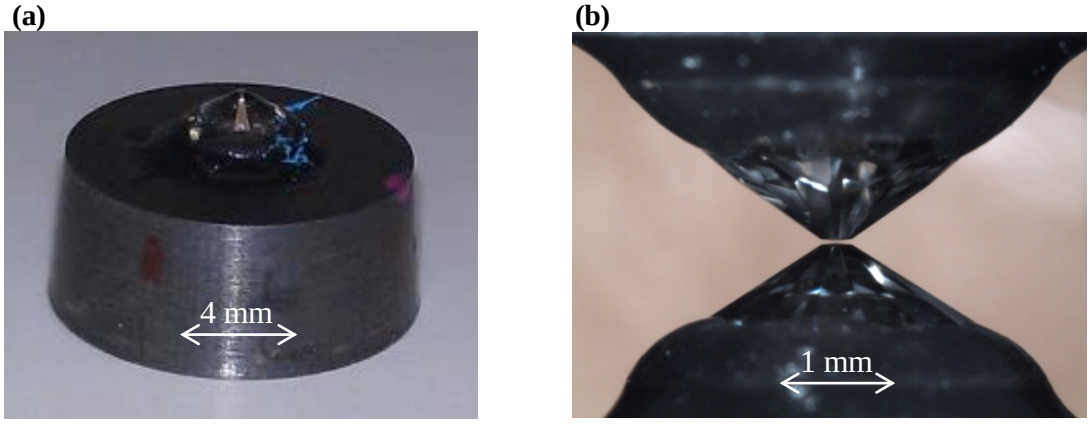

Figure 2.2. Diamond mounting and alignment. (a) A black resin is used to mount diamond anvils to a seat; shown here are a WC seat and a diamond with culet diameter of ~100 μm and bevel diameter of 300 μm. (b) Mounted diamonds (of the same dimensions) are aligned in the microscope to bring the culets directly on top of one another; this image provides a close-up view of the resin and anvils.

downstream in an NRIXS experiment) is equipped with six aligning screws, while the piston (upstream) only has four. Therefore, common practice is to first secure the diamond on the cylinder side, and then adjust the aligning screws on the piston side—while looking through the cylinder-side diamond using a high-magnification microscope—to bring the culets directly on top of each other. By looking through the microscope while the DAC is on its side, one can measure the spacing between the culets and perform this alignment procedure at a variety of spacings, e.g., 500, 200, 100, 30, and 10 μm. Finally, the alignment of the diamonds is confirmed while they are in contact, and their parallelness is checked by investigating whether any optical fringes are visible. If ≥2 full fringes are visible, the alignment process can be repeated, or a new orientation of the piston with respect to the cylinder can be chosen. Since there are three "windows" in the panoramic DAC, there are three possible orientations that allow for placement of the detectors during an NRIXS experiment (Figure 2.1); in some DACs, one orientation may produce a better and more reproducible alignment than the others.

The next step is to prepare a beryllium gasket, which will serve as the walls of the sample chamber in the DAC. Beryllium (Be) is a hazardous and very soft material, which makes DAC preparations difficult and limits the pressure range over which the DAC remains stable. However, the scattered photons in an NRIXS experiment must pass through the gasket to reach radially positioned detectors (e.g., Figure 2.4), so the more common, x-ray absorbing gasket materials cannot be used (e.g., stainless steel and rhenium). Early Be gaskets that were machined for NRIXS experiments were 5 mm in diameter. We use specially designed Be gaskets that are 3 mm in diameter and machined with a ~400 μm flat area in center that is ~100 μm thick. The smaller diameter results in less absorption of

scattered photons, while the flat area in the center allows for the gasket to rest stably in a horizontal position on the diamond culets before (and during) indentation.

Preparation of a Be gasket for high-pressure NRIXS experiments involves (1) pre-indenting the gasket, (2) drilling a hole in the center of it, and (3) applying an insert made of a stiff, low-atomic number material, e.g., boron-epoxy, cBN, or diamond. To pre-indent the Be gasket, one begins by supporting it on a ring of mounting putty and centering the flat area over the culets. Indenting the Be gasket to a thickness of ~35 μm work-hardens it prior to the experiment, resulting in an increased resistance to further deformation during the experiment and, in turn, improves the chances of achieving higher pressures. A sample chamber is produced by drilling a hole in the Be gasket using electrical discharge machining; the drill hole diameter should be ~1/3 of the culet diameter (D_{culet}) for $D_{culet} \geq$ 250 μm, and equal to or slightly larger than the culet size for $D_{culet} <$ 250 μm. For larger culet sizes, a sample chamber large enough for precision sample loading will fit easily into the center of the culet, leaving some room for sample chamber migration during compression. For smaller culets, e.g., $D_{culet} =$ 150 μm, a sample hole that would fit onto the culet makes sample loading very challenging. Therefore, for small culet sizes, we drill roughly the entire culet and fill in the hole with the insert material, which reinforces the shape and size of the sample chamber—thus avoiding rapid thinning of the sample during compression—as a result of the insert's high shear strength.

For our high-pressure NRIXS experiments, we use a boron-epoxy insert material because it is less absorbing at the relevant x-ray energies (~14.4 keV) than cBN and diamond. To make the boron-epoxy, one mixes amorphous boron and epoxy (in a ratio of 3.5:1 by weight) with acetone in a mortar until they are well combined (*Lin et al.*, 2003b).

This procedure should be done under a fume hood and immediately before the first insert is to be loaded, since the boron-epoxy tends to dry out and become difficult to work with. Extra boron-epoxy material can be stored under acetone for loading in the days after it is made. To make the insert, one loads a small piece of the boron-epoxy into the drilled hole in the Be gasket and compresses it between the diamonds. The insert should fill the entire hole; spilling over onto the gasket material is fine as long as its distribution is roughly even and symmetric. Finally, a tungsten loading needle is used to drill a smaller hole in the boron-epoxy insert, which will serve as the sample chamber. We note that tungsten is used to avoid ^{57}Fe contamination, which could occur if a stainless steel loading needle is used.

The ideal sample for a high-pressure NRIXS experiment is isotopically enriched in the resonant isotope (^{57}Fe in our case), and has a starting thickness between 10 to 20 μm. Both allow for optimal counting rates, while this sample thickness prevents absorption of the forward scattering signal and significant sample thinning during compression. Ideally, the sample will be in the center of the culet and not in contact with the gasket or insert materials, to avoid pressure gradients. When necessary, a few ruby spheres or a piece of gold will also be loaded as secondary pressure markers, to allow for offline monitoring while increasing the pressure (e.g., *Mao et al.*, 1986; *Dorogokupets and Oganov*, 2003; 2006). However, rubies and gold are relatively absorbing materials at ~14.4 keV, and thus reduce the counting rates of the NRIXS signal. Therefore, we do not load a secondary pressure marker for our NRIXS experiments on ε-Fe, and instead monitor the pressure in the sample chamber offline (e.g., while increasing the pressure) using the high-frequency Raman edge of the diamond from the center of the culet (e.g,. *Akahama and Kawamura*, 2006). We note that our final reported pressures are based on our *in situ* measured volumes

of ε-Fe and do not depend on the diamond edge calibration.

The final (optional) step is to load a quasi-hydrostatic pressure-transmitting medium into the sample chamber. For example, pressurized helium and neon gas–loading facilities are available at GeoSoilEnviroCARS (GSECARS) sector of the APS. If the experiment does not require quasi-hydrostatic conditions, or the size or geometry of the sample chamber does not allow for it, then the sample can also be fully embedded in the boron epoxy insert. To close the DAC and increase the pressure, one uses the tightening screws. By turning them in sequence two at a time, one applies a parallel force to the diamonds—and, in turn, the metal gasket—which improves the stability of the sample chamber with compression.

2.1.2 Our Panoramic DAC Preparations

The analysis presented in this thesis is based on four preparations of modified panoramic diamond-anvil cells (DACs) with 90º openings on the downstream side (Figure 2.1) and beveled anvils with flat culet diameters of 250 or 150 μm. WC seats were used on the piston side of the DAC, and cBN seats were used on the cylinder (downstream) side to maximize the available diffraction angles for our *in situ* XRD experiments.

For the DACs assembled with 250 μm culets, 80 μm diameter holes were drilled and filled with boron epoxy. A hole was then drilled in the center of the insert to create the sample chamber using a loading needle. Into each sample chamber, a piece of 10 μm thick 95% enriched ^{57}Fe foil was loaded, with an area of ~20 × 30 μm. Hydrostatic conditions were achieved in the sample chamber for our experiments at molar volumes per atom of ^{57}Fe greater than 5.27 cm^3/mol ($P \leq 69$ GPa) via the loading of a neon pressure transmitting medium at the GSECARS sector of the APS (Figure 2.3). For measurements made at all

other compression points, the ^{57}Fe foil was fully embedded in the boron epoxy, which served as the pressure transmitting medium. The pressure in the sample chamber was monitored offline while increasing the pressure using the diamond-edge calibration (*Akahama and Kawamura*, 2006). The final reported pressure was determined from our *in situ* XRD and the Vinet equation of state (EOS) for ε-Fe reported by *Dewaele et al.* (2006). For the DACs assembled with 150 μm culet diameters, 125 μm diameter holes were drilled in the Be gaskets and filled with boron epoxy. A hole was then drilled in the center of the insert to create the sample chamber, into which a piece of 10 μm thick 95% enriched ^{57}Fe foil was loaded (~15 × 15 μm in area). Upon compression, the ^{57}Fe foil was fully embedded in the boron epoxy, which served as the pressure-transmitting medium. Again, no secondary pressure markers were loaded, and the pressure in the sample chamber was monitored offline while increasing the pressure using the diamond edge.

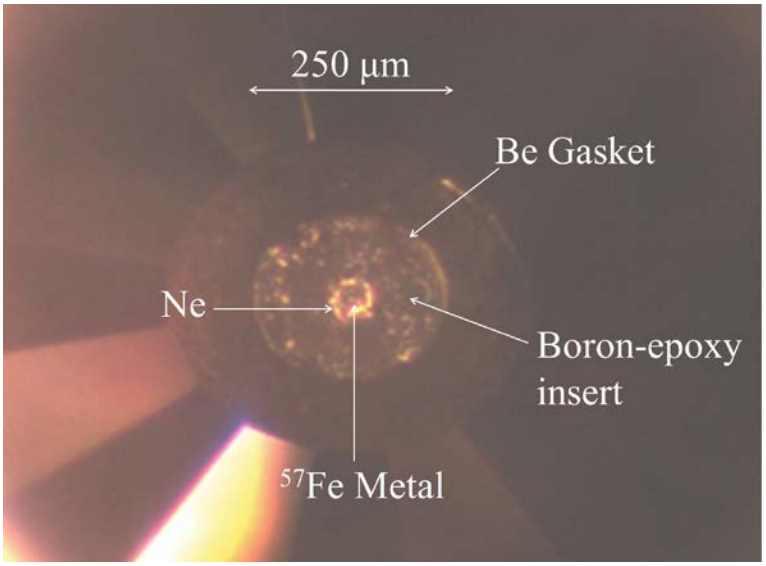

Figure 2.3. Sample chamber. For each panoramic DAC preparation, we pre-indented and drilled a Be gasket; loaded a boron-epoxy insert to maintain the thickness of the sample chamber with compression; and loaded into each a piece of 10 μm thick ^{57}Fe foil (sample). For select measurements, we also loaded a neon pressure-transmitting medium (Table 2.1).

2.2 Synchrotron X-ray Diffraction (XRD)

The theory behind synchrotron x-ray diffraction (XRD) experiments is identical to that of conventional XRD. Therefore, synchrotron XRD probes the interplanar spacing (d) of a crystal structure as a function of x-ray energy (λ) and diffraction angle (2θ):

$$n\lambda = 2d \sin\theta \tag{2.1}$$

(i.e., Bragg's Law). In turn, the sample's unit cell parameters and volume are obtained. The main advantages of synchrotron XRD are that the flux, high-precision x-ray focusing hardware, and very sensitive XRD image plates available at synchrotron radiation facilities allow for the investigation of very small samples, i.e., samples in a DAC.

The basic setup for a synchrotron XRD beamline—such as Sector 12.2.2 at the Advanced Light Source at Lawrence Berkeley Laboratory—is similar to the in-line portion of the schematic for Sector 3-ID-B at the APS (Figure 2.4). The principal hardware component for synchrotron XRD at both sector 12.2.2 and 3-ID-B is the MAR3450 image plate, which is a very sensitive detector that allows for high-statistical quality with low-energy XRD. Sector 12.2.2 is equipped with a Si(111) monochromator, which has an energy range of 6 to 40 keV, and a sample-detector distance of ~200 mm. For our experiments in the panoramic DAC, we used E = 30 keV (λ = 0.4133 Å), and determined the sample-detector distance with high accuracy using a LaB_6 standard. Together with our x-ray transparent cBN seat in the downstream position and angular opening in the DAC of 90º, we have access to a maximum 2θ of ~40º ($d \geq 0.6$ Å) (Figure 2.5).

Sector 3-ID-B is optimized for NRIXS experiments, but is also equipped for in-line XRD (Figures 2.4 and 2.5). The MAR3450 image plate is positioned between the sample stage and the forward scattering detector (see Section 2.3.2), and can be moved in and out

(a)

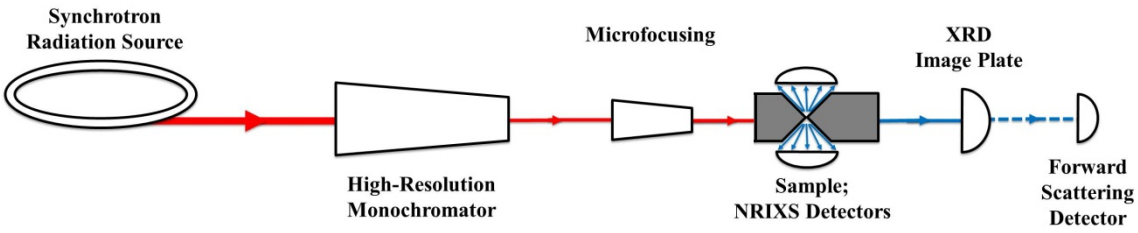

(b)

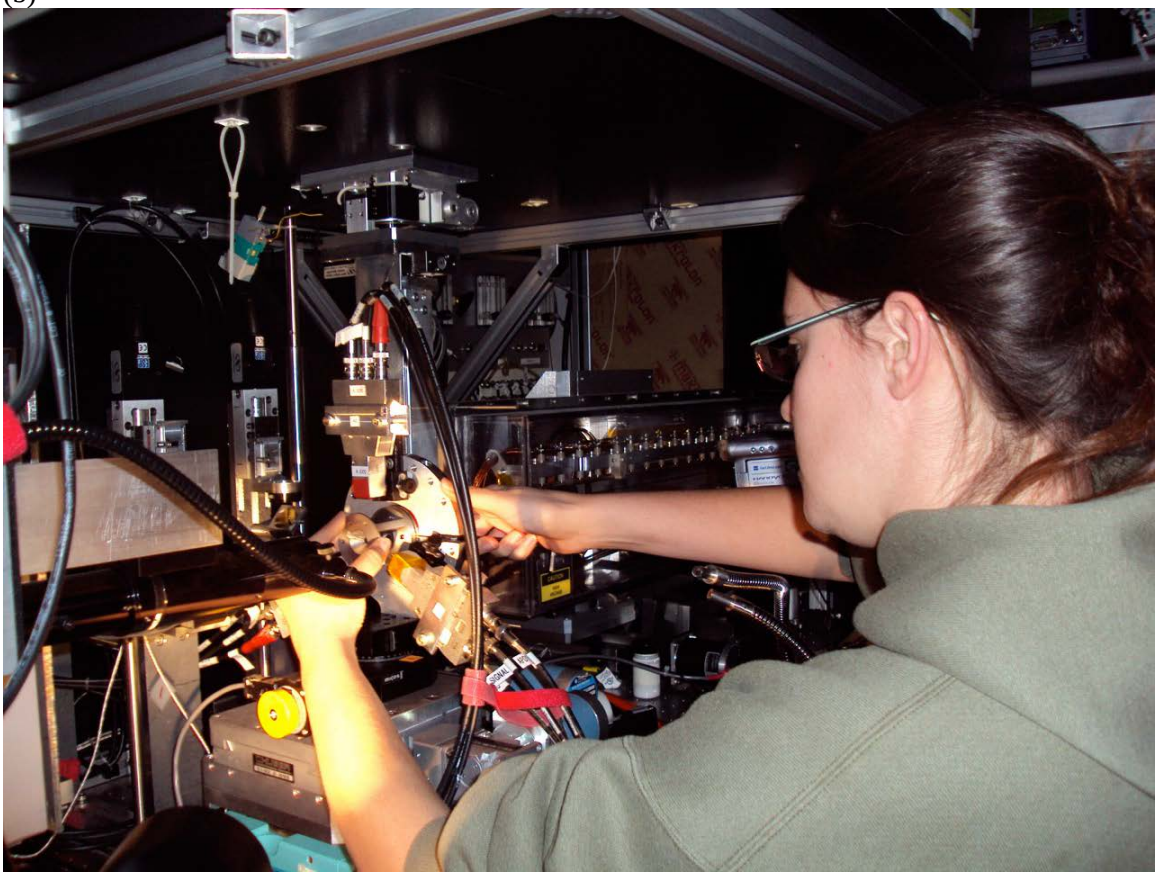

Figure 2.4. Sector 3-ID-B at the Advanced Photon Source. (a) This schematic shows the individual components (labeled in the figure) that are described in Section 3.2.2. (b) A picture taken inside the experimental hutch, with the upstream direction on the right-hand side of the image (i.e., the orientation is the opposite that presented in Figure 2.4a). The panoramic DAC is mounted in the x-ray beam, with three APDs positioned radially around and close to the sample. The XRD image plate is visible in the bottom left corner; it is a MAR3450, which can be moved in and out of the beam to measure XRD before and after NRIXS data collection. The forward-scattering detector is mounted behind where the MAR3450 image plate is positioned in the picture (i.e., off the image to the left); it measures the energy resolution for each NRIXS experiment.

of the x-ray path to allow for *in situ* XRD before and after an NRIXS experiment. The incident energy for this *in situ* XRD is dictated by the NRIXS technique, which requires an incident x-ray energy equal to that of the nuclear resonant energy of ^{57}Fe (E = 14.4125 keV, λ = 0.86025 Å). The sample-detector distance is ~318 mm, as determined during each experimental run from the calibration procedure using a CeO_2 standard. This suggests a maximum 2θ of 28.5º ($d \geq 1.75$ Å), which would corresponds to the maximum pressure at which the (101) diffraction peak for ε-Fe is accessible of ~100 GPa. However, by positioning the MAR3450 image plate at a horizontal offset of 35mm from a centered alignment with the x-ray beam, we were able to increase the maximum accessible 2θ to 33º ($d \geq 1.51$ Å). This new 2θ corresponds to a pressure from the (101) diffraction peak of ε-Fe that is well beyond that of the center of the Earth.

In summary, the majority of the XRD data presented in this thesis are from synchrotron XRD that was collected in-line at Sector 3-ID-B. The energy of the incident x-rays was fixed by the NRIXS experiments (E = 14.4125 keV λ = 0.86025 Å), and the sample-detector distance was calibrated at the beginning of each experimental cycle with a 60-second XRD exposure of a CeO_2 standard. Before and after each NRIXS dataset, a lead plate was inserted directly upstream of the sample stage to reduce detected scattering from objects in the experimental hutch, while a small hole allowed the incident x-ray beam to pass through to the sample. A 5 to 10 minute XRD exposure was measured at the sample position that was probed with NRIXS (Table 2.1). XRD image plate data were analyzed with the Fit2D software (*Hammersley et al.*, 1996), and the Fityk software (*Wojdyr*, 2010) was used to determine the *a* and *c* lattice parameters at each compression point by fitting Gaussians to the observed (100), (002), and (101) diffraction peaks. Evaluation of the

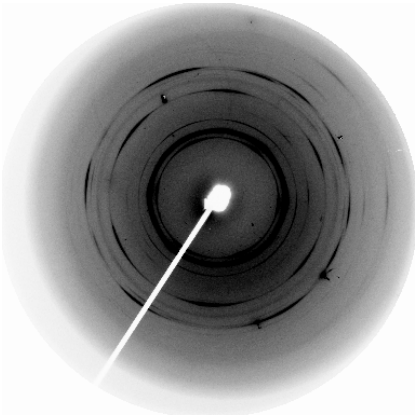

Figure 2.5. Example MAR3450 x-ray diffraction (XRD) image. Black concentric rings are Bragg reflections (i.e., the satisfaction of Equation (2.1)), with the conical angle between the center of the image, the sample, and each ring defining 2θ; the bright feature is the beam stop, which protects the MAR3450 image plate from the direct x-ray beam. This XRD measurement was collected for P9 at the ALS with E = 30 keV (λ = 0.4133 Å).

elastic and vibrational thermodynamic parameters for ε-Fe relies on these *in situ* measured volumes. To present our results on a common scale and for discussion, we convert our volumes to pressures using the Vinet EOS (*Dewaele et al.*, 2006) (Tables 2.1 and 2.2).

Propagating uncertainties in a and c obtained from our XRD data analysis, all compression points have volume errors less than 0.3% and corresponding pressure uncertainties less than 2 GPa (Table 2.2). In order to determine total pressure errors, uncertainties for the EOS parameters determined by *Dewaele et al.* (2006) must be also considered (Table 2.1). However, there is an inherent tradeoff between K_{T0} and K_{T0}' when fitting isothermal XRD data, and *Dewaele et al.* (2006) do not provide information about the correlation of their reported uncertainties. Therefore, we refit their published pressure–volume data with the EOSfit software (*Angel*, 2000) in order to obtain the variances and covariances for K_{T0} and K_{T0}' (Figure 2.6), using the EOS parameters reported by *Dewaele et al.* (2006) and fixing V_0. We note that the EOS parameters we obtain from our fit—$K_{T0} \approx 160.6$ GPa and $K_{T0}' \approx 5.53$—differ slightly from those reported by *Dewaele et al.* (2006), but agree within uncertainty. Finally, combining errors from V_0 (Table 2.1) and our measured volumes with our calculated correlated errors for K_{T0} and K_{T0}', we obtain total pressure uncertainties between 2 and 5 GPa over our experimental compression range.

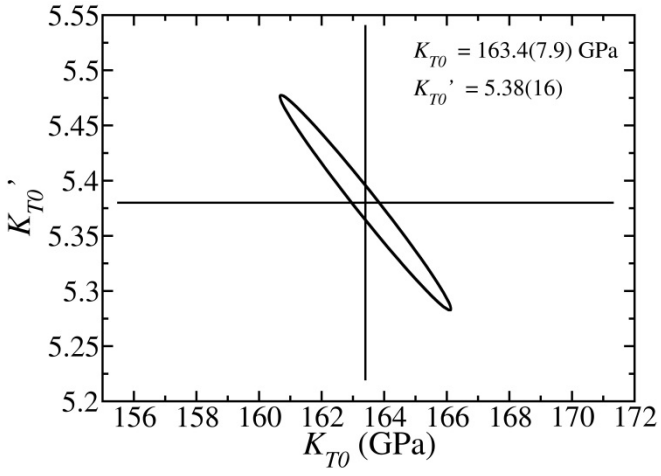

Figure 2.6. Correlation of reported EOS parameter uncertainties. The 1σ error ellipse was calculated as described in Section 2.2, and is centered on the EOS parameters reported by *Dewaele et al.* (2006). We note that the error ellipse was calculated with V_0 fixed to the value given in the caption of Table 2.1.

For our five largest compression points, we observed some texturing in the form of a loss of intensity in the (002) diffraction peak, likely due to nonhydrostatic conditions at extreme pressures. To investigate the sensitivity of our results to possible effects from texturing, we reevaluated the volumes of our five largest compression points with the ratio c/a assigned to be that reported by *Dewaele et al.* (2006), who measured XRD on ε-Fe to over 200 GPa with He and Ne as pressure-transmitting media. With the exception of our measurement at 5.00 ± 0.02 cm^3/mol (P = 106 ± 3 GPa), all resulting volumes and corresponding pressures were within the errors of our original analysis, indicating only a weak effect from texturing. Finally, XRD spectra were collected for P9 at sector 12.2.2 of the ALS, approximately 3 months after the corresponding NRIXS measurement at the APS (Figure 2.5). The energy of the incident x-rays was set to E = 30 keV (λ = 0.4133 Å), and the sample-detector distance was calibrated at the beginning the experimental run with a 60-second XRD exposure of a LaB_6 standard. Observed (100), (002), (101), (102), (110), and(103) diffraction peaks revealed unit cell parameters a = 2.263 Å and c = 3.598 Å, which differ slightly from those measured *in situ* 3 months earlier at Sector 3-ID-B (Table 2.1). However, we note that these unit cell parameters correspond to a molar volume per

Table 2.1. Parameters from a reported EOS and our XRD data collection for ε-Fe.

Index	**Exposure Time (sec), Before/After**[b]	***a*** **(Å)**[c]	***c*** **(Å)**[c]	***V*** **(cm^3/mol)**[c]	***ρ*** **(g/cm^3)**[c]	***K$_T$*** **(GPa)**[d]	***K$_T$′*** [d]
P1[a]	300 / 300	2.424(2)	3.866(2)	5.92(2)	9.61(3)	309	4.47
P2[a]	300 / --	2.404(1)	3.854(1)	5.81(1)	9.80(1)	337	4.37
P3[a]	300 / 300	2.373(2)	3.784(2)	5.56(1)	10.25(1)	408	4.17
P4[a]	300 / 300	2.344(1)	3.739(1)	5.36(1)	10.63(1)	473	4.03
P5	300 / 300	2.335(1)	3.709(1)	5.27(2)	10.80(2)	503	3.97
P6	480 / 480	2.314(1)	3.686(1)	5.15(2)	11.06(2)	555	3.89
P7	480 / 480	2.296(1)	3.639(1)	5.00(2)*	11.38(5)	619	3.80
P8	-- / 300	2.269(1)	3.643(1)	4.89(2)*	11.64(2)	674	3.73
P9	300 / 300	2.262(1)	3.605(1)	4.81(2)*	11.84(2)	718	3.68
P10	600 / 600	2.244(1)	3.577(2)	4.70(2)*	12.13(3)	783	3.62
P11	600 / 600	2.225(1)	3.547(2)	4.58(2)*	12.43(3)	856	3.55

[a]For these measurements, neon was loaded as the pressure transmitting medium. For all other compression points, the sample was fully embedded in the boron epoxy insert, which served as the pressure transmitting medium.

[b]Exposure time of the MAR3450 image plate, for *in situ* XRD measured before and after NRIXS scans at the same sample position. XRD was not collected after our NRIXS scans at P2 because the beam was lost at ~2 am on the final day of our experiment run, and it did not return before the scheduled machine intervention that morning. In addition, no XRD was collected before our NRIXS scans at P8 due to a software problem in the middle of the night that was not solved until the following morning.

[c]Hexagonal close-packed unit cell parameters (*a* and *c*) were determined from measured diffraction peaks corresponding to (100), (002), and (101) crystallographic planes. Reported values are the average of the unit cell parameters measured before and after our NRIXS scans at the same sample position. The molar volume per atom (*V*) was calculated from the measured *a* and *c* values and the definition of a hexagonal close-packed unit cell; density (ρ) was determined from *V* and *m* = 56.95 g/mol for 95% isotopically enriched ^{57}Fe. Values in parentheses give uncertainties for the last significant digit reported.

[d]The isothermal bulk modulus (K_T) and its pressure derivative (K_T') at each compression point were determined from the Vinet EOS parameters for ε-Fe reported by *Dewaele et al.* (2006): $V_0 = 6.75 \pm 0.03$ cm^3/mol, $K_{T0} = 163.4 \pm 7.9$ GPa, and $K_{T0}' = 5.38 \pm 0.16$.

*Texturing was observed at these compression points in the form of a loss of intensity in the (002) diffraction peak.

atom of 4.81 cm^3/mol and a pressure of 133 GPa, which is consistent with the values measured at the APS.

2.3 Nuclear Resonant Inelastic X-ray Scattering (NRIXS)

Nuclear resonant inelastic x-ray scattering (NRIXS) is a fairly recent experimental technique that probes the lattice vibrations (phonons) of select resonant isotopes and, in turn, their phonon density of states. The timing of the earliest NRIXS experiments coincided with the 3rd-generation synchrotrons coming online, as a result of their very high brilliance ($\propto$ flux of a focused beam) compared to earlier synchrotrons. In addition to a very brilliant x-ray source, NRIXS relies on advanced instrumentation and well-defined resonances (which are based on the interaction between protons and neutrons in atomic nuclei) to observe the excitation of nuclear resonant isotopes. One of the most important features of NRIXS is that it is an isotope-selective technique, which means the signal originates only from resonant nuclei and, in turn, the measured background is extremely low. This quality is especially important for experiments at extreme conditions (e.g., high-pressure), where counting rates can be restricted by complicated sample environments.

Currently, the NRIXS technique is available at Sector 3 and the High Pressure Collaboratorive Access Team (HP-CAT, Sector 16) beamlines of the APS; BL11XU and BL35XU at the Super Photon Ring 8-GeV (SPring-8) in Hyogo, Japan; ID18 and ID22N at the European Synchrotron Radiation Facility (ESRF) in Grenoble, France; and at P01 at PETRA–III in Hamburg, Germany. All NRIXS data presented here were collected at Sector 3-ID-B of the APS.

2.3.1 NRIXS Theory

Nuclear resonance and nuclear resonant scattering techniques have previously been

described in great detail (*Gerdau et al.*, 1985; *Ruffer et al.*, 1990; *Seto et al.*, 1995; *Sturhahn et al.*, 1995; *Sturhahn*, 2004), so we provide here only a brief overview. The term "nuclear resonance" refers to the resonant excitation of select nuclei, which can occur via radioactive decay of a parent nucleus, collision with an energetic particle, or absorption of a photon. When the nucleus relaxes to its lower-energy ground state, a γ-ray is emitted with equal or lower energy, depending on the amount of recoil that results from absorption of the photon (required by conservation of momentum). If the recoil energy (E_R) is negligible—which occurs when the lattice in which the absorber is embedded recoils as a single unit—then the emitted photon retains the energy required to excite another nucleus, resulting in resonant excitation. This phenomenon is known as the Mössbauer effect, and is the basic idea behind Mössbauer spectroscopy.

NRIXS is based on the same governing principle, but involves the simultaneous excitation of nuclear resonance and change of quantum state. In Figure 2.7, we provide a schematic representation of the nuclear energy level(s) of ^{57}Fe, and the corresponding

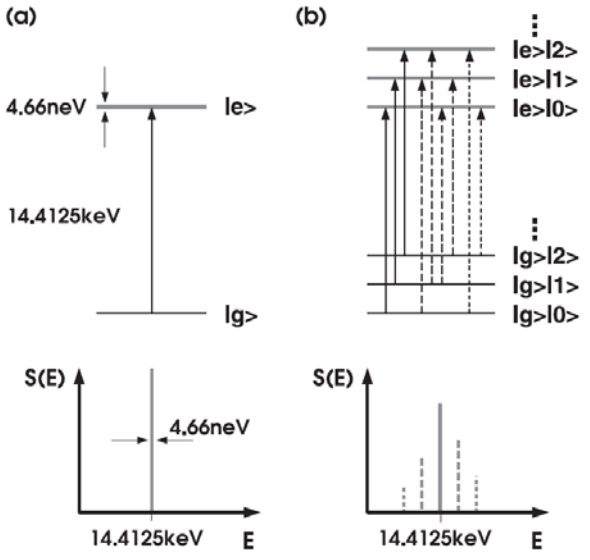

Figure 2.7. Schematic of NRIXS Theory. (a) The top-left schematic gives a nuclear energy level diagram for a fixed ^{57}Fe nucleus, which demonstrates that incident x-rays whose energy is equal to 14.4125 keV induce a transition of the ^{57}Fe nucleus from the ground state ($|g\rangle$) to an excited state ($|e\rangle$); in turn, a sharp peak is produced in the excitation probability density, $S(E)$, given in the bottom left. (b) Schematics on the right show the same quantities, but for ^{57}Fe nuclei embedded in a crystal lattice. The new energy levels reflect lattice vibrations (phonons), and the creation or annihilation of one (dashed lines) and multiple (dotted lines) phonons depicted in the energy level diagram are present as sidebands in $S(E)$. Figure taken from *Sturhahn* (2004).

excitation probability density (i.e., the number of times resonance is achieved at a given energy), which is the quantity measured by NRIXS (*Sturhahn*, 2004). The pair of plots on the left-hand side show a single transition and elastic peak that correspond to the resonant excitation of a fixed nucleus, i.e., a nucleus that cannot recoil ($E_R = 0$). Plots on the right-hand side show similar excitations for ^{57}Fe nuclei bound in a crystal lattice, and one can see that multiple transitions (and corresponding peaks) are now present.

In the plot presented in the bottom-right corner of Figure 2.7, the most prominent peak at the center of the spectrum is still the elastic peak ($E = 0$). This peak represents recoilless absorption of the lattice during absorption of a photon whose energy equals that of the nuclear transition energy. In turn, the emitted photon has the same energy, and resonant excitation of the nuclei can be achieved. This purely elastic (i.e., recoilless) process occurs over a timescale dictated by the lifetime of the nuclear resonance (which is inversely proportional to the energy width of 4.66 neV), and ultimately results in the delayed emission of a photon.

For incident radiation energies on the order of millielectronvolts (meV) larger and smaller than the nuclear transition energy (i.e., slight “off-resonance”), there are additional peaks that represent similar resonant nuclear excitations that were achieved by the creation or annihilation of quantized lattice vibrations (phonons). These peaks are often referred to as Stokes and anti-Stokes peaks, respectively, because of their conceptual similarity to those measured with optical spectroscopy techniques. The anti-Stokes peak corresponds to “phonon-annihilation” because the energy of the incident photon is smaller than the nuclear transition energy, so the resonance signal must originate from the simultaneous absorption of the incident radiation and preexisting energy in the crystal, i.e., a phonon. Similarly, the

Stokes peak corresponds to the number of times resonance was achieved when the excess energy from the incident photon was successfully transferred to the lattice in the form of a new phonon. Finally, a similar pair of lower-intensity peaks at slightly greater energy differences (i.e., farther off-resonance) corresponds to the simultaneous creation (or annihilation) of multiple phonons. The same general features described above can also be seen in Figures 2.8 and 2.9.

There are a few important instrumentation developments that make the elegant features of the previously described NRIXS experiment possible, the first being the extreme brilliance of 3rd-generation synchrotrons like the APS, SPring-8, and ESRF. In addition, the development of efficient and tunable monochromators with very high-energy-resolution (ΔE~1 meV) near the nuclear transition energy (e.g., 14.4125 keV for ^{57}Fe) was essential for investigating the relevant vibrational information, i.e., nuclear resonances that occur at energies on the order of meV away from of the nuclear transition energy (*Toellner*, 2000). Finally, the development of avalanche photodiode (APD) detectors with a very large dynamic range and fast time resolution (nanosecond; ns) was necessary to cleanly distinguish the nuclear resonant scattering signal (which is delayed by the lifetime of nuclear resonance) from the much more efficient (when considering all timescales), nearly instantaneous electronic scattering (*Sturhahn et al.*, 1995).

Another important aspect of NRIXS experiments is the properties of the resonant isotopes themselves. In order for the experiment to be feasible for a given resonant isotope, it must have a large nuclear resonant cross section (i.e., scattering efficiency); a nuclear transition energy that can be produced with high intensity by synchrotron radiation; and a reasonable lifetime for nuclear resonance (i.e., reasonably narrow energy width of

resonance). Fortuitously, ^{57}Fe is one of the most ideal resonant isotopes. It has a nuclear resonant cross section that is 450 times larger than the photoelectric cross section at that energy. In addition, its nuclear transition energy (14.4125 keV) falls at an optimal level that allows for a reasonable flux of incident photons (based on the efficiency of the high-resolution monochromator) and efficiency of other x-ray optics and detectors. Finally, the width of its nuclear resonance is 4.66 neV, which corresponds to a lifetime of nuclear resonance (τ) of 141 ns via the inverse relationship $\tau = \hbar/\Gamma$, where $\hbar$ is the reduced Planck constant (*Sturhahn et al.*, 1995). These values are ideal for timing based on the bunch separation time of the APS (153 ns) and detector efficiency.

2.3.2 Data Collection

A schematic for the basic setup for an NRIXS beamline is given in Figure 2.4a. A brilliant, continuous spectrum of photons is produced by insertion devices at 3rd-generation synchrotron radiation sources, such as the APS. To select out the x-rays with the necessary energy for an NRIXS experiment, the beam first passes over a diamond (111) high-heat-load monochromator, which selects for a narrow band of wavelengths around the nuclear transition energy of ^{57}Fe with a resolution (ΔE) of ~1 eV. Next, the beam passes over a Si multireflection high-resolution monochromator, which selects an x-ray energy of 14.4125 keV with ΔE ~1 meV (*Toellner*, 2000). Finally, the beam is focused onto the sample using Kirkpatrick-Baez mirrors, which produce a focused spot size of ~10 × 10 μm. Delayed scattered photons from nuclear resonances are detected by avalanche photodiode (APD) detectors positioned radially around and close to the sample (Figure 2.4). In addition, the energy resolution is determined via a fourth APD, which is placed in the forward-scattering

direction. When installed (as in Sector 3-ID-B), an XRD image plate can be moved into and out of the beam's path to collect *in situ* XRD, as described in Section 2.2.

The following procedure for collecting an NRIXS dataset is specific to Sector 3-ID-B of the APS, and assumes that the x-ray beam is already optimally aligned and focused. In addition, it assumes the monochromator has been tuned so that the energy of the incident x-rays is near the nuclear resonance energy of ^{57}Fe (14.4125 keV), although small deviations due to temperature drift are fine for the described procedure because the hutch is well-insulated. Finally, it assumes the placement of an APD detector in the forward scattering position, which will measure the energy resolution during the experiment.

The first step is to prepare the panoramic DAC to be mounted on the sample stage. The putty that supported the Be gasket during indentation and sample loading must be removed in order to maximize the counting rates, since leftover putty will absorb scattered photons. Next, it is recommended that a mark be made on the panoramic DAC to note which "window" is orientated in the upward direction, for consistency between measurements. The DAC can then be secured in the sample holder, and the three APD detectors can be positioned as close to the sample as possible, i.e., ~2 cm away because of the DAC geometry (Figure 2.4). At this point, it is important to check whether any signal (i.e., noise) is being detected by the APDs while the x-ray shutter is closed, since this could add significant background noise to the dataset. If there are significant counts on any of the detectors, their mounting should be checked to ensure they are in contact with the DAC and not being torqued. If everything seems correct but the signal remains without any incident x-rays, the detector itself likely needs to be replaced or repaired. Finally, the sample mount can be placed in the path of the x-ray beam, to begin the procedure of locating the sample.

Before the x-ray shutter is opened, one initially locates the sample using a microscope that has been aligned with the x-ray spot in all dimensions. Once the sample is approximately focused in the aligning microscope, a small diamond correction is made to account for the index of refraction of the diamond that is upstream of the sample (1.15 μm in the upstream direction). After recording the approximate position of the sample, one can open the x-ray shutter and check whether any delayed signal is being registered on the APDs. If there is little to no signal, the first step is to tune the monochromators to ensure the energy of the beam is on resonance, i.e., 14.4125 keV. Once the energy of the beam has been optimized, one can scan the position of the sample stage in the horizontal and vertical directions, to align the beam in a very reproducible spot on the sample that has high counting rates; this often corresponds to the center of the sample. The energy of the beam is tuned to fully optimize the energy of the beam and, in turn, the counting rates. Finally, the background that is being measured by the APDs is checked by allowing them to count for 100 seconds at an energy that is 200 meV below the resonance energy. If the number of background counts is too high (> 0.1 Hz), then it is likely that the timing window of the detectors needs to be adjusted because photons are spilling over from the prompt signal.

If *in situ* XRD is being collected, then the image plate must be moved in-line with the x-ray beam and the lead plate inserted upstream of the DAC at this time. After securing the hutch, the MAR3450 image plate is erased (of any previously collected data), and an exposure is collected by opening the x-ray shutter for a fixed amount of time (5 to 10 minutes in our case). After closing the shutter, the image from the MAR3450 image plate is recorded (read out), and the XRD data can be viewed and initially processed with the Fit2d software to determine the sample pressure.

To begin an NRIXS measurement, the parameters of a single scan are assigned, including the energy range around the nuclear resonance energy to be scanned; the number of points to be collected over that energy range (i.e., the energy step size); and the amount of time for data collection at each energy step. The energy can drift over time due to temperature changes, so a scan time of ~1 hour is ideal. This allows for the optimization of the energy between scans to ensure a high-quality dataset. Finally, individual scans can be summed together after as many scans as are necessary to produce the desired number of counts have been collected, e.g., in the Stokes peak.

The NRIXS data presented in this thesis are based on experiments that were performed at beamline 3-ID-B of the APS in October 2009, August 2010, and February 2011. For each experimental run, the storage ring was operated in top-up mode with 24 bunches that were separated by 153 ns. Three APD detectors were positioned radially around and close to the sample to collect the incoherent inelastic scattered photons. A fourth APD was positioned downstream in the forward scattering direction and independently measured an average ΔE ~ 1.2 meV at FWHM (*Toellner*, 2000). For each NRIXS scan at most compression points, the high-resolution monochromator was tuned from –65 to +85 meV around the nuclear resonance energy of ^{57}Fe (14.4125 keV). For our two largest compression points, this range was extended to –75 to +90 meV, to ensure we were measuring all of the vibrational information. Between 8 and 21 NRIXS scans were collected for each compression point, with the exception of our measurement at 5.81 ± 0.01 cm^3/mol (P = 36 ± 2 GPa), for which only four scans were collected (Table 2.2). The raw NRIXS data from each of our 11 compression points are plotted together in Figures 2.8 and 2.9.

Table 2.2. Pressures and experimental parameters for our NRIXS data collection.

Index	V (cm^3/mol)	P (GPa)[e]	Energy Range (meV)[f]	Stokes Peak (counts/sec)[g]	Number of Scans[g]
P1[a]	5.92(2)	30(2)	−65 to +85	290/58	12
P2[b]	5.81(1)	36(2)	−65 to +85	70/18	4
P3[a]	5.56(1)	53(2)	−65 to +85	100/36	8
P4[a]	5.36(1)	69(3)	−65 to +85	130/38	8
P5[c]	5.27(2)	77(3)	−65 to +85	280/50	10
P6[c]	5.15(2)	90(3)	−65 to +85	310/88	18
P7[c]	5.00(2)*	106(3)	−70 to +85	290/66	14
P8[c]	4.89(2)*	121(3)	−65 to +85	210/85	21
P9[c]	4.81(2)*	133(4)	−65 to +85	130/38	8
P10[d]	4.70(2)*	151(5)	−75 to +90	130/65	13
P11[d]	4.58(2)*	171(5)	−75 to +90	70/40	8

[a]NRIXS and *in situ* XRD measurements were performed using a single preparation of DAC11, in order of increasing compression (P1, P3, P4).

[b]NRIXS and *in situ* XRD measurements were performed at P2 during decompression of DAC12. (No other NRIXS experiments were performed with this DAC preparation.) We note that only 4 NRIXS scans were collected at P2 because the beam was lost at ~2am on the final day of our experiment run, and it did not return before the scheduled machine intervention.

[c]NRIXS and *in situ* XRD measurements were performed using a single (new) preparation of DAC11, in order of increasing compression (P5, P6, P7, P8, P9).

[d]NRIXS and *in situ* XRD measurements were performed using a single (new) preparation of DAC11, in order of increasing compression (P10, P11). We note that only 70 counts were collected in the Stokes peak for P11 because the diamonds failed during the 9th scan.

[e]Measured volumes were converted to pressures (P) using the Vinet EOS for ε-Fe reported by *Dewaele et al.* (2006) (Table 2.1). Reported uncertainties in P reflect measured uncertainties in V and reported uncertainties for the Vinet EOS parameters, with a correlation between K_{T0} and K_{T0}' determined from our fit of the pressure–volume data reported by *Dewaele et al.* (2006). See Section 2.2 and Figure 2.6 for more details.

[f]The energy range over which NRIXS data was collected, relative the nuclear transition energy of ^{57}Fe (14. 4125 keV). Larger energy regions were necessary at P10 and P11 to ensure that we were measuring all of the vibrational information.

[g]The numerator of the ratio gives the absolute number of counts at the height of the first Stokes peak. The denominator provides the total seconds counted at each energy step, which reflects the number of scans and the data collection time at each energy step.

2.3.3 Data Analysis

The data analysis procedure presented here is based on the PHOENIX software (*Sturhahn*, 2000), which greatly simplifies and streamlines the necessary data analysis. The first step is to sum together all of the scans collected at a given compression point using the "padd" command, which also converts the data file measured directly by the APDs into a more commonly readable format. To prepare the input file for the "padd" command ("in_padd"), one must assign values for the operating energy and sample temperature, which are fixed at 14.4125 keV and 300 K, respectively, for our investigations of ^{57}Fe at ambient temperature. In addition, detailed information is needed about the monochromator, scan parameters, and the background, width, and asymmetry of the measured resolution function. The final step for preparing the input file for "padd" is indicating the names of the scans that are to be summed together.

The result of running the "padd" (or "mpadd") command are *.dat (data; Figures 2.8–2.10) and *.res (resolution function) files. The data file provides the flux of delayed k-fluorescence photons emitted during deexcitation of the nucleus, i.e., the sum of data collected by the three APDs positioned radially around the sample, from all relevant scans. Similarly, the resolution file contains the sum of all data collected by the APD in the forward scattering position. An example of these two curves measured at 90 GPa is given in Figure 2.10, with the data file plotted in black and the resolution file plotted in red. In total, 18 scans were collected over an energy range of −65 to +85 meV around the nuclear transition energy; 1 scan counted for 3 seconds at each energy step, and 17 scans counted for 5 seconds, resulting in a total of 88 seconds at each energy step. The number of counts per second is a function of both sample thickness and how well optimized the

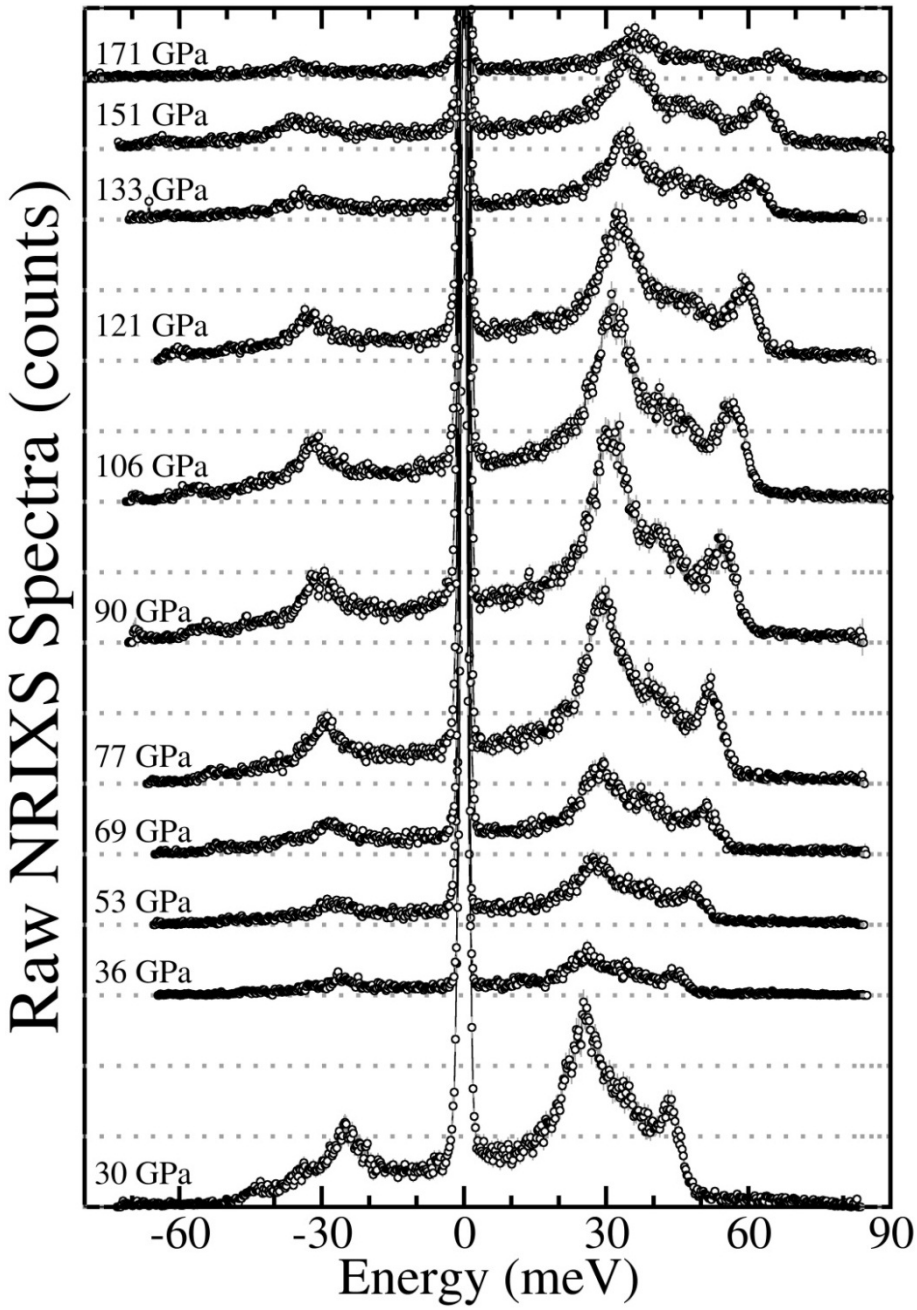

Figure 2.8. Our raw NRIXS spectra for ε-Fe. Black circles represent the number of times resonance was achieved at a given energy around the nuclear transition energy of ^{57}Fe (14.4125 keV, which is plotted as 0-energy). The energy-step size was 0.25 meV. The elastic peaks at $E = 0$ extend vertically beyond the edge of the plot; peaks present at $E > 0$ correspond to the excitation of lattice phonons, while peaks present at $E < 0$ correspond to the annihilation of pre-existing lattice phonons. Gray dotted lines are plotted horizontally at increments of 100 counts, to allow for estimation of the height of the Stokes (Table 2.3) and anti-Stokes peaks for a given spectrum. We note that the raw data presented here is not normalized and, thus, absolute peak heights are largely influenced by data collection times.

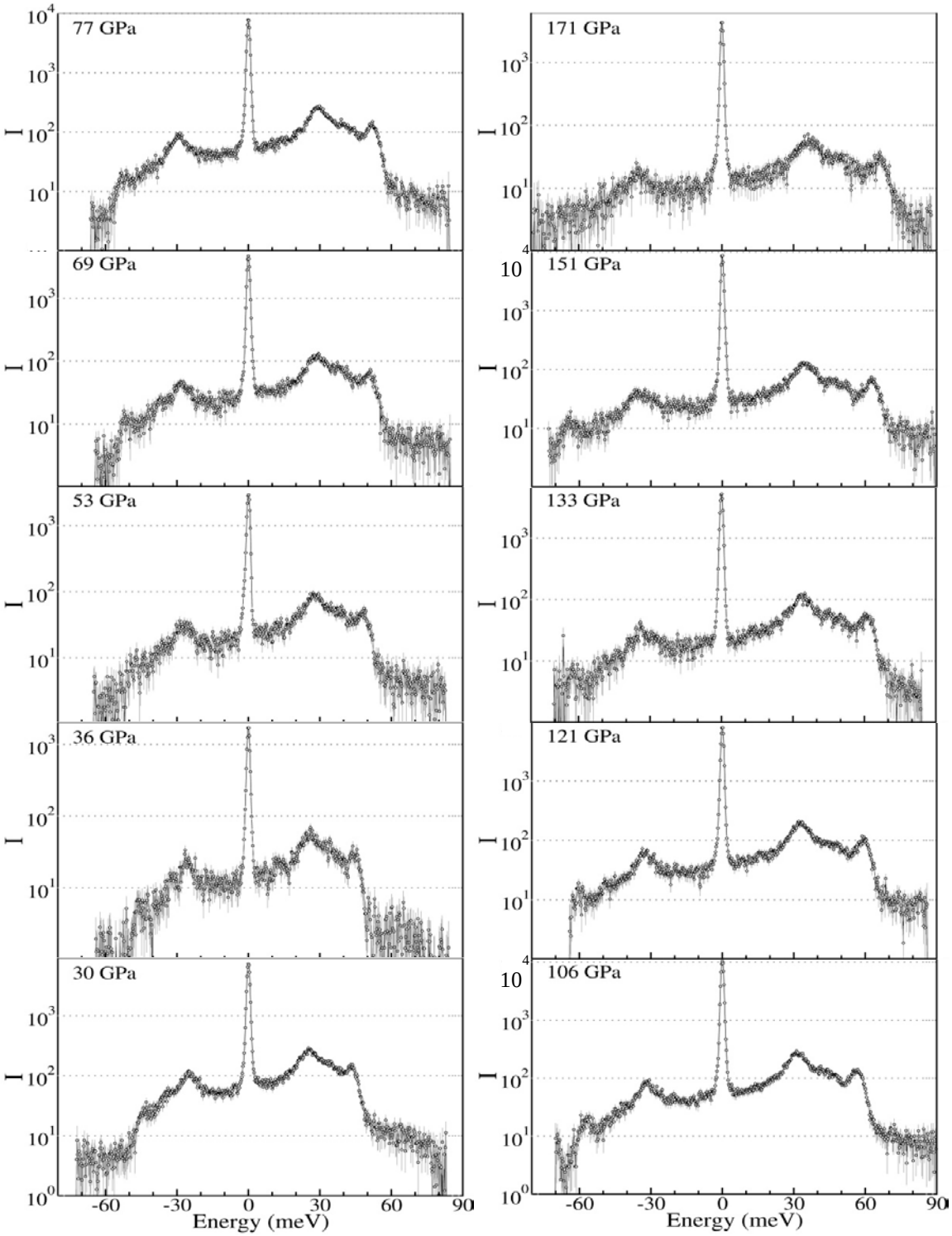

Figure 2.9. Our raw NRIXS spectra for ε-Fe, normalized. Black circles represent the same data given in Figure 2.8, but now plotted separately and with a logarithmic vertical scale for intensity (*I*), in order to facilitate viewing data at each compression point. We note that the raw data measured at 90 GPa is not included in this figure because it is plotted separately in Figure 2.10.

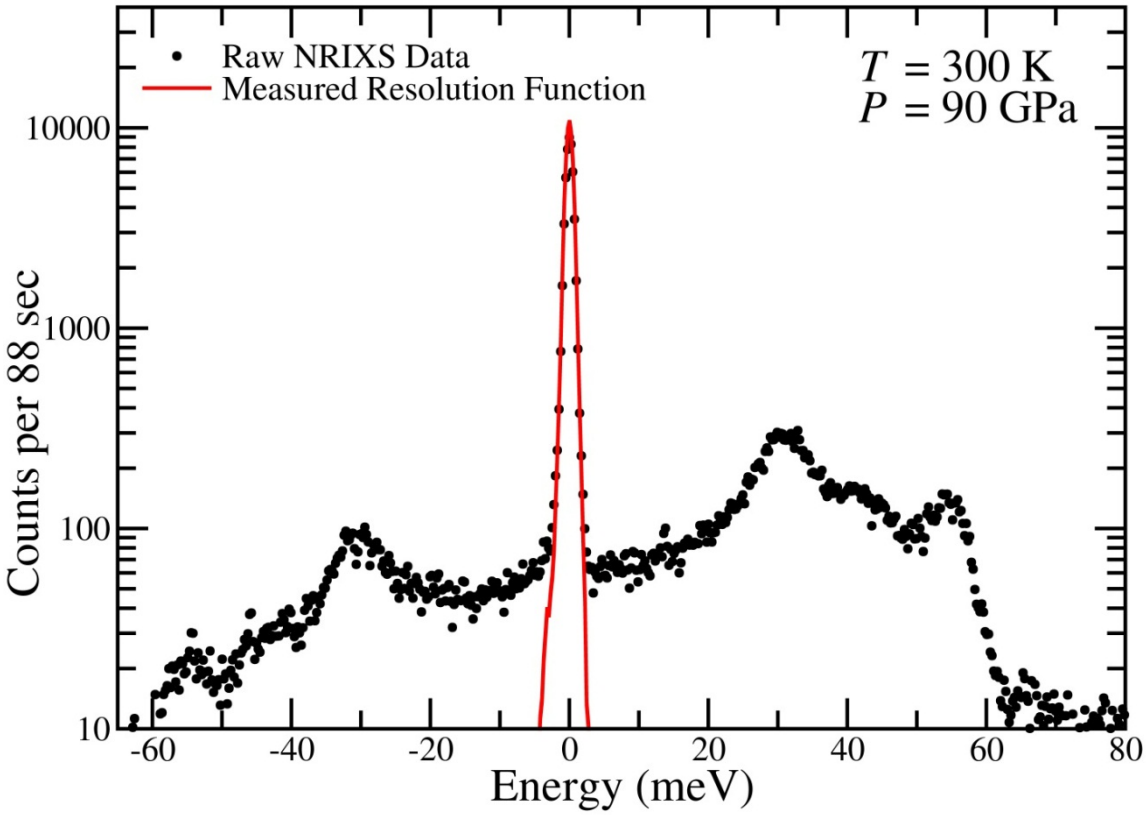

Figure 2.10. Example raw NRIXS spectrum with detail. The raw NRIXS spectrum measured at V = 5.15 ± 0.02 cm^3/mol (P = 90 ± 3 GPa) is given, highlighting the important features: raw data in black (i.e., the flux of delayed K-fluorescence photons emitted during de-excitation of the nucleus; Figures 2.8 and 2.9); resolution function in red (measured with the forward scattering detector); energy range of scans (-65 to + 80 meV); counts per 88 sec (related to the number of scans and the degree of optimization of the monochromator); an intense elastic peak (demonstrating the large recoilless fraction of ε-Fe); and the pressure determined from *in situ* XRD and an established EOS (*Dewaele et al.*, 2006).

monochromator is. The strong intensity of the central elastic peak demonstrates ε-Fe's large recoilless fraction (Section 2.3.1).

Once the individual NRIXS scans for a given compression point have been summed together, the resolution function file must be prepared so that it can be read and analyzed by the PHOENIX software. First, one subtracts any overall background, determined by fitting a line to the entire dataset. Next, the width of the resolution function

is determined by visually investigating where its intensity decreases to the level of the background noise (typically around $E \sim \pm 5$ meV for our experiments); any data beyond this width is then removed. In the case of a poorly resolved resolution function, any "tails" that extend to higher energies should be kept in the resolution function file; in turn, this introduces additional uncertainties for analyses involving low-energy vibrational information (Section 5.5). We note that the procedure of preparing the resolution function file is not necessary if one is using the newest version of the software (PHOENIX 2.1.0), which automatically prepares the resolution function file during the command that sums together the measured NRIXS spectra.

The NRIXS data and resolution function files are now ready (e.g., Figure 2.10) to be read and analyzed. Basic information that must be provided in the input file for PHOENIX ("in_phox") includes the nuclear transition energy and recoil energy of the resonant isotope (14.4125 keV and E_R = 1.956 meV for ^{57}Fe, respectively), and the sample temperature. In addition, tunable parameters that influence the quality of the data analysis include the inelastic and overall data background, and the fit range and asymmetry of the elastic peak. These parameters must be adjusted during analysis to produce the optimal normalization of the data and avoid negativity of the resulting phonon density of states (DOS), i.e., in order to obtain accurate vibrational thermodynamic parameters.

The first important output of the PHOENIX software is the pure phonon excitation spectrum, $I'(E)$, which is the spectrum that is produced once the PHOENIX software properly fits and removes the elastic contribution (peak) from the data file. In turn, $I'(E)$ is related to $S(E)$—the excitation probability density, or the probability for absorption per unit of energy—via a normalization procedure which is based on the general property that the

first moment of $S(E)$ is equal to E_R. To decompose the measured $S(E)$ into one- and multi-phonon (n-phonon) contributions, the PHOENIX software performs a forward data inversion (i.e., the Fourier-log technique), as described by *Sturhahn* (2000). From the total $S(E)$, the Lamb-Mössbauer factor, kinetic energy, and mean force constant can be obtained from the 0th-, 1st-, 2nd-, and 3rd-order moments, i.e., $S_n = \int E^n S(E)\,dE$ for n = 0, 1, 2, and 3. Details of this procedure have been presented by *Lipkin* (1995), *Sturhahn and Chumakov* (1999), and *Sturhahn* (2004).

Next, to determine the phonon density of states (DOS), $D(E,V)$, the PHOENIX software applies the quasi-harmonic lattice model to $S(E)$. In general, the quasi-harmonic lattice model assumes individual lattice vibrations (phonons) do not interact, so the system is approximated as a set of independent harmonic oscillators. It assumes the interatomic potential around equilibrium atomic positions has a quadratic dependence on atomic displacement, resulting in phonons with infinite lifetimes and well-defined atomic motions. In turn, the quasi-harmonic model implies the temperature dependence of phonon frequencies and, in turn, the phonon DOS, arises only from thermal expansion (i.e., a change in volume). Such an assumption is thought to be reasonable for ambient temperature conditions, such as those relevant for the experiments presented here. However, we note that the accuracy of the quasi-harmonic approximation becomes questionable at high temperatures, where phonon-phonon and phonon-electron interactions play an increasingly important role.

As previously stated, PHOENIX applies the quasi-harmonic lattice model to $S(E)$ in order to determine the partial and projected phonon DOS, $D(E,V)$:

$$D(E,V) = \frac{E}{E_R} \tanh \frac{\beta E}{2} \left(S_1(E,V) + S_1(-E,V) \right)$$

for $E \geq 0$ (*Sturhahn*, 2004). The phonon DOS determined from NRIXS measurements at each of our 11 compression points are plotted together in Figure 2.11. From the phonon DOS, one obtains a variety of elastic and vibrational thermodynamic parameters. For example, the integrated phonon DOS is directly related to the Lamb-Mössbauer factor and vibrational components of the specific heat capacity, free energy, entropy, internal energy, and kinetic energy, providing a self-consistent check on the parameters that are related to the moments of the raw NRIXS data. Details of how each parameter can be determined from the phonon DOS will be presented in their respective sections.

To demonstrate the high statistical quality of our phonon DOS, we compare our measured uncertainties with those from a previous NRIXS study on ε-Fe over a similar compression range (*Mao et al.*, 2001). Performing the same PHOENIX analysis on both datasets, we find that our data produce errors for parameters determined from the phonon DOS that are ~70% smaller on average, largely due to our long data collection times and the higher-resolution monochromator (ΔE = 2 meV in *Mao et al.* (2001)).

Finally, the "psvl" command in PHOENIX performs a parabolic fit of the low-energy region of the phonon DOS to determine the Debye sound velocity (see Section 4.4). The input file for psvl ("in_psvl") requires knowledge of the sample density, which can either be determined from *in situ* measured volumes (as in our case), or via an equation of state (EOS). The latter calculation can be performed by the "psvl" command, based on the indicated pressure value and EOS parameters. In addition, the user must determine the appropriate energy range over which to perform the fit. The lower bound of this range is

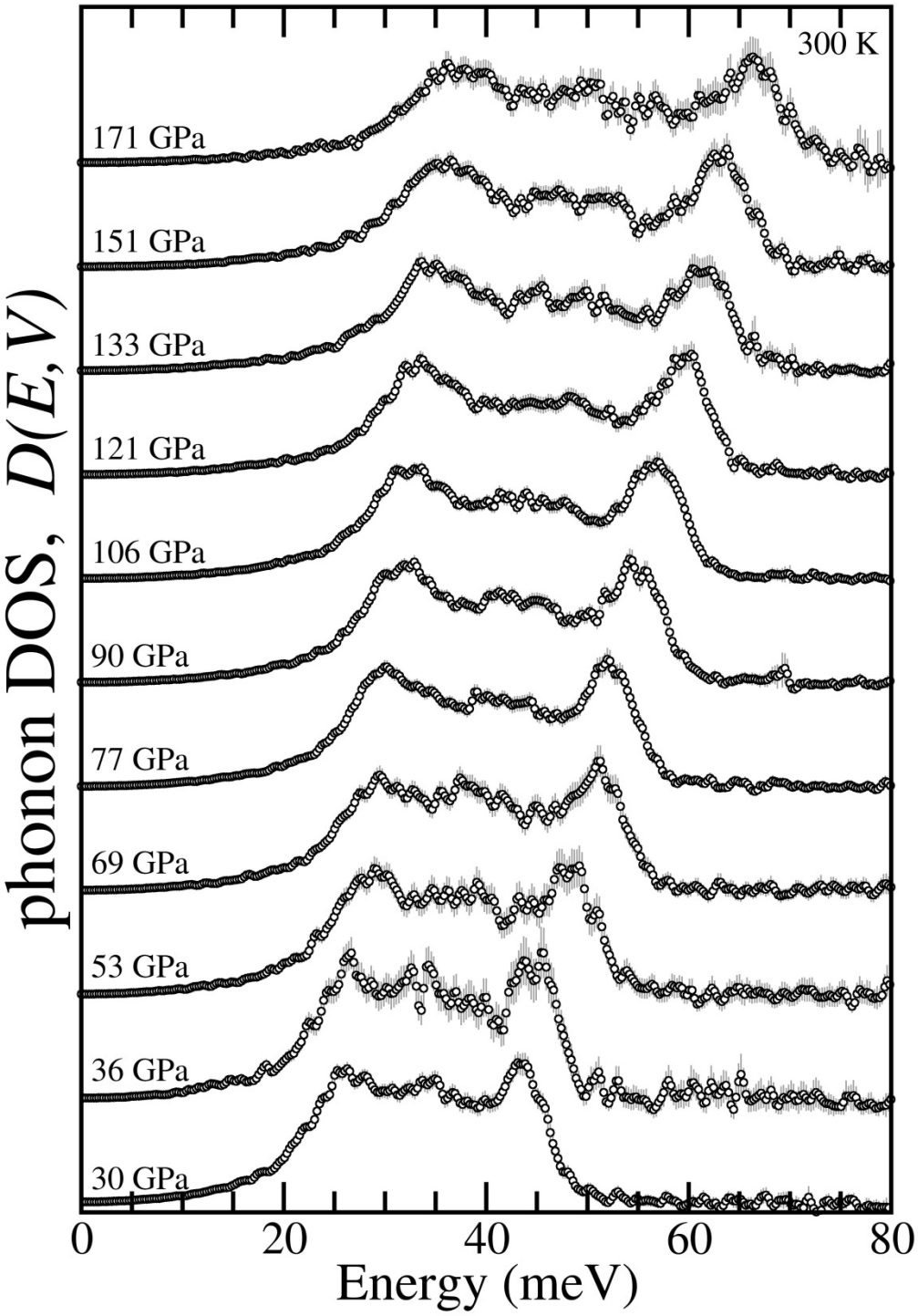

Figure 2.11. Our measured phonon DOS for ε-Fe. Black circles give the measured phonon DOS at an energy step of 0.25 meV, determined by applying the quasi-harmonic model to our raw NRIXS data after removal of the elastic peak (*Sturhahn*, 2000). Uncertainties are plotted as gray vertical lines; the pressure of each phonon DOS is labeled on the figure, and was determined from our *in situ* measured volumes.

dictated by the width of the resolution function (~3.5 meV), which may influence the curvature of the phonon DOS and, in turn, the Debye sound velocity. The upper bound is dictated by the maximum energy at which the Debye model is appropriate, i.e., where the phonon DOS is parabolic, which was below ~20 to 34 meV for our experimental compression range. The end result is that the “psvl” command will provide values for the Debye sound velocity produced by fits over various energy ranges, in addition to the corresponding compressional and shear sound velocities that are based, in part, on the input EOS parameters. We note that the choice of energy range by the user introduces some uncertainty to the output sound velocities; therefore, it is important to investigate the magnitude of this uncertainty as a function of energy range.

Chapter 3

Melting and Thermal Pressure of hcp-Fe[1]

3.1 Introduction

The Earth's core is thought to be composed mainly of iron with some light elements (*McDonough*, 2003). Therefore, an accurate determination of the high-pressure phase diagram of iron is of fundamental importance for studies of the deep Earth. Of particular interest is iron's high-pressure melting behavior (e.g., *Williams et al.*, 1987; *Boehler*, 1993; *Shen et al.*, 1998; *Ahrens et al.*, 2002; *Ma et al.*, 2004; *Nguyen and Holmes*, 2004), because Earth's solid inner core and liquid outer core are in contact at the inner–core boundary. This phase boundary serves as an important constraint on the temperature profile of the core and offers insight into the temperature at the core–mantle boundary, which is a key parameter for geodynamic modeling and for determining what phases are stable in the lowermost mantle.

Existing data suggest that hexagonal close-packed iron (ε-Fe) is the stable phase at core pressures and room temperature (*Alfè et al.*, 2001; *Ma et al.*, 2004; *Dewaele et al.*, 2006; *Tateno et al.*, 2010). However, the high-pressure melting behavior of ε-Fe is not well

[1] Revised over what was previously published as *Murphy et al.* (2011a).

established due to experimental challenges at simultaneous high-pressure and temperature (*PT*) (e.g., see Figure 1 in (*Nguyen and Holmes*, 2004)), which also make it difficult to confirm or reproduce past experimental results.

An alternative to investigating the melting curve of ε-Fe with high-*PT* experiments is to measure its ambient temperature phonon density of states (DOS), which contains vibrational information that is coupled with its melting behavior. In particular, the phonon DOS of ε-Fe is directly related to its mean-square displacement of atoms, which can be used to determine the shape of ε-Fe's high-pressure melting curve. By anchoring this shape with an experimentally determined melting point, one obtains ε-Fe's high-pressure melting behavior from phonon DOS experiments at 300 K. This approach minimizes the potential for chemical reactions in high-*PT* experiments and the need to rely on accurate temperature readings at extreme conditions. We present the shape of ε-Fe's high-pressure melting curve, which we benchmark through existing experimental data on ε-Fe.

An additional geophysical application of ε-Fe's phonon DOS at 300 K is the direct determination of the volume- and temperature-dependent vibrational free energy, which is related to the vibrational component of the thermal pressure. Together with the electronic and anharmonic components, this gives the total thermal pressure (P_{th}), which is an important parameter for determining the density of iron under core conditions. Shock-compression experiments have accessed P_{th} via the thermodynamic Grüneisen parameter and Mie-Grüneisen theory (*Jeanloz*, 1979; *Brown and McQueen*, 1986; *Asimow and Ahrens*, 2010), and many past theoretical calculations have dealt with P_{th} (*Wasserman et al.*, 1996; *Stixrude et al.*, 1997; *Vočadlo et al.*, 2000; *Alfè et al.*, 2001; *Sha and Cohen*, 2010a). Here we present a direct determination of the vibrational component of the thermal

pressure from measurements of ε-Fe's phonon DOS.

We performed nuclear resonant inelastic x-ray scattering (NRIXS) and *in situ* synchrotron x-ray diffraction (XRD) experiments in order to directly probe the volume dependence of ε-Fe's total phonon DOS between pressures of 30 and 151 GPa. Similar NRIXS experiments have previously been performed on ε-Fe up to 153 GPa (*Lübbers et al.*, 2000; *Mao et al.*, 2001; *Giefers et al.*, 2002; *Shen et al.*, 2004; *Lin et al.*, 2005). However, these reports did not attempt analysis of the melting curve shape or the determination of the volume-dependent thermal pressure of ε-Fe. In addition, our long data collection times at pressures over 100 GPa resulted in the highest statistical quality phonon DOS to outer core pressures measured to date, and our *in situ* determination of sample volume with XRD distinguishes this study from previous similar works.

3.2 Experimental

For details of our DAC preparation, experimental procedures, and data analysis, see Chapter 2. The analysis, results, and discussion in this chapter are based on the first 10 compression points of the dataset described in Chapter 2 ($P \leq 151$ GPa), because it was performed before the final compression point ($P = 171 \pm 5$ GPa) was collected in February 2011. We note that results from the analysis presented in this chapter with the addition of our final, largest compression point agree with the original results within uncertainty.

NRIXS data were analyzed with the PHOENIX software, which was used to remove the elastic contribution and apply the quasi-harmonic lattice model (*Sturhahn*, 2000; *Sturhahn and Jackson*, 2007). From the resulting volume-dependent total phonon DOS, $D(E,V)$, we obtained two parameters that are related to ε-Fe's thermal pressure and melting curve shape. The vibrational free energy per ^{57}Fe atom (F_{vib}) is given by

$$F_{vib}(V,T) = \frac{1}{\beta}\int \ln\left(2\sinh\frac{\beta E}{2}\right) D(E,V)\,dE \qquad (3.1)$$

(Table 3.1, Figure 3.1), where $\beta = (k_B T)^{-1}$ is the inverse temperature and k_B is Boltzmann's constant. In addition, the mean-square displacement of ^{57}Fe atoms ($\langle u^2 \rangle$) is given by

$$\left\langle u^2 \right\rangle = \frac{E_R}{3k_0^2}\int \frac{1}{E}\coth\frac{\beta E}{2} D(E,V)\,dE, \qquad (3.2)$$

where E_R is the recoil energy and k_0 is the wavenumber of the resonant photon. For the 14.4125 keV transition of ^{57}Fe, E_R = 1.956 meV and k_0 = 7.306 Å^{-1} (*Sturhahn*, 2004). In Equations (3.1) and (3.2), the phonon DOS has been normalized by $\int D(E)\,dE = 3$.

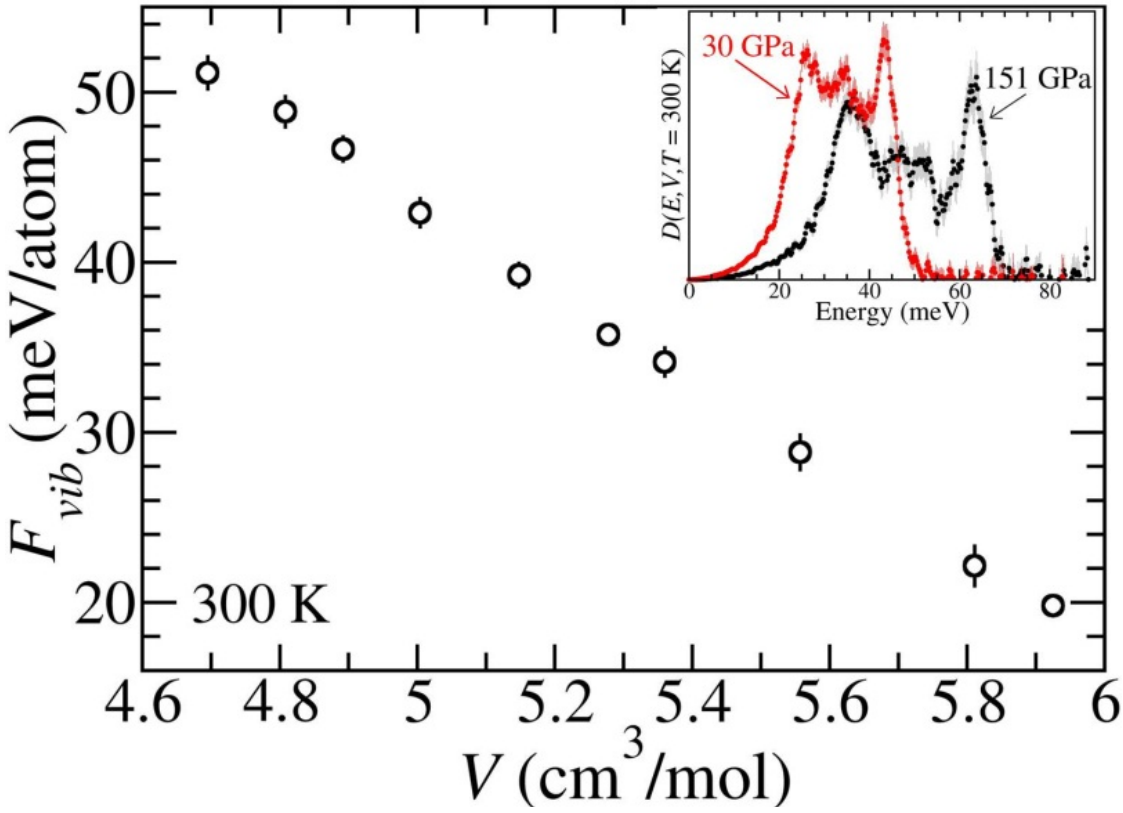

Figure 3.1. Vibrational free energy per ^{57}Fe atom at 300 K. Inset shows the measured total phonon DOS of ε-Fe at 30 GPa (red) and 151 GPa (black) at 300 K.

Table 3.1. Free energy and Lamb-Mössbauer temperature from NRIXS data, and melting temperatures and thermal pressures from analysis.

V (cm^3/mol)[a]	P_V (GPa)[a]	F_{vib} (meV/atom)[b]	T_{LM} (K)[b]	T_M^h (K)[c]	P_{th} (GPa)[d]	T_M (K)[c]
5.92(2)	30(2)	19.8(6)	2140(20)	2470(70)	17(1)	2190
5.81(1)	36(2)	22(1)	2210(40)	2520(80)	18(1)	2250
5.56(1)	53(2)	29(1)	2520(40)	2790(90)	22(1)	2600
5.36(1)	69(3)	34.1(8)	2810(30)	3040(90)	25(1)	2940
5.27(2)	77(3)	35.7(5)	2920(20)	3130(90)	27(1)	3110
5.15(2)	90(3)	39.2(7)	3180(30)	3300(100)	30(1)	3400
5.00(2)	106(3)	42.9(8)	3370(30)	3500(100)	31(1)	3520
4.89(2)	121(3)	46.7(7)	3660(40)	3700(100)	35(2)	3880
4.81(2)	133(4)	48.8(9)	3830(50)	3900(100)	36(2)	3930
4.70(2)	151(5)	51.1(9)	4130(60)	4100(100)	39(2)	4160
4.58(2)[e]	171(5)	55.9(1.4)	4330(90)	4300(100)	40(2)	4240

Note: Values in parentheses denote errors for the last significant digit(s) reported.
[a]Molar volumes per ^{57}Fe atom (V) and pressure (P_V) for each compression point are duplicated from Tables 2.1 and 2.2. A brief explanation of reported uncertainties is given in Section 2.2.
[b]The vibrational free energy (F_{vib}) and Lamb-Mössbauer temperature (T_{LM}) at 300 K were calculated from the measured total phonon DOS (*Sturhahn*, 2000; 2004).
[c]The harmonic melting temperature $\left(T_M^h\right)$ was determined using Equation (3.9) and the *Ma et al.* (2004) anchor melting point; anharmonic melting temperatures (T_M) account for anharmonic effects (Section 3.5; Appendix A).
[d]The total thermal pressure (P_{th}) was taken at T_M and used in Equation (3.10) before extrapolating and plotting T_M (P) in Figure 3.4.
[e]Although our final, largest compression point was not included in the analysis presented in this chapter, we report the corresponding values for reference. We note that the results from the fitting and extrapolation procedures described in Section 3.5 with the addition of our largest compression point agree with the original results within uncertainty.

3.3 Thermal Pressure

The total thermal pressure is additive in its vibrational and electronic components:

$$P_{th} = P_{vib} + P_{el} = -\left(\frac{\partial F_{vib}}{\partial V}\right)_T - \left(\frac{\partial F_{el}}{\partial V}\right)_T . \tag{3.3}$$

Fitting our F_{vib} data (Table 3.1) with a 2nd-order polynomial, we find $F_{vib}(V, 300\ \mathrm{K}) = 220.15 - 43.74V + 1.67V^2$, in units of meV/atom. Then, taking the volumetric derivative of

this relation, we obtain $P_{vib}(V, 300\ \text{K}) = 0.0965(43.74 - 3.35V)$, which gives $P_{vib}(V, 300\ \text{K})$ = 2.31 ± 0.06 and 2.70 ± 0.06 GPa at our smallest (30 GPa) and largest (151 GPa) compression points, respectively. We note that the value outside of the parentheses in our relation for $P_{vib}(V, 300\ \text{K})$ corresponds to a conversion of units, giving P_{vib} in units of GPa.

We can also investigate the temperature dependence of P_{vib} using our ambient temperature data, because F_{vib} is directly proportional to T (see Equation (3.1)). However, temperature (anharmonic) effects on the phonon DOS have not been accounted for, e.g., softening of phonon energies with increasing temperature, so derivatives of the best-fit polynomials of our $F_{vib}(V, T > 300\ \text{K})$ give only the harmonic component of the vibrational thermal pressure $\left(P_{vib}^{h}\right)$. Therefore, taking T = 5600 K, we find $P_{vib}^{h}(5600\ \text{K})$ = 37 ± 3 GPa and 40 ± 3 GPa at our smallest and largest compression points, respectively.

In order to obtain the total $P_{vib}(V,T)$ for T > 300 K, we must account for the anharmonic component of the vibrational thermal pressure $\left(P_{vib}^{anh}\right)$ using

$$P_{vib}\left(V,T\right) = P_{vib}^{h}\left(V,T\right) + \left[P_{vib}^{anh}\left(V,T\right) - P_{vib}^{anh}\left(V,300\ \text{K}\right)\right]. \tag{3.4}$$

Experimental data for temperature effects on ε-Fe's phonon DOS are not available for the *PT* conditions of interest here, so we rely on theoretical values for $P_{vib}^{anh}(V,T)$. *Dewaele et al.* (2006) fit *ab initio* anharmonic thermal pressures (*Alfè et al.*, 2001) with the formulation

$$P_{vib}^{anh}(V,T) = A_{vib}^{anh}\left(\frac{V}{V_0}\right)^{B_{vib}^{anh}} T^2 \tag{3.5}$$

(*Dorogokupets and Oganov*, 2006), and found A_{vib}^{anh} = 1.28 × 10^{-7} GPa·K^{-2} and B_{vib}^{anh} = 0.87. Applying Equation (3.5) and our $P_{vib}^{h}(V,T)$ to Equation (3.4), we obtain the total $P_{vib}(V,T)$.

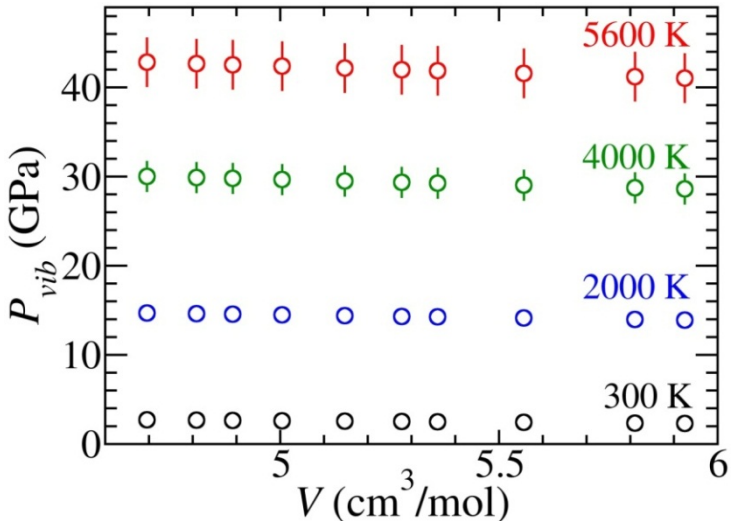

Figure 3.2. Vibrational thermal pressure of ε-Fe. Anharmonic effects have been accounted for in high-temperature values for the vibrational thermal pressure, $P_{vib}(T > 300\ \text{K})$; errors calculated from best-fit parameters are smaller than the symbol if not visible.

compression points, respectively, which corresponds to a 5% increase over the volume range of this study (Figure 3.2).

Finally, for the volume- and temperature-dependent electronic thermal pressure, we use the fit of *ab initio* values for $P_{el}(V,T)$ (*Alfè et al.*, 2001) with the formulation given in Equation (3.5) by *Dewaele et al.* (2006), who found $A_{el} = 4.82 \times 10^{-7}$ GPa·K^{-2} and $B_{el} = 0.339$. Applying our $P_{vib}(V,T)$ and this semi-empirical relationship for $P_{el}(V,T)$ to Equation (3.3), we find $P_{th}(300\ \text{K}) = 2.35$ and 2.74 GPa, and $P_{th}(5600\ \text{K}) = 55$ and 56 GPa at our smallest and largest compression points, respectively (Table 3.1). The small variation in P_{th} over our compression range and at a given temperature suggests only a weak volume dependence. However, P_{th} depends strongly on temperature, as can be seen in Figure 3.3.

Our $P_{vib}(V, 300\ \text{K})$ agree well with reported values for the quasi-harmonic Debye thermal pressure from *Dewaele et al.* (2006). In addition, our $P_{vib}^{h}(V,T)$ agree fairly well

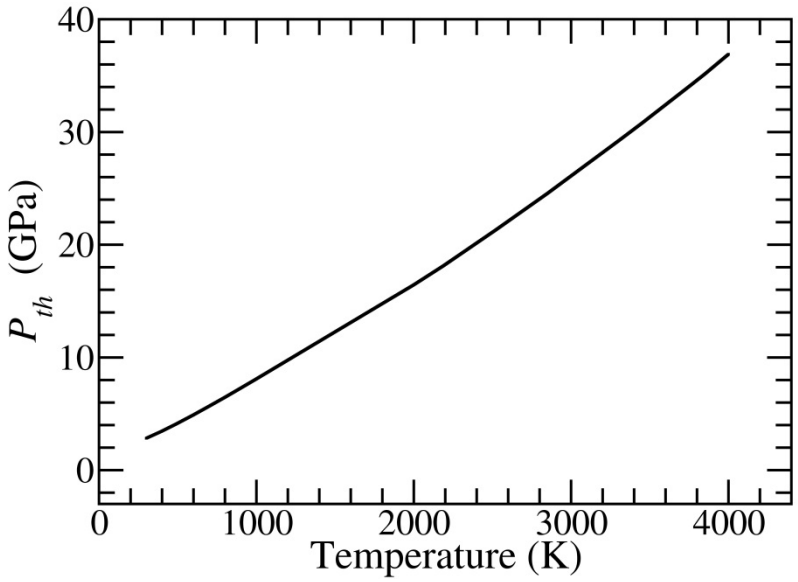

Figure 3.3. Temperature dependence of ε-Fe's total thermal pressure. The black curve gives the total thermal pressure (P_{th}) of ε-Fe as a function of temperature for the largest compression point considered in this chapter (V = 4.70 ± 0.02 cm^3/mol, P = 151 ± 5 GPa). We note that P_{th} is only weakly volume-dependent, but it has a nearly linear dependence on temperature.

with results from *ab initio* density-functional theory (DFT) calculations of the high-temperature harmonic thermal pressure by *Alfè et al.* (2001), although they reported a faster increase in P_{vib}^{h} with decreasing volume (~20% over the volume range of this study). Therefore, an experimental determination of $P_{vib}^{h}(V,T)$ agrees qualitatively with select first principles calculations. Finally, our $P_{th}(V,T)$ are in excellent agreement with a DFT calculation by *Vočadlo et al.* (2000), but our observed trend is opposite to that predicted by *Sha and Cohen* (2010a) in their DFT calculation of P_{th} for ε-Fe.

3.4 High-Pressure Melting Behavior

To constrain the high-pressure melting curve of ε-Fe, we start with Gilvarry's reformulation of Lindemann's original melting criterion, which states that melting occurs when the mean-square displacement of atoms (<u^2>) reaches a critical fraction (C) of the mean-square separation of nearest neighbor atoms (<r^2>) (*Gilvarry*, 1956b), or

$$\left\langle u^2 \right\rangle = C \left\langle r^2 \right\rangle. \tag{3.6}$$

It is important to note that Equation (3.6) predicts melting behavior based on a vibrational instability of the solid phase; in turn, the Lindemann melting criterion is often criticized for not having a strong thermodynamic basis since it does not consider the properties of the liquid state. However, it has been shown that the Lindemann melting criterion can be approximately derived from thermodynamic considerations of the relationship between the correlated atomic motion (entropy) of the liquid phase and vibrational properties of the solid phase for simple structures (*Wallace*, 1991; *Lawson*, 2009). Therefore, it has been argued that the Lindemann melting criterion provides a reasonable approximation for the melting curve shapes of monatomic, close-packed materials like ε-Fe.

We have defined $\langle u^2 \rangle$ above (Equation (3.2)), and now present its high-temperature formulation

$$\left\langle u^2 \right\rangle \approx k_B T \frac{2E_R}{3k_0^2} \int \frac{1}{E^2} D\left(E,V\right) dE \equiv \frac{T}{k_0^2} \frac{1}{T_{LM}} \tag{3.7}$$

where the Lamb-Mössbauer temperature (T_{LM}) is introduced for discussion and to simplify the expression (Table 3.1). Equation (3.7) is valid for $k_B T \gg E_{max}$, where E_{max} is the maximum (cutoff) energy of the phonon DOS. For our smallest and largest compression points, E_{max} is ~50 and ~70 meV, respectively (Figure 2.11). If we predict an E_{max} at 330 GPa and 300 K of ~100 meV, then this high-temperature approximation for $\langle u^2 \rangle$ is valid for $T \gg$ 1200 K, which is well below the temperatures discussed here.

Substituting Equation (3.7) into Equation (3.6) and rearranging, we obtain an expression for the harmonic melting temperature $\left(T_M^h\right)$ that is based on our measured phonon DOS via $T_{LM}(V)$:

$$T_M^h(V) \approx k_0^2 C \left\langle r^2 \right\rangle \cdot T_{LM}(V). \tag{3.8}$$

The value of k_0 does not depend on volume, C is thought to be approximately constant with volume (*Gilvarry*, 1956a), and $\langle r^2 \rangle \propto V^{2/3}$ for an hcp unit cell, so we rewrite Equation (3.8) in a reduced states form as

$$T_M^h(V) = T_{M0} \cdot \left(\frac{V}{V_{M0}} \right)^{2/3} \frac{T_{LM}(V)}{T_{LM}(V_{M0})}. \tag{3.9}$$

From Equation (3.9), our $T_{LM}(V)$ determines the shape of ε-Fe's melting curve, but an anchor melting point (represented by T_{M0} and V_{M0}) is necessary to calibrate the melting temperatures. For the anchor melting point, we use $T_M(P = 105\ \text{GPa}) = 3510 \pm 100$ K for ε-Fe, which was measured by *Ma et al.* (2004) using laser-heated static compression *in situ* synchrotron XRD. We convert their reported pressure to volume using the Vinet EOS (*Dewaele et al.*, 2006), and determine $T_{LM}(V_{M0})$ by quadratic interpolation of our measured $T_{LM}(V)$. Applying these anchor point values and our measured $T_{LM}(V)$ to Equation (3.9), we find $T_M^h = 2470 \pm 70$ K and 4100 ± 100 K at our smallest and largest compression points, respectively (Table 3.1). Reported errors account for measured uncertainties in V and T_{LM}, and an uncertainty in T_{M0} of 100 K (*Ma et al.*, 2004).

3.5 Discussion

Our harmonic melting points are based on measurements of the phonon DOS at 300 K, and therefore do not account for thermal pressure or anharmonic effects. To find the total pressure at each melting point, we apply our $P_{th}(V,T)$ to the high-PT EOS:

$$P(V,T_M) = P_V(V,300\,\text{K}) + \left[P_{th}(V,T_M) - P_{th}(V,300\,\text{K}) \right]. \tag{3.10}$$

P_V is the pressure determined by applying the Vinet EOS (*Dewaele et al.*, 2006) to our

measured volumes, and the square brackets contain our thermal pressure correction, which already accounts for anharmonic effects (see Section 3).

Additional experiments will be necessary in order to understand the role of anharmonicity on ε-Fe's phonon DOS and, in turn, the thermodynamic parameters determined here, i.e., the melting curve shape and thermal pressure. Previous experiments have looked in detail at the effects of temperature on the phonon DOS of low-pressure phases of iron, including the body-centered cubic (α-Fe) and face-centered cubic phases (γ-Fe) (*Kresch*, 2009). These studies found the phonon energies of α-Fe to have large and varying shifts, and significantly less variation in the phonon DOS shape of γ-Fe with temperature (i.e., less pronounced anharmonic effects). *Kresch* (2009) argues that one possible explanation for the different behavior with temperature is the fact that α-Fe has a more open structure compared to that of γ-Fe, and, in turn allows for more anharmonicity because the atoms have more room to "move about." Following the same logic, one might expect the properties of ε-Fe to be more closely related to those of γ-Fe, since they are both close-packed structures.

Results from studies that have previously investigated the effects of temperature on ε-Fe's phonon DOS seem to be consistent with the suggestion that the overall shape of the phonon DOS changes only slightly with temperature (*Shen et al.*, 2004; *Lin et al.*, 2005), based on qualitative inspection of their reported phonon DOS. However, we note that a more detailed comparison is not possible at this time because of sparse data coverage that is confined to low pressures, and the relatively low statistical quality that resulted from the limited duration of the stability of the laser-heating system. In order to quantitatively evaluate the role of anharmonicity on the thermodynamic parameters presented here, it will

be necessary to collect higher-statistical quality NRIXS datasets for ε-Fe at high-*PT* conditions with *in situ* XRD. Such experiments are very challenging, but will be important for improving our understanding of the properties of iron at core conditions.

In the absence of sufficient data on temperature effects on ε-Fe's phonon DOS, we now approximate an anharmonic correction term for our melting temperatures by investigating the temperature dependence of T_{LM}. We assume that the phonon DOS scales regularly with temperature, and that the temperature derivatives of the seismic velocity and the Debye sound velocity at constant volume are directly related (Appendix A). Combined with thermodynamic definitions, these assumptions give rise to an anharmonic correction term of –11% at our smallest compression point, or an anharmonic melting temperature (T_M) of ~2190 K (Appendix A). This anharmonic correction decreases at larger compressions, and for $P \geq 100$ GPa after accounting for P_{th}, our anharmonic melting temperatures are within the errors of our $T_M^h(V)$ (Table 3.1). The one exception, where T_M(4.89 cm^3/mol) exceeds T_M^h (4.89 cm^3/mol) by more than its error, may be related to the volume uncertainty of that compression point.

At the pressure of the core–mantle boundary, we find T_M(135 GPa) = 3500 ± 100 K. To benchmark this result, we find that it agrees well with the melting point reported by *Ahrens et al.* (2002) from shock-compression experiments: T_M(135 GPa) = 3400 ± 200 K. In addition, it agrees fairly well with T_M(135 GPa) = 3200 ± 100 K measured by *Boehler* (1993) (see Figure 2a in reference), who defined melting as the onset of convective motion in laser-heated static-compression experiments. However, our melting temperature lies well below that reported by *Williams et al.* (1987), who found T_M(135 GPa) = 4800 ± 200 K using a combination of static- and shock-compression experiments.

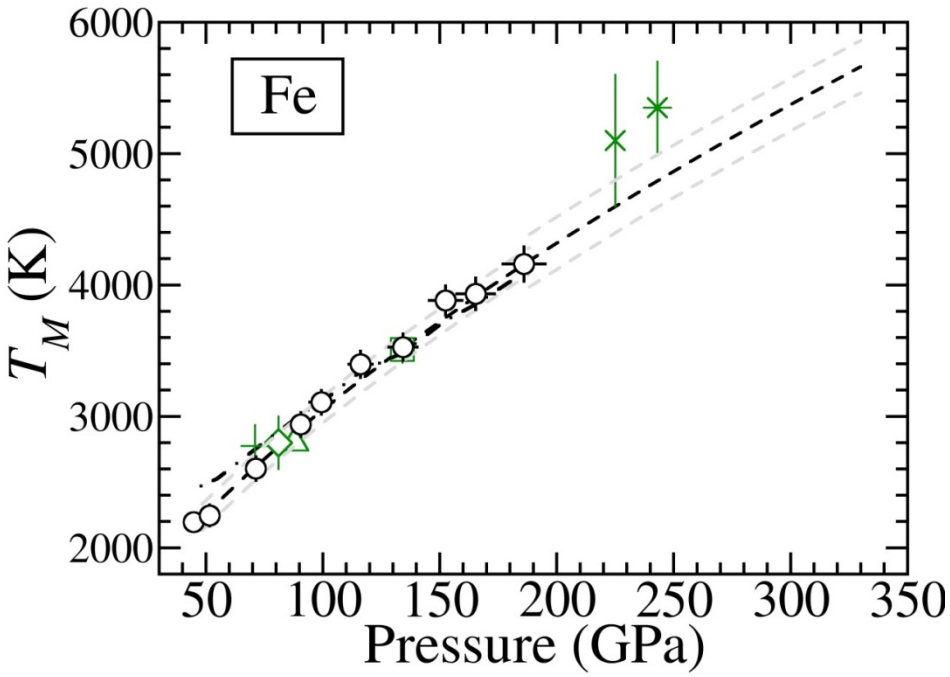

Figure 3.4. High-pressure melting behavior of ε-Fe. Black circles show melting points that account for thermal pressure and anharmonic effects. The black dashed line gives the fit and extrapolation of our melting points with Equation (3.11), and the gray dashed lines show uncertainties of ±100 K over our experimental compression range, and ±200 K beyond our compression range. The black dash-dotted line shows our harmonic melting temperatures, which account for thermal pressure. The green x, +, and * show results from shock-compression melting experiments by *Nguyen and Holmes* (2004), *Ahrens et al.* (2002), and *Brown and McQueen* (1986), respectively; the green triangle, square, and diamond show results from static-compression experiments by *Komabayashi and Fei* (2010), *Ma et al.* (2004), and *Shen et al.* (1998), respectively, where the final two have been corrected to account for thermal pressure following Equation (3.10).

To extrapolate our melting results beyond the compression range of this study, we apply two independent extrapolation equations. First, we use the Simon-Glatzel equation, which is an empirical relation for the pressure dependence of T_M given by

$$T_M = T_{M0}\left(\frac{P_M - P_{M0}}{x} + 1\right)^y, \tag{3.11}$$

where x and y are fitting parameters (*Simon and Glatzel*, 1929). For the anchor melting point (T_{M0} and P_{M0}), we again use the result from *Ma et al.* (2004), but we first apply our

thermal pressure correction since thermal pressure was not accounted for in their study. Using Equation (3.11) to fit and extrapolate our melting points, which account for thermal pressure and anharmonic effects, we find a melting temperature at the inner–core boundary (ICB, P = 330 GPa) of 5700 ± 100 K (Figure 3.4). Here we have assigned the error to be that of our largest compression point's harmonic melting temperature, which is slightly larger than the error derived from fitting parameter uncertainties.

The second extrapolation equation is a commonly used approximate form of Lindemann's melting relation

$$T_M\left(V\right) = T_{M0}\exp\left[2\gamma_{M0}\left(1-\frac{V}{V_{M0}}\right)+\frac{2}{3}\ln\left(\frac{V}{V_{M0}}\right)\right] \tag{3.12}$$

(*Poirier*, 2000), where the vibrational Grüneisen parameter at the volume of the anchor melting point (γ_{M0}) serves as the fitting parameter. Taking T_{M0} and V_{M0} from *Ma et al.* (2004), we fit our ten melting points with Equation (3.12) and find γ_{M0} = 1.65 ± 0.06. We then simultaneously solve for $P(V,T_M)$ and $T_M(V)$ (Equations (3.10) and (3.12)) in order to determine the volume of ε-Fe at the pressure of the ICB that accounts for the melting temperature-dependent thermal pressure. The result is a self-consistent melting temperature for ε-Fe at 330 GPa of 5500 ± 100 K, where the error is assigned as before.

Combining the results of our two independent extrapolations, we find the melting temperature of ε-Fe at the ICB to be T_M(330 GPa) = 5600 ± 200 K. To further benchmark this result and investigate its sensitivity to the anchor melting point, we perform the same thermal pressure correction, anharmonic correction, and extrapolation procedures with alternate anchor melting points. Anchoring our melting curve shape with the melting point measured by *Jackson et al.* (2012) at 82 GPa (after accounting for P_{th}) and 3025 K, we find

Table 3.2. Anchor melting point parameters.[a]

	***Ma et al.* (2004)**	***Jackson et al.* (2012)**	***Shen et al.* (1998)**	***Komabayashi and Fei* (2010)**
T_{M0} (K)	3510(100)	3025(115)	2800(50)	2800
V_{M0} (cm^3/mol)	5.01	5.35	5.47	5.38
P_{M0} (GPa)	134	82(5)	81	88
$T_{LM}(V_{M0})$ (K)	3390	2820	2650	2770
X	160(40)	110(20)	150(30)	230(30)
Y	1.7(5)	1.78(5)	1.6(5)	1.4(5)
γ_{M0}	1.65(6)	1.68(6)	1.75(6)	1.72(6)

[a]Parameters are calculated for the melting points measured by *Ma et al.* (2004), *Jackson et al.* (2012), *Shen et al.* (1998), and *Komabayashi and Fei* (2010), as described in the text. P_{M0} accounts for thermal pressure, assuming constant volume for all studies except *Jackson et al.* [2012], who report a thermal pressure correction that is half as large as that predicted by our constant volume considerations; parameters x and y are from Equation (3.11), and γ_{M0} is from Equation (3.12).

T_M(330 GPa) ~ 5500 to 5800 K. A similar melting temperature range is found when anchoring our melting curve shape with the triple point measured by *Shen et al.* (1998) at 81 GPa (after accounting for P_{th}) and 2800 K. Finally, anchoring our melting curve shape with *Komabayashi and Fei's* (2010) reported triple point at 90 GPa and 2800 K, we find T_M(330 GPa) ~ 5500 K from Equation (3.11), and ~5200 K from Equation (3.12). Therefore, using the shape we determine from the phonon DOS, the melting temperature of ε-Fe at the ICB predicted from the melting points reported by *Ma et al.* (2004), *Shen et al.* (1998), and *Komabayashi and Fei* (2010) all agree within their uncertainties, thus serving as benchmarks for our approach (Table 3.2).

Finally, we note that considering the uncertainties of our melting curve shape and our two independent extrapolations, our results intersect the range of values reported in the shock-compression studies of *Nguyen and Holmes* (2004) and *Brown and McQueen* (1986) (Figure 3.4).

From Equation (3.10), our $P_{th}(V,T)$, and our T_M(330 GPa) = 5600 ± 200 K, we find the density of pure ε-Fe to be ρ_{Fe}(330 GPa) = 13.50 ± 0.03 g/cm^3. This ρ_{Fe} can also be reported as a core density deficit (CDD), or the percent difference between the density of ε-Fe under core conditions and the seismically inferred density of the core. The preliminary reference Earth model (PREM) predicts a density at the ICB of 12.76 g/cm^3, based on observations of Earth's normal modes and seismic wave travel times (*Dziewonski and Anderson*, 1981). Together with our ρ_{Fe}(330 GPa, 5600 ± 200 K), this gives a CDD of 5.5 ± 0.2%, where the uncertainty reflects the errors we assigned to our extrapolated melting temperatures. Our CDD value agrees well with *Komabayashi and Fei's* (2010) recently calculated CDD of 5.3 wt%, which is based on static-compression experiments and a lower melting temperature for ε-Fe at the ICB.

The CDD offers insight into the amount of light elements present in the core (*Poirier*, 2000; *Hemley and Mao*, 2001). However, the alloying of Ni and light elements (e.g., S, Si, O, C, H) may affect the melting temperature and other thermoelastic parameters of ε-Fe (e.g., *Boehler*, 1992; *Poirier*, 2000; *Seagle et al.*, 2008) and, in turn, complicate the determination of the true composition of the core by, for example, altering the P_{th} correction. In order to better constrain the CDD, it would be ideal to use the density of an Fe-Ni alloy at ICB conditions as a reference, rather than pure Fe. While the EOS of Fe-Ni is thought to be similar to that of pure Fe (*Mao et al.*, 1990), the effect of alloying on P_{th} is not well-known.

3.6 Implications and Conclusions

It is important to note that a significant amount of light elements in Earth's solid inner core has far-reaching implications for the thermal properties of this remote region.

First, geodynamo theory argues that the Earth's magnetic field is generated by the rotation and vigorous convection of the electrically conductive liquid outer core. Convection of the outer core is driven by a combination of thermal buoyancy and chemical buoyancy, the latter of which results from the exclusion of light elements from the solid inner core and, in turn, the formation of a relatively light fluid above the inner–core boundary (ICB). The relative importance of thermal and chemical buoyancy is not well constrained, but in his review paper of geodynamo models, *Buffet* (2000) predicts that 80% of the power for generating the goedynamo comes from chemical buoyancy. If a significant amount of light elements must be present in the inner core to match seismic observations, then either thermal buoyancy must play a larger role in driving convection in the outer core, or another mechanism is needed to generate the geodynamo.

In addition, the melting (freezing) point depression at the conditions of Earth's ICB is often estimated from a comparison of the melting temperatures of iron alloys and pure iron. Such a comparison is very difficult to make, since even the seemingly simplest component—the melting behavior of pure ε-Fe at the conditions of Earth's ICB—is not well-known (see Section 1.2 for a more detailed review). If a significant amount of light elements are present in the solid inner core, then such a comparison becomes exceedingly complex, since multiple phases may be present in the inner core, all of whose melting behaviors must be accurately measured and considered.

In summary, we determined ε-Fe's high-pressure melting behavior and thermal pressure from measurements of its total phonon DOS at 300 K. Accounting for thermal pressure and anharmonic effects, we found ε-Fe's melting temperature at the pressure of the CMB to be 3500 ± 100 K. In addition, by combining the results of two independent

extrapolations of our melting curve, we found ε-Fe's melting temperature at the ICB to be 5600 ± 200 K. We have presented benchmarking cases and show that the melting temperatures of ε-Fe predicted from our approach are in agreement with shock-compression studies. Finally, our predicted melting temperature for ε-Fe at the ICB corresponds to a CDD of 5.5 ± 0.2% for the solid inner core, which has important implications for our understanding of the thermal properties of Earth's core.

Chapter 4

Grüneisen parameter of hcp-Fe[2]

4.1 Introduction

Iron is thought to be the main constituent in the Earth's core (e.g., *McDonough*, 2003), and existing data suggest that hexagonal close-packed iron (ε-Fe) is the stable phase at core conditions (*Alfè et al.*, 2001; *Ma et al.*, 2004; *Dewaele et al.*, 2006; *Tateno et al.*, 2010). Therefore, the accurate determination of ε-Fe's thermophysical properties is of fundamental importance for studies of the deep Earth. For example, accurate measurements of ε-Fe's thermodynamic Grüneisen parameter (γ_{th}) would aid in the determination of its high-pressure thermal equation of state, because γ_{th} is the coefficient that relates thermal pressure to thermal energy per unit volume. In addition, γ_{th} is used to reduce shock-compression data to isothermal data and to calculate adiabatic gradients (*Poirier*, 2000), both of which are important applications for furthering our understanding of Earth's core.

The thermodynamic Grüneisen parameter is made up of electronic and vibrational components, the latter of which is directly related to the volume dependence of the phonon

[2] Revised over what was previously published as *Murphy et al.* (2011b).

density of states (DOS). The vibrational Grüneisen parameter (γ_{vib}) of ε-Fe is particularly important because it is used to extrapolate available melting data to the inner–core boundary, where Earth's solid inner core and liquid outer core are in contact. However, reported values of γ_{vib} are not in complete agreement (*Jeanloz*, 1979; *Brown and McQueen*, 1986; *Dubrovinsky et al.*, 2000a; *Lübbers et al.*, 2000; *Alfè et al.*, 2001; *Anderson et al.*, 2001; *Ahrens et al.*, 2002; *Giefers et al.*, 2002; *Dewaele et al.*, 2006), and are often based on indirect or approximate determinations. As a result, uncertainty and confusion surround γ_{vib}, and a wide range of extrapolated melting temperatures have been reported.

An approximate form of γ_{vib} is the Debye Grüneisen parameter (γ_D), which is based on Debye's approximation that the entire phonon DOS can be described by its low-energy region, where the dispersion relation is linear. In past studies, γ_D has been approximated from x-ray diffraction experiments via the Rietveld structural refinement method. From this refinement, one obtains an approximate mean-square atomic displacement and, in turn, the Debye temperature, which is related to γ_D (*Dubrovinsky et al.*, 2000a; *Anderson et al.*, 2001). In addition, researchers have approximated γ_D from adiabatic decompression experiments via a thermodynamic relationship that relates γ and $\left(\partial T/\partial P\right)_S$ (*Boehler and Ramakrishnan*, 1980).

Here we determine $\gamma_{vib}(V)$ from the total phonon DOS, which we measured at eleven compression points between pressures of 30 GPa and 171 GPa using nuclear resonant inelastic x-ray scattering (NRIXS) and *in situ* x-ray diffraction (XRD) experiments (*Sturhahn et al.*, 1995). In addition, we determine $\gamma_D(V)$ for ε-Fe from the volume dependence of its Debye sound velocity, which we obtain from the low-energy region of the phonon DOS (*Sturhahn and Jackson*, 2007). Our long NRIXS data-collection

times and high-energy resolution resulted in the high statistical quality that is necessary to derive γ_{vib} and γ_D.

4.2 Experimental

For details of our diamond-anvil cell (DAC) preparations, experimental procedures, and data analysis, see Chapter 2. The analysis, results, and discussion in this chapter are based on our entire NRIXS and *in situ* XRD dataset (11 compression points). To derive γ_{vib} and γ_D, we rely on our *in situ* measured volumes. To present our results on a common scale and for discussion, we convert our measured volumes to pressures using the Vinet equation of state (EOS) (*Dewaele et al.*, 2006) (Table 4.1).

From our NRIXS experiments, we obtained ε-Fe's total phonon DOS, $D(E,V)$ (*Sturhahn*, 2000; *Sturhahn and Jackson*, 2007), from which we directly determined two parameters that relate γ_{vib} to the vibrational thermal pressure via a Mie-Grüneisen type relationship. The vibrational component of the specific heat capacity per ^{57}Fe atom (C_{vib}) is given by

$$C_{vib}(V) = k_B \int \left(\frac{\beta E}{2\sinh(\beta E/2)} \right)^2 D(E,V)\,\mathrm{d}E, \tag{4.1}$$

and the vibrational internal energy per ^{57}Fe atom (U_{vib}) is given by

$$U_{vib}(V) = \frac{1}{2} \int E \coth \frac{\beta E}{2} D(E,V)\,\mathrm{d}E \tag{4.2}$$

(Table 4.1), where k_B is Boltzmann's constant and $\beta = (k_B T)^{-1}$ is the inverse temperature (*Sturhahn*, 2004). In Equations (4.1) and (4.2), the phonon DOS has been normalized by $\int D(E)\,dE = 3$.

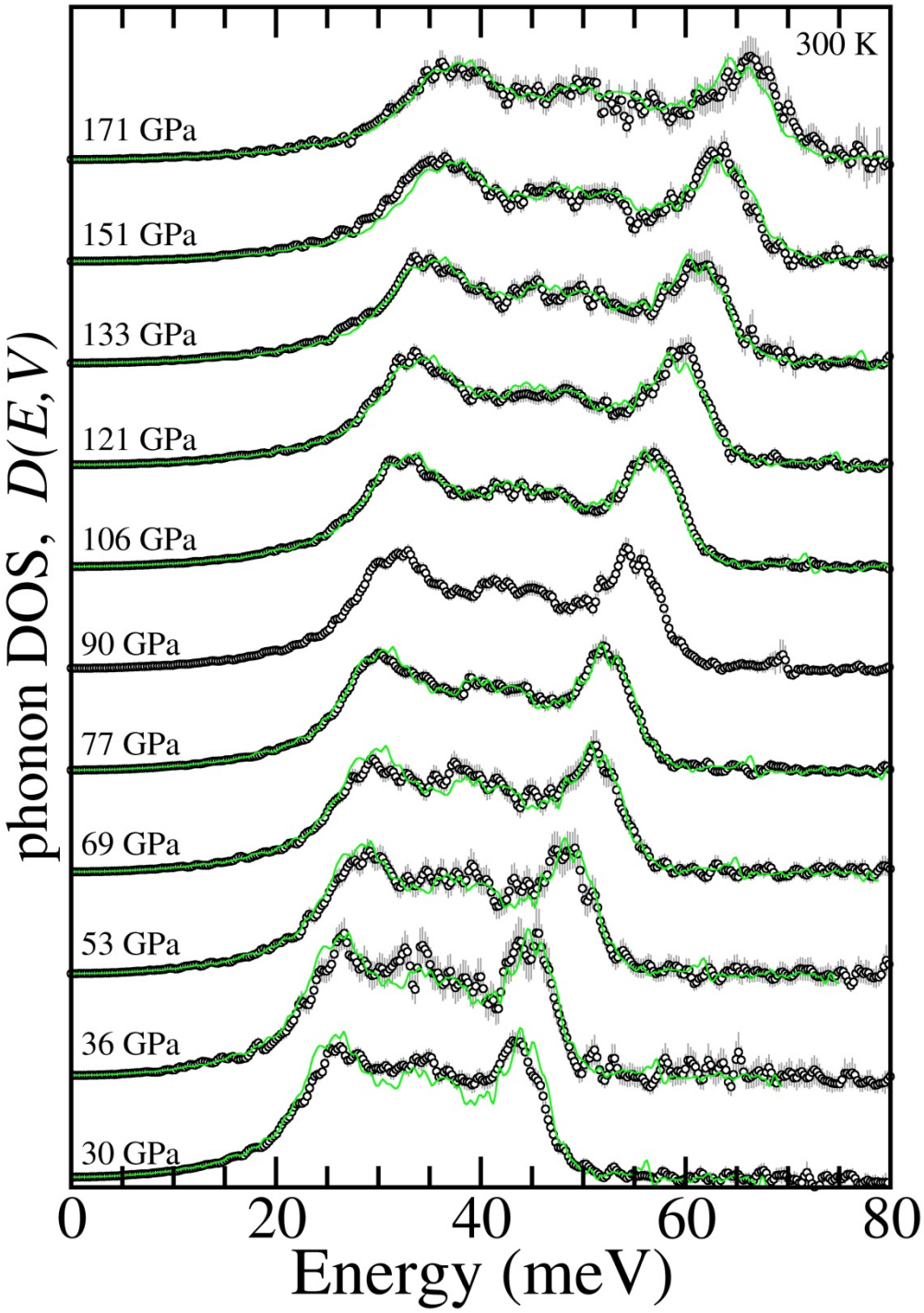

Figure 4.1. Comparison of measured and scaled phonon DOS of ε-Fe. Black curves show the measured phonon DOS at each compression point; green curves show the phonon DOS at V_i = 5.15 ± 0.02 cm^3/mol (P = 90 ± 3 GPa), scaled to each other measured phonon DOS using Equation (4.3) and the appropriate scaling parameter for each pair of phonon DOS, following the procedure described in Section 4.4.

4.3 Vibrational Grüneisen Parameter

Qualitative inspection of our data reveals that our phonon DOS are similar in shape at all compression points, and that any pair of phonon DOS appears to be related by a single overall scaling parameter. This suggestion can be evaluated in Figure 4.1, where we plot our measured phonon DOS at each compression point in black, along with the phonon DOS at V_i = 5.15 ± 0.02 cm^3/mol (P = 90 ± 3 GPa) that has been scaled using

$$D\left(E,V\right)=\xi\left(V/V_i\right)\cdot D\left[\xi\left(V/V_i\right)\cdot E,V_i\right] \tag{4.3}$$

and the appropriate scaling parameter (ξ) for each pair of phonon DOS in green. We note that ξ is energy independent and $\xi(1) = 1$.

To determine the appropriate scaling parameter for each pair of phonon DOS, we assign one spectrum to be an initial reference phonon DOS, (E,V_i), to which we apply Equation (4.3). We then minimize the least-squares difference between this scaled reference phonon DOS and each of the other ten unscaled phonon DOS, (E,V_j) (Figure 4.1). This process is repeated with each phonon DOS serving as the reference, resulting in eleven datasets that each contain ten data points. To incorporate our entire scaling parameter analysis into each dataset, we then rescale all of our data to each reference volume (V_i) by

$$\xi\left(\frac{V_k}{V_i}\right)=\xi\left(\frac{V_k}{V_j}\right)\cdot\xi\left(\frac{V_j}{V_i}\right). \tag{4.4}$$

In Figure 4.2, we show the result of this scaling analysis for an example reference phonon DOS: $\xi(V_k/V_i)$ at V_i = 5.15 ± 0.02 cm^3/mol. Given the smooth trend and small errors, we find that a generalized scaling law successfully describes the volume dependence of ε-Fe's phonon DOS. We note that a similar analysis was previously performed by *Alfè et*

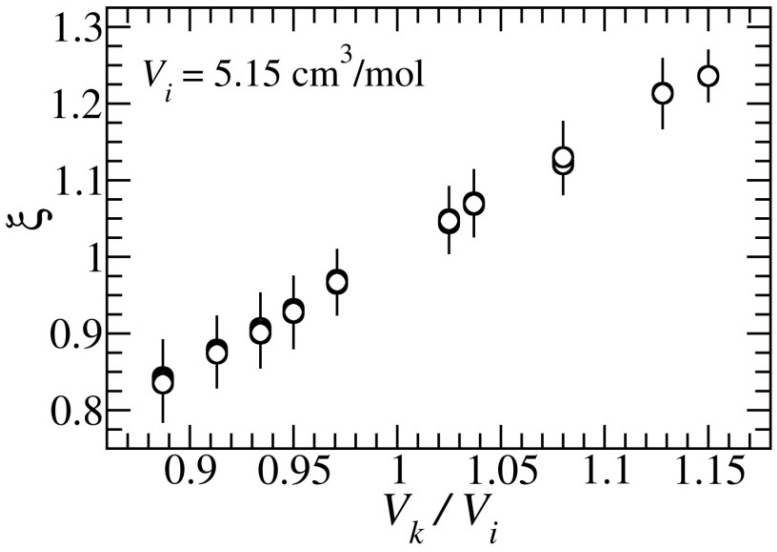

Figure 4.2. Scaling parameter analysis demonstration. The scaling parameter (ξ) is plotted as a function of the relative volumes of a scaled reference phonon DOS, (E,V_i), and all other unscaled phonon DOS, $\mathcal{D}(E,V_k)$. In this example, V_i = 5.15 ± 0.02 cm^3/mol (P = 90 ± 3 GPa). All scaling analysis data have been included, following Equation (4.4).

al. [2001], who investigated the volume dependence of dispersion curves for ε-Fe using *ab initio* density-functional theory (DFT) calculations. *Alfè et al.* [2001] reported $\xi(1.244)$ = 1.409 for V_i = 4.20 cm^3/mol, which agrees fairly well with the value predicted by extrapolating our results to the same volume ratio. However, this comparison is largely qualitative because the scaling parameter reported by *Alfè et al.* [2001] was determined for dispersion curves calculated at T = 4000 K, and V_i = 4.20 cm^3/mol is beyond the compression range of our measurements.

Finally, we derive an expression for the relationship between γ_{vib} and the volume dependence of the scaling parameter, $\xi(V/V_i)$, by combining the commonly used parameterization

$$\gamma_{vib} = \gamma_{vib,i}\left(\frac{V}{V_i}\right)^q, \tag{4.5}$$

with the definition of the vibrational Grüneisen parameter

$$\gamma_{vib} = \frac{\partial \ln \xi\left(V/V_i\right)}{\partial \ln V_i}, \tag{4.6}$$

where $\gamma_{vib,i}$ and V_i are the vibrational Grüneisen parameter and volume at a reference compression, and q is a fitting parameter. Substituting Equation (4.5) into Equation (4.6) and integrating, we obtain

$$\xi\left(\frac{V}{V_i}\right) = \xi_i \exp\left\{\frac{\gamma_{vib,i}}{q}\left[\left(\frac{V}{V_i}\right)^q - 1\right]\right\}, \tag{4.7}$$

when $q \neq 0$. At the reference compression, $V = V_i$ and $\xi_i = \xi(1) = 1$, so Equation (4.7) simplifies to

$$\xi\left(\frac{V}{V_i}\right) = \exp\left(\frac{-\gamma_{vib,i}}{q}\right)\exp\left\{\frac{\gamma_{vib,i}}{q}\left(\frac{V}{V_i}\right)^q\right\}. \tag{4.8}$$

Fitting each of our eleven $\xi(V_k/V_i)$ datasets with Equation (4.8) and allowing both $\gamma_{vib,i}$ and q to vary freely, we found large uncertainties in q, with the most tightly constrained fit being q(5.15 cm^3/mol) = 0.8 ± 0.7. Therefore, we reperformed the fits with q fixed to one of three assigned values: first, q(5.15 cm^3/mol) = 0.8; second, the commonly assumed q = 1; and third, q = 1.2. Finally, we fit the resulting three sets of $\gamma_{vib,i}(V)$ with Equation (4.5) and obtained ambient pressure $\gamma_{vib,0}$ = 1.88 ± 0.02 for q = 0.8; $\gamma_{vib,0}$ = 1.98 ± 0.02 for q = 1.0; and $\gamma_{vib,0}$ = 2.08 ± 0.02 for q = 1.2. These results can be combined and presented as $\gamma_{vib,0}$ = 2.0 ± 0.1, where we assign the error to reflect fitting parameter uncertainties and the range associated with our fixed q values.

4.4 Debye Grüneisen Parameter

The low-energy region of a material's phonon DOS is related to its Debye sound velocity (v_D), provided it is parabolic ("Debye-like"). We determined v_D for ε-Fe at each of our eleven compression points (Table 4.1) by using an exact relation for the dispersion of low-energy acoustic phonons with our *in situ* measured volumes, and determining the best

energy range to use for this fit (see Equation (9) in *Sturhahn and Jackson* (2007)). The large compression range and high statistical quality of our data allow us to calculate a very accurate $v_D(V)$, which is related to γ_D by

$$\gamma_D = \frac{1}{3} - \frac{V}{v_D}\left(\frac{\partial v_D}{\partial V}\right)_T . \tag{4.9}$$

Combining Equations (4.9) and (4.5) and integrating, we obtain the expression

$$v_D = v_{D,0}\left(\frac{V}{V_0}\right)^{1/3} \exp\left\{-\frac{\gamma_{D,0}}{q}\left[\left(\frac{V}{V_0}\right)^q - 1\right]\right\}, \tag{4.10}$$

which depends on the ambient pressure Debye sound velocity ($v_{D,0}$), Debye Grüneisen parameter ($\gamma_{D,0}$), and volume (V_0) (*Dewaele et al.*, 2006), and the fitting parameter q (*Sturhahn and Jackson*, 2007). Therefore, to determine $\gamma_D(V)$, we fit our $v_D(V)$ with Equation (4.10), fixing q as in Section 3, and found $\gamma_{D,0} = 1.70 \pm 0.07$ and $v_{D,0} = 3.66 \pm 0.06$ km/s for $q = 0.8$; $\gamma_{D,0} = 1.78 \pm 0.07$ and $v_{D,0} = 3.63 \pm 0.06$ km/s for $q = 1.0$; and $\gamma_{D,0} = 1.87 \pm 0.08$ and $v_{D,0} = 3.60 \pm 0.06$ km/s for $q = 1.2$. Combining these results as in Section 3, we find $\gamma_{D,0} = 1.8 \pm 0.1$ and $v_{D,0} = 3.63 \pm 0.09$ km/s.

4.5 Discussion

A generalized scaling law describes the volume dependence of ε-Fe's phonon DOS fairly well. However, it is important to note that the relative intensity of the middle vibrational mode decreases with respect to the low- and high-energy vibrational modes with compression (Figure 4.1). This slight deviation from perfectly generalized scaling could contribute to the poorly constrained nature of q, which is the parameter that controls the rate at which γ_{vib} and γ_D decrease with decreasing volume.

Our $\gamma_{vib,i}$ and γ_D at each compression point are listed in Table A.1 (in Appendix A),

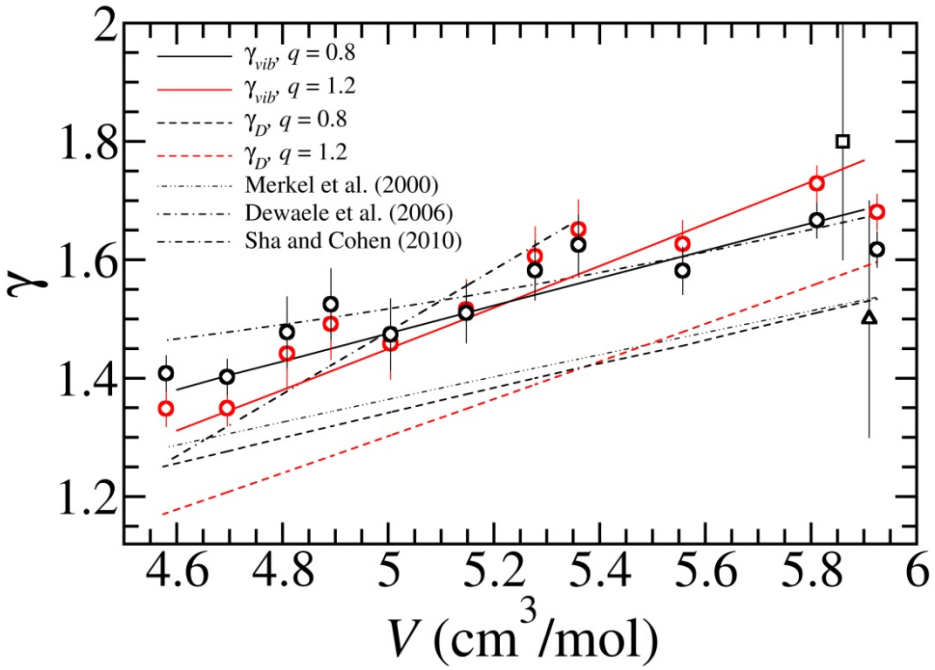

Figure 4.3. Grüneisen parameters of ε-Fe. Individual $\gamma_{vib,i}$ from Section 4.3 are plotted as circles for q = 0.8 (black) and q = 1.2 (red); fitted curves of $\gamma_{vib,i}$ with Equation (4.5) (solid lines) and $\gamma_D(V)$ (dashed lines) are shown for q = 0.8 (black lines) and q = 1.2 (red lines). The dash-dotted line shows $\gamma_D(V)$ reported by *Dewaele et al.* (2006), which is based in part on their XRD data; the black square and triangle show the individual γ_D determined from NRIXS measurements by *Lübbers et al.* (2000) and *Giefers et al.* (2002), respectively, at the average volume of each experimental pressure range; the dash-dot-dotted line shows $\gamma_{th}(V)$ determined by *Merkel et al.* (2000) using Raman spectroscopy experiments; and the dash-dash-dotted line shows γ_{th} reported by *Sha and Cohen* (2010a) in their Figure 8, based on the results of their DFT calculations at T = 500 K.

and are plotted with their fitted curves in Figure 4.3. We find that γ_{vib} is systematically ~10% larger than γ_D, which may be explained in part by the fact that γ_{vib} is derived from the entire phonon DOS, while γ_D depends only on the acoustic regime (i.e., the low-energy region). There is not enough information to determine whether this discrepancy is related to sample texturing, which we observed in our five largest compression points (see supplemental materials).

Our $\gamma_{vib}(V)$ for q = 0.8 agree fairly well with $\gamma_v(V)$ determined by *Anderson et al.* (2001) from intensity changes in static-compression XRD lines with compression. In

Table 4.1. Specific heat capacity, internal energy, and Debye sound velocity of ε-Fe from NRIXS data.[a]

V (cm^3/mol)	P (GPa)	C_{vib} (k_B/atom)	U_{vib} (meV/atom)	v_D (km/s)
5.92(2)	30(2)	2.62(2)	87.9(9)	4.36(3)
5.81(1)	36(2)	2.60(4)	88.5(1.8)	4.37(6)
5.56(1)	53(2)	2.54(3)	90.4(1.5)	4.57(4)
5.36(1)	69(3)	2.49(2)	92.0(1.2)	4.80(4)
5.27(2)	77(3)	2.47(2)	92.6(8)	4.93(3)
5.15(2)	90(3)	2.44(2)	93.6(9)	5.13(3)
5.00(2)	106(3)	2.40(2)	95.0(1.0)	5.23(3)
4.89(2)	121(3)	2.36(2)	96.4(1.0)	5.33(4)
4.81(2)	133(4)	2.33(2)	97.2(1.2)	5.47(5)
4.70(2)	151(5)	2.30(2)	98.0(1.3)	5.72(10)
4.58(2)	171(5)	2.25(3)	100(2)	5.64(7)

[a]Volume (V) was measured with *in situ* XRD and converted to pressure (P) using the Vinet EOS (*Dewaele et al.*, 2006) (Tables 2.1 and 2.2); the vibrational specific heat capacity (C_{vib}) and vibrational internal energy (U_{vib}) per ^{57}Fe atom were determined from the integrated phonon DOS (Equations (4.1) and (4.2)); and the Debye sound velocity (v_D) was obtained from the low-energy region of the measured phonon DOS and our *in situ* measured volumes, and accounts for ^{57}Fe enrichment levels. Values in parentheses give uncertainties for the last significant digit(s).

addition, the slope for q = 0.8 agrees fairly well with that of $\gamma_D(V)$ reported by *Dewaele et al.* (2006), which was determined from a combination of previously reported shock-compression data, an assumed volume dependence of γ, and their static-compression XRD experiments. However, $\gamma_D(V)$ from *Dewaele et al.* (2006) is ~10% larger than our $\gamma_D(V)$. Finally, two previous NRIXS experiments on ε-Fe reported volume-independent γ_D up to 42 GPa; our $\gamma_D(V)$ agree well with that reported by *Giefers et al.* (2002), but are significantly lower than that reported by *Lübbers et al.* (2000) (Figure 4.3). We note that the discrepancy with the latter study may be related to the fact that the energy scale they used was incorrect.

Although γ_{vib} is only one component of the total γ_{th}, we compare our results with

reported values for ε-Fe's $\gamma_{th}(V)$. *Merkel et al.* (2000) used Raman spectroscopy experiments to determine $\gamma_0 = 1.68 \pm 0.2$ for $q = 0.7 \pm 0.5$, which is very similar to our $\gamma_D(V)$ for $q = 0.8$. *Sha and Cohen* (2010a) performed DFT calculations to find $\gamma_{th}(V)$ for nonmagnetic ε-Fe at 500 K. Their result agrees fairly well with our high-pressure $\gamma_{vib,i}$ but has a steeper slope than our fitted curves, possibly due to different EOS parameters (Figure 4.3). Finally, *Brown and McQueen* (1986) found $\gamma = 1.56$ at a density of 12.54 g/cm^3 using shock-compression experiments, which is larger than our predicted value at the same density (~1.3). However, we note that the *Brown and McQueen* (1986) data point is for liquid iron, whereas our results are for solid ε-Fe at 300 K.

To explore the geophysical applications of γ_{vib}, we first investigate the volume-dependent vibrational thermal pressure (P_{vib}) of ε-Fe by applying our $\gamma_{vib}(V)$ to a Mie-Grüneisen type relationship:

$$P_{vib} = \left(\frac{C_{vib}\gamma_{vib}}{C_{vib} + C_{el}} \right) \frac{U_{vib}}{V}. \tag{4.11}$$

$C_{vib}(V)$ and $U_{vib}(V)$ are obtained from our measurements (Equations (4.1) and (4.2)), and we use approximate values for the electronic component of the specific heat capacity (C_{el}) from *Alfè et al.* (2001). Applying these values and our $\gamma_{vib}(V)$ to Equation (4.11), we find P_{vib}(300 K) = 2.39 ± 0.08 GPa and 2.75 ± 0.1 GPa at our smallest (30 GPa) and largest (171 GPa) compression points, respectively. Reported errors account for the previously mentioned uncertainties in γ_{vib} and our measured uncertainties in V, C_{vib}, and U_{vib}. These values agree very well with our P_{vib} calculated directly from the integrated phonon DOS (*Murphy et al.*, 2011a), which were 2.31 ± 0.06 GPa and 2.74 ± 0.06 GPa at our smallest and largest compression points. Finally, accounting for electronic and anharmonic

contributions at high temperatures following *Murphy et al.* (2011a), we find the total thermal pressure (P_{th}) of ε-Fe at our new, largest compression point (V = 4.58 cm^3/mol) to be P_{th}(2000 K) = 16 GPa, P_{th}(4000 K) = 37 GPa, and P_{th}(5600 K) = 56 GPa.

Next, we use our $\gamma_{vib}(V)$ to estimate the high-pressure melting behavior of ε-Fe by applying it to a commonly used, approximate form of the empirical Lindemann melting criterion

$$T_M(V) = T_M^{ref}\left(\frac{V}{V_M^{ref}}\right)^{2/3} \exp\left\{\frac{2\gamma_{vib}^{ref}}{q}\left[1-\left(\frac{V}{V_M^{ref}}\right)^{q}\right]\right\}, \tag{4.12}$$

where T_M^{ref}, V_M^{ref}, and γ_{vib}^{ref} are the melting temperature, volume, and vibrational Grüneisen parameter at a reference melting point. We take the melting point measured by *Ma et al.* (2004) using laser-heated synchrotron x-ray diffraction experiments as the reference: T_M^{ref} = 3510 ± 100 K at $P_{300\ K}$ = 105 GPa, or V_M^{ref} = 5.01 cm^3/mol using the Vinet EOS (*Dewaele et al.*, 2006; *Murphy et al.*, 2011a). From Equation (4.5) and our results in Section 3, we find γ_{vib}^{ref} = 1.47 ± 0.1. Applying these reference point values to Equation (4.12), we estimate T_M(4.70 cm^3/mol) = 4100 ± 100 K and T_M(4.58 cm^3/mol) = 4300 ± 100 K for ε-Fe. We note that replacing γ_{vib}^{ref} with γ_D^{ref} = 1.32 ± 0.1 (see Section 4.4) results in melting temperatures that are ~3% smaller at these compressions.

Finally, we account for thermal pressure at the melting temperatures of our two largest compression points following *Murphy et al.* (2011a), which gives P_{th}(4.70 cm^3/mol, 4100 K) = 38 GPa and P_{th}(4.58 cm^3/mol, 4300 K) = 40 GPa, respectively. Applying the corresponding thermal pressure correction assuming constant volume, we find T_M(186 GPa) = 4100 ± 100 K and T_M(208 GPa) = 4300 ± 100 K. These estimated melting points agree very well with our previously reported high-pressure melting behavior of ε-Fe,

determined from the mean-square displacement of ^{57}Fe atoms which we obtained directly from the integrated phonon DOS (*Murphy et al.*, 2011a).

Appendix A

Details of Melting Temperature Calculation

Relevant parameters for determining the high-pressure melting behavior of ε-Fe with Equations (3.9)–(3.12) and the *Ma et al.* (2004) or *Jackson et al.* (2012) anchor melting point are given in Table 3.2. To approximate an anharmonic correction term for our harmonic melting temperatures, we begin with the hypothesis that ε-Fe's phonon DOS scales regularly with temperature:

$$D\left(E,V,T\right)=\xi\left(V,T\right)D\left(\xi\left(V,T\right),E,V_0,T_0\right) \tag{A.1}$$

where the scaling parameter (ξ) is independent of energy and $\xi(V_0,T_0) = 1$. Together with the low-energy Debye-like description of the phonon DOS (*Hu et al.*, 2003), Equation (A.1) gives

$$\frac{\xi^3\left(V,T\right)v_D^3\left(V,T\right)}{V}=\frac{v_D^3\left(V_0,T_0\right)}{V_0}, \tag{A.2}$$

where v_D is the Debye sound velocity, and the subscript *0* refers to some reference conditions.

Next, we write the temperature derivatives of v_D and the seismic velocity (v_ϕ) at constant volume, which are given by

$$3v_D^{-3}\left(\frac{\partial \ln v_D}{\partial \ln T}\right)_V = v_p^{-3}\left(\frac{\partial \ln v_p}{\partial \ln T}\right)_V + 2v_S^{-3}\left(\frac{\partial \ln v_s}{\partial \ln T}\right)_V$$
$$v_\phi^{\,2}\left(\frac{\partial \ln v_\phi}{\partial \ln T}\right)_V = v_p^{\,2}\left(\frac{\partial \ln v_p}{\partial \ln T}\right)_V - \frac{4}{3}v_s^{\,2}\left(\frac{\partial \ln v_s}{\partial \ln T}\right)_V , \quad \text{(A.3)}$$

where v_p and v_s are the compressional and shear sound velocities, respectively. The derivatives in Equation (A.3) are related by

$$\left(\frac{\partial \ln v_D}{\partial \ln T}\right)_V = \left(\frac{\partial \ln v_\phi}{\partial \ln T}\right)_V \frac{3-4\eta^2}{2+\eta^3}\frac{2\psi+\eta^3}{3-4\psi\eta^2}, \quad \text{(A.4)}$$

where $\eta = v_s / v_p$, and $\psi = (\partial \ln v_s/\partial \ln T)_V /(\partial \ln v_p/\partial \ln T)_V$. There is also a direct relationship between v_ϕ and the isothermal bulk modulus (K_T), so we find

$$\left(\frac{\partial \ln v_\phi}{\partial \ln T}\right)_V = \frac{1}{2}\alpha T\left(K_T' + \frac{\gamma}{(1+\alpha\gamma T)} - \delta_T\right) \approx \frac{1}{2}\alpha T\left(K_T' + \gamma - \delta_T\right), \quad \text{(A.5)}$$

where α is the thermal expansion coefficient, K_T' is the pressure derivative of K_T, δ_T is the Anderson-Grüneisen parameter, and γ is the thermodynamic Grüneisen parameter.

Combining Equations (A.2), (A.4), and (A.5), we obtain an expression for the temperature derivative of the scaling parameter at constant volume:

$$\left(\frac{\partial \ln \xi}{\partial \ln T}\right)_V = -\frac{1}{2}\alpha T\left(K_T' + \gamma - \delta_T\right)\frac{3-4\eta^2}{2+\eta^3}\frac{2\psi+\eta^3}{3-4\psi\eta^2} \equiv -\frac{1}{2}\alpha T\epsilon, \quad \text{(A.6)}$$

where ϵ is introduced for abbreviation. Reasonable values of ψ over the compression range of this study are between 2 and 2.6 (*Stacey and Davis*, 2004), and previously reported values for v_p and v_s indicate $\eta \sim 0.5$ for ε-Fe (*Mao et al.*, 2001; *Lin et al.*, 2005).

Assuming $\alpha\epsilon$ varies with volume but not temperature, we are then able to integrate Equation (A.6) and obtain the following expression for the anharmonic melting temperature (T_M):

$$T_M = T_M^h \exp\left[\alpha\epsilon\left(T_M - T_0\right) - \alpha_{M0}\epsilon_{M0}\left(T_{M0} - T_0\right)\right]. \tag{A.7}$$

T_M^h is the uncorrected harmonic melting temperature (Equation (3.9)); $\alpha_{M0} = \alpha(V_{M0})$ and $\epsilon_{M0} = \epsilon(V_{M0})$, where V_{M0} is the volume of the anchor melting point; T_{M0} is the melting temperature of the anchor melting point; and T_0 = 300 K, the temperature at which our experiments were performed. Finally, since we find $|\alpha\epsilon(T_M - T_{M0})| \ll 1$, we can approximate the exponential linearly and solve for T_M:

$$T_M \approx T_M^h \frac{\left(1-\alpha\epsilon T_{M0}\right)\exp\left[\left(\alpha\epsilon - \alpha_{M0}\epsilon_{M0}\right)\left(T_{M0} - T_0\right)\right]}{1-\alpha\epsilon T_M^h \exp\left[\left(\alpha\epsilon - \alpha_{M0}\epsilon_{M0}\right)\left(T_{M0} - T_0\right)\right]}. \tag{A.8}$$

We use Equation (A.8) to determine our anharmonic melting temperatures, and the collection of terms to the right of T_M^h in Equation (A.8) are what we call the "anharmonic correction term." Taking η = 0.5, $\psi(V)$ from Stacey and Davis (2004), δ_T from Sharma and Sharma (2010), and K_T' and γ from *Dewaele et al.* (2006) (Table A.1), we find that $\epsilon(V)$ varies between 4.6 and 9.0 over the compression range of this study. Finally, applying these $\epsilon(V)$ values and $\alpha(V)$ from *Anderson et al.* (2001), we find an anharmonic correction term of 0.89 at our smallest compression point. For $P \geq 100$ GPa (after accounting for thermal pressure), this correction term is ~1.

Table A.1. Anharmonic correction term parameters.[a]

V (cm^3/mol)	α (10^{-5} K^{-1})	K_T'	δ_T	γ	Ψ
5.92(2)	3.88	4.47	4.91	1.68	1.97
5.81(1)	3.65	4.37	4.86	1.65	2.02
5.56(1)	3.06	4.17	4.73	1.61	2.15
5.36(1)	2.59	4.03	4.64	1.57	2.26
5.27(2)	2.45	3.97	4.59	1.56	2.31
5.15(2)	2.11	3.89	4.53	1.54	2.38
5.00(2)	1.81	3.80	4.46	1.52	2.45
4.89(2)	1.60	3.73	4.40	1.50	2.51
4.81(2)	1.43	3.68	4.36	1.49	2.54
4.70(2)	1.27	3.62	4.31	1.48	2.57

[a]The parameters presented here were used in Equation (A.8) to determine an anharmonic correction for our melting curve shape: α is the thermal expansion coefficient (*Anderson et al.*, 2001); K_T' is the pressure derivative of K_T (*Dewaele et al.*, 2006); δ_T is the Anderson-Grüneisen parameter (*Sharma and Sharma*, 2010); γ is the Grüneisen parameter (*Dewaele et al.*, 2006); and ψ is the ratio of the logarithmic temperature derivatives of v_s and v_p at constant volume (*Stacey and Davis*, 2004).

Bibliography

Ahrens, T. J., K. G. Holland, and G. Q. Chen (2002), Phase diagram of iron, revised-core temperatures, *Geophys. Res. Lett.*, *29*(7), 4, doi:10.1029/2001gl014350.

Akahama, Y., and H. Kawamura (2006), Pressure calibration of diamond anvil Raman gauge to 310 GPa, *J. Appl. Phys.*, *100*(4), 4, doi:10.1063/1.2335683.

Alfè, D., G. D. Price, and M. J. Gillan (2001), Thermodynamics of hexagonal-close-packed iron under Earth's core conditions, *Phys. Rev. B*, *64*(4), 16, doi:10.1103/PhysRevB.64.045123

Alfè, D., G. D. Price, and M. J. Gillan (2002), Iron under Earth's core conditions: Liquid-state thermodynamics and high-pressure melting curve from ab initio calculations, *Phys. Rev. B*, *65*(16), 11, doi:10.1103/PhysRevB.65.165118.

Anderson, O. L., and D. G. Isaak (2000), Calculated melting curves for phases of iron, *Am. Miner.*, *85*(2), 376-385.

Anderson, O. L., L. Dubrovinsky, S. K. Saxena, and T. LeBihan (2001), Experimental vibrational Grüneisen ratio values for epsilon-iron up to 330 GPa at 300 K, *Geophys. Res. Lett.*, *28*(12), 2359–2359.

Andrault, D., G. Fiquet, T. Charpin, and T. le Bihan (2000), Structure analysis and stability

field of beta-iron at high P and T, *Am. Miner.*, *85*(2), 364–371.

Angel, R. J. (2000), Equations of state, in *High-temperature and high-pressure crystal chemistry*, edited by R. M. Hazen and R. T. Downs.

Antonangeli, D., F. Occelli, H. Requardt, J. Badro, G. Fiquet, and M. Krisch (2004), Elastic anisotropy in textured hcp-iron to 112 GPa from sound wave propagation measurements, *Earth Planet. Sci. Lett.*, *225*(1–2), 243–251, doi:10.1016/j.epsl.2004.06.004.

Antonangeli, D., J. Siebert, J. Badro, D. L. Farber, G. Fiquet, G. Morard, and F. J. Ryerson (2010), Composition of the Earth's inner core from high-pressure sound velocity measurements in Fe-Ni-Si alloys, *Earth Planet. Sci. Lett.*, *295*(1–2), 292–296, doi:10.1016/j.epsl.2010.04.018.

Asanuma, H., E. Ohtani, T. Sakai, H. Terasaki, S. Kamada, T. Kondo, and T. Kikegawa (2010), Melting of iron-silicon alloy up to the core-mantle boundary pressure: implications to the thermal structure of the Earth's core, *Phys. Chem. Miner.*, *37*(6), 353–359, doi:10.1007/s00269-009-0338-7.

Asanuma, H., E. Ohtani, T. Sakai, H. Terasaki, S. Kamada, N. Hirao, and Y. Ohishi (2011), Static compression of Fe(0.83)Ni(0.09)Si(0.08) alloy to 374 GPa and Fe(0.93)Si(0.07) alloy to 252 GPa: Implications for the Earth's inner core, *Earth Planet. Sci. Lett.*, *310*(1–2), 113–118, doi:10.1016/j.epsl.2011.06.034.

Asimow, P. D., and T. J. Ahrens (2010), Shock compression of liquid silicates to 125 GPa: The anorthite-diopside join, *J. Geophys. Res.-Solid Earth*, *115*, doi:10.1029/2009jb007145.

Badding, J. V., R. J. Hemley, and H. K. Mao (1991), High-pressure chemistry of hydrogen in metals: in situ study of iron hydride, *Science*, *253*(5018), 421–424, doi:10.1126/science.253.5018.421.

Badro, J., G. Fiquet, F. Guyot, E. Gregoryanz, F. Occelli, D. Antonangeli, and M. d'Astuto (2007), Effect of light elements on the sound velocities in solid iron: Implications for the composition of Earth's core, *Earth Planet. Sci. Lett.*, *254*(1–2), 233–238, doi:10.1016/j.epsl.2006.11.025.

Bancroft, D., E. L. Peterson, and S. Minshall (1956), Polymorphism of iron at high pressure, *J. Appl. Phys.*, *27*(3), 291–298, doi:10.1063/1.1722359.

Belonoshko, A. B., R. Ahuja, and B. Johansson (2000), Quasi-ab initio molecular dynamic study of Fe melting, *Phys. Rev. Lett.*, *84*(16), 3638–3641, doi:10.1103/PhysRevLett.84.3638.

Bigeleisen, J., and M. G. Mayer (1947), Calculation of equilibrium constants for isotopic exchange reactions, *J. Chem. Phys.*, *15*(5), 261–267, doi:10.1063/1.1746492.

Birch, F. (1940), The alpha-gamma transformation of iron at high pressures, and the problem of the earth's magnetism, *Am. J. Sci.*, *238*(3), 192–211.

Birch, F. (1960), The velocity of compressional waves in rocks to 10 kilobars, part 1, *J. Geophys. Res.*, *65*(4), 1083–1102, doi:10.1029/JZ065i004p01083.

Birch, F. (1961), Velocity of compressional waves in rocks to 10 kilobars, part 2, *J. Geophys. Res.*, *66*(7), 2199–2224, doi:10.1029/JZ066i007p02199.

Birch, F. (1964), Density and composition of mantle and core, *J. Geophys. Res.*, *69*(20),

4377–4388.

Boehler, R., and J. Ramakrishnan (1980), Experimental results on the pressure dependence of the Grüneisen parameter: A review, *Journal of Geophysical Research*, *85*(NB12), 6996–7002.

Boehler, R., N. Vonbargen, and A. Chopelas (1990), Melting, thermal expansion, and phase transitions of iron at high pressures, *J. Geophys. Res.-Solid Earth Planets*, *95*(B13), 21731–21736.

Boehler, R. (1992), Melting of the Fe-FeO and the Fe-FeS systems at high pressure: Constraints on core temperatures, *Earth Planet. Sci. Lett.*, *111*(2–4), 217–227.

Boehler, R. (1993), Temperatures in the Earth's core from melting-point measurements of iron at high static pressures, *Nature*, *363*(6429), 534–536.

Boness, D. A., J. M. Brown, and A. K. McMahan (1986), The electronic thermodynamics of iron under Earth core conditions, *Phys. Earth Planet. Inter.*, *42*(4), 227–240.

Brown, J. M., and R. G. McQueen (1982), The equation of state for iron and the Earth's core, in *High-Pressure Research in Geophysics*, edited by S. Akimoto and M. H. Manghnani, pp. 611–623, Center for Academic Publications, Tokyo.

Brown, J. M., and R. G. McQueen (1986), Phase transitions, Grüneisen parameter, and elasticity for shocked iron between 77 GPa and 400 GPa, *J. Geophys. Res.-Solid Earth Planets*, *91*(B7), 7485–7494.

Buffett, B. A. (2000), Earth's core and the geodynamo, *Science*, *288*(5473), 2007–2012, doi:10.1126/science.288.5473.2007.

Campbell, A. J., C. T. Seagle, D. L. Heinz, G. Y. Shen, and V. B. Prakapenka (2007), Partial melting in the iron-sulfur system at high pressure: A synchrotron X-ray diffraction study, *Phys. Earth Planet. Inter.*, *162*(1–2), 119–128, doi:10.1016/j.pepi.2007.04.001.

Crowhurst, J. C., G. R. Hearne, J. D. Comins, A. G. Every, and P. R. Stoddart (1999), Surface Brillouin scattering at high pressure: Application to a thin supported gold film, *Phys. Rev. B*, *60*(22), 14990–14993.

Crowhurst, J. C., A. F. Goncharov, and J. M. Zaug (2004), Impulsive stimulated light scattering from opaque materials at high pressure, *J. Phys.-Condes. Matter*, *16*(14), S1137–S1142, doi:10.1088/0953-8984/16/14/023.

Dewaele, A., P. Loubeyre, F. Occelli, M. Mezouar, P. I. Dorogokupets, and M. Torrent (2006), Quasihydrostatic equation of state of iron above 2 Mbar, *Phys. Rev. Lett.*, *97*(21), 4, doi:10.1103/PhysRevLett.97.215504.

Dorogokupets, P. I., and A. R. Oganov (2003), Equations of state of Cu and Ag and revised ruby pressure scale, *Dokl. Earth Sci.*, *391A*(6), 854–857.

Dorogokupets, P. I., and A. R. Oganov (2006), Equations of state of Al, Au, Cu, Pt, Ta, and W and revised ruby pressure scale, *Dokl. Earth Sci.*, *410*(7), 1091–1095, doi:10.1134/s1028334x06070208.

Dubrovinsky, L. S., S. K. Saxena, and P. Lazor (1998), High-pressure and high-temperature in situ X-ray diffraction study of iron and corundum to 68 GPa using an internally heated diamond anvil cell, *Phys. Chem. Miner.*, *25*(6), 434–441.

Dubrovinsky, L. S., S. K. Saxena, N. A. Dubrovinskaia, S. Rekhi, and T. le Bihan (2000a), Grüneisen parameter of epsilon-iron up to 300 GPa from in-situ X-ray study, *Am. Miner.*, *85*(2), 386–389.

Dubrovinsky, L. S., S. K. Saxena, F. Tutti, S. Rekhi, and T. LeBehan (2000b), In situ X-ray study of thermal expansion and phase transition of iron at multimegabar pressure, *Phys. Rev. Lett.*, *84*(8), 1720–1723, doi:10.1103/PhysRevLett.84.1720.

Duffy, T. S., and D. L. Anderson (1989), Seismic Velocities in Mantle Minerals and the Mineralogy of the Upper Mantle, *Journal of Geophysical Research-Solid Earth and Planets*, *94*(B2), 1895–1912, doi:10.1029/JB094iB02p01895.

Duffy, T. S. (2008), Mineralogy at the extremes, *Nature*, *451*(7176), 269–270, doi:10.1038/nature06584.

Dziewonski, A. M., and D. L. Anderson (1981), Preliminary reference Earth model, *Phys. Earth Planet. Inter.*, *25*(4), 297–356.

Fei, Y. W., J. Li, C. M. Bertka, and C. T. Prewitt (2000), Structure type and bulk modulus of Fe(3)S, a new iron-sulfur compound, *Am. Miner.*, *85*(11–12), 1830–1833.

Fiquet, G., J. Badro, F. Guyot, H. Requardt, and M. Krisch (2001), Sound velocities in iron to 110 gigapascals, *Science*, *291*(5503), 468–471.

Fiquet, G., J. Badro, E. Gregoryanz, Y. Fei, and F. Occelli (2009), Sound velocity in iron carbide (Fe3C) at high pressure: Implications for the carbon content of the Earth's inner core, *Phys. Earth Planet. Inter.*, *172*(1-2), 125–129, doi:10.1016/j.pepi.2008.05.016.

Fischer, R. A., A. J. Campbell, O. T. Lord, G. A. Shofner, P. Dera, and V. B. Prakapenka (2011), Phase transition and metallization of FeO at high pressures and temperatures, *Geophys. Res. Lett.*, *38*, doi:10.1029/2011gl049800.

Gao, L. L., B. Chen, M. Lerche, E. E. Alp, W. Sturhahn, J. Y. Zhao, H. Yavas, and J. Li (2009), Sound velocities of compressed Fe3C from simultaneous synchrotron X-ray diffraction and nuclear resonant scattering measurements, *J. Synchr. Rad.*, *16*, 714–722, doi:10.1107/s0909049509033731.

Gerdau, E., R. Ruffer, H. Winkler, W. Tolksdorf, C. P. Klages, and J. P. Hannon (1985), Nuclear bragg diffraction of synchrotron radiation in yttrium iron garnet, *Phys. Rev. Lett.*, *54*(8), 835–838.

Giefers, H., R. Lübbers, K. Rupprecht, G. Wortmann, D. Alfè, and A. I. Chumakov (2002), Phonon spectroscopy of oriented hcp iron, *High Press. Res.*, *22*(2), 501–506, doi:10.1080/08957950290011437.

Gilvarry, J. J. (1956a), Variation of the amplitude of thermal vibration on the fusion curve, *Phys. Rev.*, *104*(4), 908–913.

Gilvarry, J. J. (1956b), The Lindemann and Grüneisen laws, *Phys. Rev.*, *102*(2), 308–316.

Hammersley, A. P., S. O. Svensson, M. Hanfland, A. N. Fitch, and D. Häusermann (1996), Two-dimensional detector software: From real detector to idealised image or two-theta scan, *High Pressure Res.*, *14*, 235–248.

Hemley, R. J., and H. K. Mao (2001), In situ studies of iron under pressure: New windows on the Earth's core, *Int. Geol. Rev.*, *43*(1), 1–30.

Hirao, N., T. Kondo, E. Ohtani, K. Takemura, and T. Kikegawa (2004a), Compression of iron hydride to 80 GPa and hydrogen in the Earth's inner core, *Geophys. Res. Lett.*, *31*(6), doi:10.1029/2003gl019380.

Hirao, N., E. Ohtani, T. Kondo, and T. Kikegawa (2004b), Equation of state of iron-silicon alloys to megabar pressure, *Phys. Chem. Miner.*, *31*(6), 329–336, doi:10.1007/s00269-004-0387-x.

Hu, M. Y., W. Sturhahn, T. S. Toellner, P. D. Mannheim, D. E. Brown, J. Y. Zhao, and E. E. Alp (2003), Measuring velocity of sound with nuclear resonant inelastic x-ray scattering, *Phys. Rev. B, 67*(9), 5, doi:10.1103/PhysRevB.67.094304.

Huang, H. J., Y. W. Fei, L. C. Cai, F. Q. Jing, X. J. Hu, H. S. Xie, L. M. Zhang, and Z. Z. Gong (2011), Evidence for an oxygen-depleted liquid outer core of the Earth, *Nature*, *479*(7374), 513−516, doi:10.1038/nature10621.

Isaak, D. G., and O. L. Anderson (2003), Thermal expansivity of HCP iron at very high pressure and temperature, *Physica B, 328*(3–4), 345–354, doi:10.1016/s0921-4526(02)01858-6.

Jackson, J. M., W. Sturhahn, M. Lerche, J. Zhao, T. S. Toellner, E. E. Alp, S. V. Sinogeikin, J. Bass, C. A. Murphy, and J. K. Wicks (2012), Melting of compressed iron by monitoring atomic dynamics, *under review*.

Jeanloz, R. (1979), Properties of Iron at High Pressures and the State of the Core, *J. Geophys. Res.*, *84*(NB11), 6059–6069.

Kantor, A. P., I. Y. Kantor, A. V. Kurnosov, A. Y. Kuznetsov, N. A. Dubrovinskaia, M.

Krisch, A. A. Bossak, V. P. Dmitriev, V. S. Urusov, and L. S. Dubrovinsky (2007), Sound wave velocities of fcc Fe-Ni alloy at high pressure and temperature by mean of inelastic X-ray scattering, *Phys. Earth Planet. Inter.*, *164*(1–2), 83–89, doi:10.1016/j.pepi.2007.06.006.

Kennett, B. L. N., E. R. Engdahl, and R. Buland (1995), Constraints on Seismic Velocities in the Earth from Traveltimes, *Geophys. J. Int.*, *122*(1), 108–124, doi:10.1111/j.1365-246X.1995.tb03540.x.

Komabayashi, T., and Y. Fei (2010), Internally consistent thermodynamic database for iron to the Earth's core conditions, *J. Geophys. Res.-Solid Earth*, *115*, 12, doi:10.1029/2009jb006442.

Kresch, M. G. (2009), Temperature dependence of phonons in elemental cubic metals studied by inelastic scattering of neutrons and x-rays, 286 pp, California Institute of Technology, Pasadena.

Laio, A., S. Bernard, G. L. Chiarotti, S. Scandolo, and E. Tosatti (2000), Physics of iron at Earth's core conditions, *Science*, *287*(5455), 1027–1030, doi:10.1126/science.287.5455.1027.

Lawson, A. C. (2009), Physics of the Lindemann melting rule, *Philosophical Magazine*, *89*(22-24), 1757-1770, doi:10.1080/14786430802577916.

Lin, J. F., A. J. Campbell, and D. L. Heinz (2003a), Static compression of iron-silicon alloys: Implications for silicon in the Earth's core, *J. Geophys. Res.*, *108*(B1), doi:10.1029/2002JB001978.

Lin, J. F., J. Shu, H. K. Mao, R. J. Hemley, and G. Shen (2003b), Amorphous boron gasket in diamond anvil cell research, *Rev. Sci. Instrum.*, *74*(11), 4732–4736, doi:10.1063/1.1621065.

Lin, J. F., V. V. Struzhkin, W. Sturhahn, E. Huang, J. Y. Zhao, M. Y. Hu, E. E. Alp, H. K. Mao, N. Boctor, and R. J. Hemley (2003c), Sound velocities of iron-nickel and iron-silicon alloys at high pressures, *Geophys. Res. Lett.*, *30*(21), 4, doi:10.1029/2003gl018405.

Lin, J. F., Y. Fei, W. Sturhahn, J. Y. Zhao, H. K. Mao, and R. J. Hemley (2004), Magnetic transition and sound velocities of Fe3S at high pressure: Implications for Earth and planetary cores, *Earth Planet. Sci. Lett.*, *226*(1–2), 33–40, doi:10.1016/j.epsl.2004.07.018.

Lin, J. F., W. Sturhahn, J. Y. Zhao, G. Shen, H. K. Mao, and R. J. Hemley (2005), Sound velocities of hot dense iron: Birch's law revisited, *Science*, *308*(5730), 1892–1894, doi:10.1126/science.1111724.

Lipkin, H. J. (1995), Mössbauer sum-rules for use with synchrotron sources, *Phys. Rev. B*, *52*(14), 10073–10079, doi:10.1103/PhysRevB.52.10073.

Lübbers, R., H. F. Grünsteudel, A. I. Chumakov, and G. Wortmann (2000), Density of phonon states in iron at high pressure, *Science*, *287*(5456), 1250–1253.

Luo, S. N., J. A. Akins, T. J. Ahrens, and P. D. Asimow (2004), Shock-compressed MgSiO(3) glass, enstatite, olivine, and quartz: Optical emission, temperatures, and melting, *J. Geophys. Res.-Solid Earth*, *109*(B5), doi:10.1029/2003jb002860.

Ma, Y. Z., H. K. Mao, R. J. Hemley, S. A. Gramsch, G. Shen, and M. Somayazulu (2001), Two-dimensional energy dispersive x-ray diffraction at high pressures and temperatures, *Rev. Sci. Instrum.*, *72*(2), 1302–1305.

Ma, Y. Z., M. Somayazulu, G. Shen, H. K. Mao, J. F. Shu, and R. J. Hemley (2004), In situ X-ray diffraction studies of iron to Earth-core conditions, *Phys. Earth Planet. Inter.*, *143*, 455–467, doi:10.1016/j.pepi.2003.06.005.

Mao, H. K., P. M. Bell, J. W. Shaner, and D. J. Steinberg (1978), Specific Volume Measurements of Cu, Mo, Pd, and Ag and Calibration of Ruby R1 Fluorescence Pressure Gauge From 0.06 to 1 Mbar, *J. Appl. Phys.*, *49*(6), 3276–3283, doi:10.1063/1.325277.

Mao, H. K., J. Xu, and P. M. Bell (1986), Calibration of the Ruby Pressure Gauge to 800 kbar under Quasi-Hydrostatic Conditions, *Journal of Geophysical Research-Solid Earth and Planets*, *91*(B5), 4673–4676, doi:10.1029/JB091iB05p04673.

Mao, H. K., Y. Wu, L. C. Chen, J. F. Shu, and A. P. Jephcoat (1990), Static Compression of Iron to 300 GPa and $Fe_{0.8}Ni_{0.2}$ Alloy to 260 GPa: Implications for Composition of the Core, *J. Geophys. Res.-Solid Earth Planets*, *95*(B13), 21737–21742.

Mao, H. K., J. F. Shu, G. Shen, R. J. Hemley, B. S. Li, and A. K. Singh (1999), Elasticity and rheology of iron above 220 GPa and the nature of the Earth's inner core (vol 396, pg 741, 1998), *Nature*, *399*(6733), 280–280.

Mao, H. K., et al. (2001), Phonon density of states of iron up to 153 gigapascals, *Science*, *292*(5518), 914–916.

Mao, W. L., W. Sturhahn, D. L. Heinz, H. K. Mao, J. F. Shu, and R. J. Hemley (2004), Nuclear resonant x-ray scattering of iron hydride at high pressure, *Geophys. Res. Lett.*, *31*(15), doi:10.1029/2004gl020541.

Mao, W. L., et al. (2008), Experimental determination of the elasticity of iron at high pressure, *J. Geophys. Res.-Solid Earth*, *113*(B9), 14, doi:10.1029/2007jb005229.

McDonough, W. F. (2003), Compositional Model for the Earth's Core, in *Treatise on Geochemistry, The Mantle and Core*, edited by D. H. Heinrich and K. T. Karl, pp. 547–568, Pergamon, Oxford.

McQueen, R. G., S. P. Marsh, J. W. Taylor, J. N. Fritz, and W. J. Carter (1970), The equation of state of solids from shock wave studies, in *High-Velocity Impact Phenomena*, edited by R. Kinslow, pp. 293–417, Academic, New York.

Merkel, S., A. F. Goncharov, H. K. Mao, P. Gillet, and R. J. Hemley (2000), Raman spectroscopy of iron to 152 gigapascals: Implications for Earth's inner core, *Science*, *288*(5471), 1626–1629, doi:10.1126/science.288.5471.1626.

Morard, G., D. Andrault, N. Guignot, C. Sanloup, M. Mezouar, S. Petitgirard, and G. Fiquet (2008), In situ determination of Fe-Fe3S phase diagram and liquid structural properties up to 65 GPa, *Earth Planet. Sci. Lett.*, *272*(3–4), 620–626, doi:10.1016/j.epsl.2008.05.028.

Murphy, C. A., J. M. Jackson, W. Sturhahn, and B. Chen (2011a), Melting and thermal pressure of hcp-Fe from the phonon density of states, *Phys. Earth Planet. Inter.*, *188*(1–2), 114–120, doi:10.1016/j.pepi.2011.07.001.

Murphy, C. A., J. M. Jackson, W. Sturhahn, and B. Chen (2011b), Grüneisen parameter of hcp-Fe to 171 GPa, *Geophysical Research Letters*, *38*(L24306), doi:10.1029/2011GL049531.

Musgrave, M. J. P. (1970), *Crystal Acoustics: Introduction to the study of elastic waves and vibrations in crystals*, pp. 72, Holden-Day, Inc., San Francisco.

Narygina, O., L. S. Dubrovinsky, C. A. McCammon, A. Kurnosov, I. Y. Kantor, V. B. Prakapenka, and N. A. Dubrovinskaia (2011), X-ray diffraction and Mössbauer spectroscopy study of fcc iron hydride FeH at high pressures and implications for the composition of the Earth's core, *Earth Planet. Sci. Lett.*, *307*(3–4), 409–414, doi:10.1016/j.epsl.2011.05.015.

Nguyen, J. H., and N. C. Holmes (2004), Melting of iron at the physical conditions of the Earth's core, *Nature*, *427*(6972), 339–342, doi:10.1038/nature02248.

Ohta, K., R. E. Cohen, K. Hirose, K. Haule, K. Shimizu, and Y. Ohishi (2012), Experimental and Theoretical Evidence for Pressure-Induced Metallization in FeO with Rocksalt-Type Structure, *Phys. Rev. Lett.*, *108*(2), doi:10.1103/PhysRevLett.108.026403.

Poirier, J.-P. (2000), *Introduction to the Physics of the Earth's Interior*, Second ed., pp. 232-233, Cambridge University Press, Cambridge, UK.

Polyakov, V. B. (1998), On anharmonic and pressure corrections to the equilibrium isotopic constants for minerals, *Geochim. Cosmochim. Acta*, *62*(18), 3077–3085, doi:10.1016/s0016-7037(98)00220-8.

Polyakov, V. B., and S. D. Mineev (1999), Mössbauer spectroscopy as applied to isotopic geochemistry: I. Equilibrium fractionation of iron isotopes, *Geokhimiya*(8), 858–870.

Polyakov, V. B. (2009), Equilibrium iron isotope fractionation at core-mantle boundary conditions, *Science*, *323*(5916), 912–914, doi:10.1126/science.1166329.

Ruffer, R., E. Gerdau, M. Grote, R. Hollatz, R. Rohlsberger, H. D. Ruter, and W. Sturhahn (1990), Nuclear Bragg-diffraction using synchrotron radiation: A new method for hyperfine spectroscopy, *Hyperfine Interact.*, *61*(1–4), 1279–1293, doi:10.1007/bf02407612.

Sakai, T., E. Ohtani, H. Terasaki, S. Kamada, N. Hirao, M. Miyahara, and M. Nishijima (2011), Phase stability and compression study of (Fe(0.89),Ni(0.11))(3)S up to pressure of the Earth's core, *Am. Miner.*, *96*(10), 1490–1494, doi:10.2138/am.2011.3822.

Saxena, S. K., and L. S. Dubrovinsky (2000), Iron phases at high pressures and temperatures: Phase transition and melting, *Am. Miner.*, *85*(2), 372–375.

Schauble, E. A. (2004), Applying stable isotope fractionation theory to new systems, in *Geochemistry of Non-Traditional Stable Isotopes*, edited by C. M. Johnson, B. L. Beard and F. Albarede, pp. 65–111, Mineralogical Soc Amer, Chantilly.

Scott, H. P., Q. Williams, and E. Knittle (2001), Stability and equation of state of Fe3C to 73 GPa: Implications for carbon in the Earth's core, *Geophys. Res. Lett.*, *28*(9), 1875–1878, doi:10.1029/2000gl012606.

Seagle, C. T., D. L. Heinz, A. J. Campbell, V. B. Prakapenka, and S. T. Wanless (2008), Melting and thermal expansion in the Fe-FeO system at high pressure, *Earth Planet. Sci. Lett.*, *265*(3–4), 655–665, doi:10.1016/j.epsl.2007.11.004.

Seto, M., Y. Yoda, S. Kikuta, X. W. Zhang, and M. Ando (1995), Observation of Nuclear Resonant Scattering Accompanied by Phonon Excitation Using Synchrotron Radiation, *Phys. Rev. Lett.*, *74*(19), 3828-3831.

Sha, X. W., and R. E. Cohen (2006), Lattice dynamics and thermodynamics of bcc iron under pressure: First-principles linear response study, *Phys. Rev. B*, *73*(10), doi:10.1103/PhysRevB.73.104303.

Sha, X. W., and R. E. Cohen (2010a), First-principles thermal equation of state and thermoelasticity of hcp Fe at high pressures, *Phys. Rev. B*, *81*(9), 10, doi:10.1103/PhysRevB.81.094105.

Sha, X. W., and R. E. Cohen (2010b), Elastic isotropy of epsilon-Fe under Earth's core conditions, *Geophys. Res. Lett.*, *37*, doi:10.1029/2009gl042224.

Sharma, S. K., and B. K. Sharma (2010), Volume dependence of thermal expansivity for hcp iron, *Phys. B-Condes. Matter*, *405*(15), 3145–3148, doi:10.1016/j.physb.2010.04.037.

Shen, G., H. K. Mao, R. J. Hemley, T. S. Duffy, and M. L. Rivers (1998), Melting and crystal structure of iron at high pressures and temperatures, *Geophys. Res. Lett.*, *25*(3), 373–376.

Shen, G., W. Sturhahn, E. E. Alp, J. Zhao, T. S. Toellner, V. B. Prakapenka, Y. Meng, and

H. R. Mao (2004), Phonon density of states in iron at high pressures and high temperatures, *Phys. Chem. Miner.*, *31*(6), 353–359, doi:10.1007/s00269-004-0403-1.

Shibazaki, Y., et al. (2012), Sound velocity measurements in dhcp-FeH up to 70 GPa with inelastic X-ray scattering: Implications for the composition of the Earth's core, *Earth Planet. Sci. Lett.*, *313*, 79–85, doi:10.1016/j.epsl.2011.11.002.

Simon, F., and G. Glatzel (1929), Remarks on fusion pressure curve, *Z. Anorg. Allg. Chem.*, *178*(1/3), 309–316.

Sola, E., and D. Alfè (2009), Melting of Iron under Earth's Core Conditions from Diffusion Monte Carlo Free Energy Calculations, *Phys. Rev. Lett.*, *103*(7), 4, doi:10.1103/PhysRevLett.103.078501.

Sola, E., J. P. Brodholt, and D. Alfè (2009), Equation of state of hexagonal closed packed iron under Earth's core conditions from quantum Monte Carlo calculations, *Phys. Rev. B*, *79*(2), 6, doi:10.1103/PhysRevB.79.024107.

Stacey, F. D., and P. M. Davis (2004), High pressure equations of state with applications to the lower mantle and core, *Phys. Earth Planet. Inter.*, *142*(3–4), 137–184, doi:10.1016/j.pepi.2004.02.003.

Steinle-Neumann, G., L. Stixrude, R. E. Cohen, and O. Gulseren (2001), Elasticity of iron at the temperature of the Earth's inner core, *Nature*, *413*(6851), 57–60, doi:10.1038/35092536.

Steinle-Neumann, G., L. Stixrude, and R. E. Cohen (2004), First-principles elastic

constants for the hcp transition metals Fe, Co, and Re at high pressure (vol 60, pg 791, 1999), *Phys. Rev. B, 69*(21), doi:10.1103/PhysRevB.69.219903.

Stevenson, D. J. (1981), Models of the Earth's Core, *Science*, *214*(4521), 611–619.

Stixrude, L., R. E. Cohen, and D. J. Singh (1994), Iron at High-Pressure: Linearized-Augmented-Plane-Wave Computations in the Generalized-Gradient Approximation, *Phys. Rev. B*, *50*(9), 6442-6445, doi:10.1103/PhysRevB.50.6442.

Stixrude, L., E. Wasserman, and R. E. Cohen (1997), Composition and temperature of Earth's inner core, *J. Geophys. Res.-Solid Earth*, *102*(B11), 24729–24739.

Strong, H. M., R. E. Tuft, and R. E. Hanneman (1973), Iron fusion curve and gamma-delta-L triple point, *Metallurgical Transactions*, *4*(11), 2657–2661, doi:10.1007/bf02644272.

Struzhkin, V. V., et al. (2001), Nuclear inelastic X-ray scattering of FeO to 48 GPa, *Phys. Rev. Lett.*, *87*(25), doi:10.1103/PhysRevLett.87.255501.

Sturhahn, W., T. S. Toellner, E. E. Alp, X. Zhang, M. Ando, Y. Yoda, S. Kikuta, M. Seto, C. W. Kimball, and B. Dabrowski (1995), Phonon density of states measured by inelastic nuclear resonant scattering, *Phys. Rev. Lett.*, *74*(19), 3832–3835.

Sturhahn, W., and A. Chumakov (1999), Lamb-Mössbauer factor and second-order Doppler shift from inelastic nuclear resonant absorption, *Hyperfine Interact.*, *123*(1–8), 809–824, doi:10.1023/a:1017060931911.

Sturhahn, W. (2000), CONUSS and PHOENIX: Evaluation of nuclear resonant scattering data, *Hyperfine Interact.*, *125*(1–4), 149–172.

Sturhahn, W. (2004), Nuclear resonant spectroscopy, *J. Phys.-Condes. Matter*, *16*(5), S497–S530.

Sturhahn, W., and J. M. Jackson (2007), Geophysical Applications of Nuclear Resonant Spectroscopy, *Geol. Soc. Am., Special Paper 421*, 157–174.

Tateno, S., K. Hirose, Y. Ohishi, and Y. Tatsumi (2010), The structure of iron in Earth's inner core, *Science*, *330*(6002), 359–361, doi:10.1126/science.1194662.

Terasaki, H., S. Kamada, T. Sakai, E. Ohtani, N. Hirao, and Y. Ohishi (2011), Liquidus and solidus temperatures of a Fe-O-S alloy up to the pressures of the outer core: Implication for the thermal structure of the Earth's core, *Earth Planet. Sci. Lett.*, *304*(3–4), 559–564, doi:10.1016/j.epsl.2011.02.041.

Toellner, T. S. (2000), Monochromatization of synchrotron radiation for nuclear resonant scattering experiments, *Hyperfine Interact.*, *125*(1–4), 3–28, doi:10.1023/a:1012621317798.

Uchida, T., Y. B. Wang, M. L. Rivers, and S. R. Sutton (2001), Stability field and thermal equation of state of epsilon-iron determined by synchrotron X-ray diffraction in a multianvil apparatus, *J. Geophys. Res.-Solid Earth*, *106*(B10), 21799–21810.

Vočadlo, L., G. A. de Wijs, G. Kresse, M. Gillan, and G. D. Price (1997), First principles calculations on crystalline and liquid iron at Earth's core conditions, *Faraday Discuss.*, *106*, 205–217.

Vočadlo, L., J. Brodholt, D. Alfè, M. J. Gillan, and G. D. Price (2000), Ab initio free energy calculations on the polymorphs of iron at core conditions, *Phys. Earth*

Planet. Inter., *117*(1–4), 123–137.

Vočadlo, L., D. P. Dobson, and I. G. Wood (2009), Ab initio calculations of the elasticity of hcp-Fe as a function of temperature at inner-core pressure, *Earth Planet. Sci. Lett.*, *288*(3–4), 534–538, doi:10.1016/j.epsl.2009.10.015.

Wallace, D. C. (1991), Melting of elements, *Proceedings of the Royal Society of London Series a-Mathematical Physical and Engineering Sciences*, *433*(1889), 631–661, doi:10.1098/rspa.1991.0068.

Wasserman, E., L. Stixrude, and R. E. Cohen (1996), Thermal properties of iron at high pressures and temperatures, *Phys. Rev. B*, *53*(13), 8296–8309.

Williams, Q., R. Jeanloz, J. Bass, B. Svendsen, and T. J. Ahrens (1987), The melting curve of iron to 250 gigapascals: A constraint on the temperature at Earth's center, *Science*, *236*(4798), 181–182.

Williams, Q., and R. Jeanloz (1990), Melting relations in the iron-sulfur system at ultra high pressures: Implications for the thermal state of the Earth, *J. Geophys. Res.-Solid Earth Planets*, *95*(B12), 19299–19310.

Wojdyr, M. (2010), Fityk: A general-purpose peak fitting program, *J. Appl. Crystallogr.*, *43*, 1126–1128, doi:10.1107/S0021889810030499.

Yoo, C. S., N. C. Holmes, M. Ross, D. J. Webb, and C. Pike (1993), Shock temperatures and melting of iron at Earth core conditions, *Phys. Rev. Lett.*, *70*(25), 3931–3934, doi:10.1103/PhysRevLett.70.3931.